# Analysis and Strategies for Five-Axis Near-Dry EDM Milling

by

Masahiro Fujiki

A dissertation submitted in partial fulfillment
of the requirements for the degree of
Doctor of Philosophy
(Mechanical Engineering)
in The University of Michigan
2009

Doctoral Committee:

Professor Jun Ni, Co-Chair
Professor Albert J. Shih, Co-Chair
Professor Jessy W. Grizzle
Professor Elijah Kannatey-Asibu Jr.
Research Scientist David A. Stephenson

# Acknowledgements

I wish to express my sincere appreciation to Dr. Jun Ni, Professor at the University of Michigan and Director of the S.M. Wu Manufacturing Research Center (WuMRC) for serving as co-chair for this project. I would also thank Dr. Albert J. Shih, Professor at the University of Michigan for also serving as my co-chair. Professor Ni and Professor Shih have been great mentors. Their insight and teaching inspired me to continue my education in the area of manufacturing.

Second, I would like to thank Dr. Jyoti Mazumder, Dr. Bhaskar Dutta, and Mr. Vijay Singh of the Precision Optic Manufacturing Group Inc., and Dr. Jean-Luis Staudenmann of National Institute of Standard and Technology, for their generous support on this project. Without their support, this project would never have been possible.

Also, I would like to thank Dr. Elijah Kannatey-Asibu Jr., Dr. Jessy W. Grizzle, Professors at the University of Michigan, and Dr. David A. Stephenson, research scientist at WuMRC, for being on my committee and providing me with helpful advice. Dr. Gap-Yong Kim, formerly a research fellow at WuMRC and currently an Assistant Professor at Iowa State University, and Mr. Xianli Qiao, a research scientist at WuMRC, also provided very valuable advice and time on this project. Finally, I wish to thank Adam Brzezinski, Matthew Chastagner, Robert Dodde, Shiming Duan, Daniel Johnson, Cindy

Kuo, Seungchul Lee, Carl McGill, Jason Moore, Bruce Tai, and all the members of the S.M. Wu Manufacturing Research Center, for their help, support and suggestions over the past four years.

# Table of Contents

# List of Figures

# List of Tables

# Abstract

Strategies for precision five-axis near-dry electric discharge machining (EDM) milling are investigated. By understanding the material removal process behind near-dry EDM milling, its performance can further be improved using a machine with five degrees of freedom. Three major research areas are investigated: (1) effect of electrode orientation in five-axis milling, (2) the trajectory planning for five-axis near-dry EDM milling, and (3) a new gap control strategy for five-axis near-dry EDM process.

Computational fluid dynamics (CFD) model is developed to predict the dielectric fluid flow rate for various electrode inclinations and qualitatively compared with the experimentally measured material removal rate. The study shows that the material removal rate is linearly proportional to the mass flow rate of air and kerosene mixture, the tool electrode wear ratio is inversely related to the mass flow rate of the air and kerosene mixture, and the average surface roughness is not correlated with the flow rate of the mixture.

Using the results from the electrode orientation investigation, a tool path planning strategy that maximizes the material removal rate in roughing process is developed. The strategy includes methods to engage into the workpiece, machining of workpiece edge, minimum lead angle for curved surface, and minimum and maximum path interval.

Experimental verifications of the proposed path planning strategy yielded higher material removal rate compared with that of standard path planning.

A new gap control strategy for five-axis near-dry EDM is proposed and experimentally investigated. The new gap controller retracts the electrode in the direction of electrode orientation. The performance of the new gap controller in term of material removal rate, tool electrode wear ratio and surface roughness is compared with that of a conventional controller. The experimental verification yielded 30% increase in material removal rate while not affecting the tool electrode wear ratio and surface roughness.

# Chapter 1.

# Introduction

## 1.1 Research Background

Electric discharge machining (EDM) is an eletro-thermal process. When a large electric potential difference is developed between two electrically conductive materials in the distance of 10 to 100 μm in dielectric medium, the dielectric medium breaks down and a channel of plasma is formed in the "gap" between the electrode and workpiece (Kunieda et al., 2005). Electrons and ions travel in the plasma channel, and the bombardment of electrons and ions against the material generates heat. The heat instantaneously melts and vaporizes the material, and quickly dissipates once the discharge ends. The amount of material removed per each discharge is minute compared with conventional machining processes such as milling and drilling. However, by controlling the electric potential difference between the workpiece and electrode at high frequency, reasonable amount of material removal process is possible. Since EDM can remove any electrically conductive workpiece material regardless of the material hardness, it is widely used for difficult-to-machine materials with conventional machining process.

As shown in Figure 1.1, there are mainly two types of EDM processes widely used in the industry (Kunieda et al., 2005). The first type is the wire EDM, in which high electric potential difference is applied between the traveling wire and the workpiece to cut a material like a band saw. The second type is called die-sinking EDM. It is commonly used in manufacturing of dies and mold with difficult-to-machine material (Ho and Newman, 2003). An electrode that mates with the final product is used to create cavities on the final product. Typically, several electrodes are consumed for roughing and finishing in die-sinking EDM. As the material is removed from the workpiece, the thermal energy from the electric discharges also removes the material from the electrode and changes the electrode geometry (Crookall, 1979).

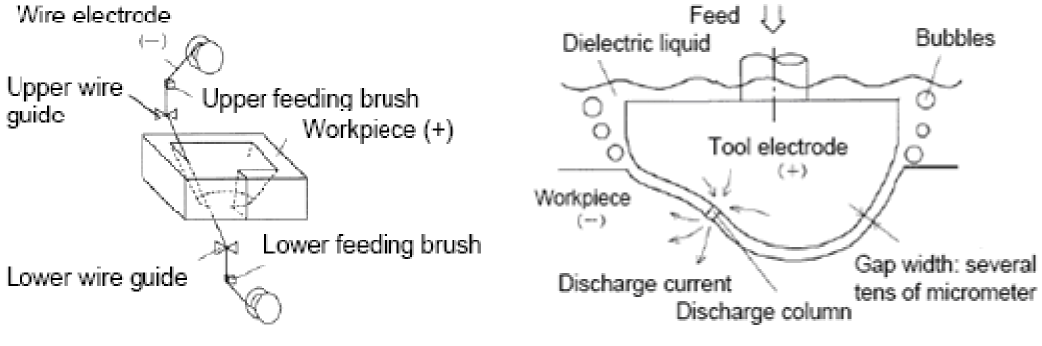

(a) (b)

Figure 1.1. Two types of EDM system (Kunieda et al., 2005) (a) wire cut and (b) die-sinker.

While the use of die-sinking EDM is still popular in the industry today, studies to replace the electrodes that have complex geometric features with simpler electrodes, as shown in Figure 1.2, have been active since the late 1980's (Saito et al., 1986, Kaneko and Tsuchiya, 1988). Nowadays, majority of research on EDM with simple electrodes use rotating solid or tubular electrodes, and CNC contouring control is utilized so that EDM machine is used like a machining center (Bayramoglu and Duffill, 1994). This method is known as EDM milling or milling by EDM. Although EDM milling can eliminate the need to machine electrodes for die-sinking EDM, there are still many challenges that need to be overcome for practical application.

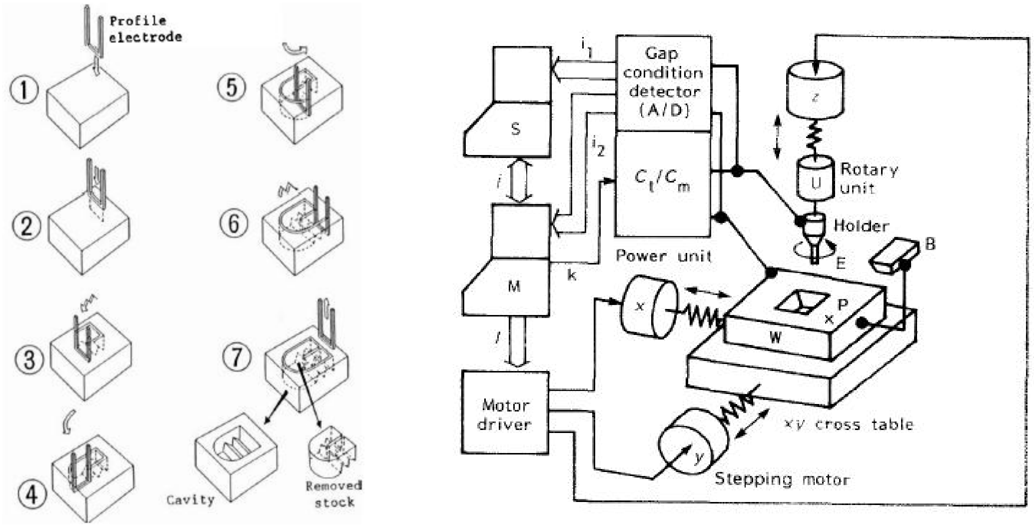

(a) (b)

Figure 1.2. EDM contouring with simple electrodes, (a) 3D swept mold cavity (Saito et al., 1986) and (b) rotating rod (Kaneko and Tsuchiya, 1988).

Much of research in EDM milling is concentrated in two areas. First area is estimation and compensation of tool wear and the second area of study in EDM milling is replacement of die-electric medium.

To describe the amount of tool wear, a non-dimensional variable called the tool electrode wear ratio, is often used (Kunieda et al., 2005). This parameter is also called electrode wear ratio (Lin and Lin, 2002) or volumetric electrode wear (Luis et al., 2005). It is defined as the ratio of the volume of electrode wear ($\Delta V_{electrode}$) to the volume of workpiece removed ($\Delta V_{workpiece}$) as in Eq. (1-1).

$$\eta = \frac{\Delta V_{electrode}}{\Delta V_{workpiece}} \tag{1-1}$$

The research in tool wear in EDM milling may be categorized into two areas: experimental study on electrode wear, and electrode wear compensation.

Dauw and Snooeys (1986) developed a real-time wear sensing system based on spark recognition to estimate the tool wear within one percent error. Yu et al. (1998) developed uniform wear method, which uses series of different trajectories to machine one surface as illustrated in Figure 1.3.

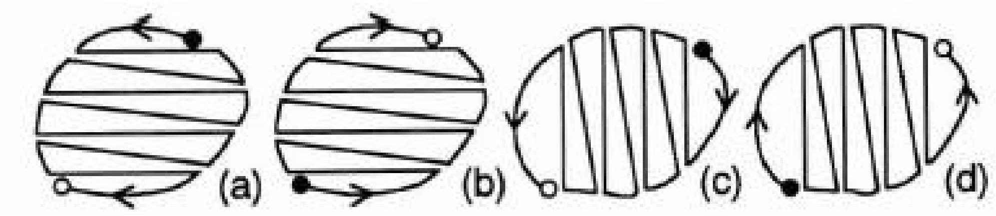

Figure 1.3. X-Y plane trajectory for uniform wear method (Yu et al., 1998).

Chang and Chiu (2004) proposed a method to compensate for tubular electrode wear by controlling the gap distance in Z-axis direction as shown in Figure 1.4. The electrode shortening can be compensated without knowing the exact tool electrode wear ratio. However, this method only works in small depth of cut with a flat surface before machining. It is not suitable for contouring along complex geometries in five-axis EDM milling.

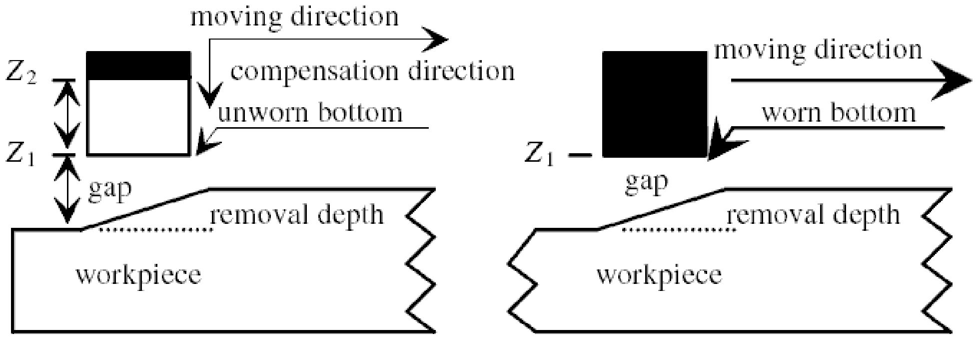

Figure 1.4. Tool shortening compensation for electric discharge scanning (Chang and Chiu, 2004).

Bleys et al. (2004) predicted tool shortening based on the electrode trajectory and spark counting. In EDM milling, if all the discharge parameters and machining conditions are fixed, the volume of electrode wear is proportional to the total volume of work-material removal. Moreover, if the generator, which outputs the high frequency electric potential to initiate the electric discharge, is an iso-energetic pulse generator, the volume of electrode wear can be estimated by multiplying a constant to the total number of normal discharges.

Pham et al. (2004) proposed a method that combines the uniform wear method by Yu et al. (1998) and the manual measurements of electrode shortening. This method is very accurate and does not require any information regarding the tool electrode wear ratio since the tool wear is measured and compensated after each path. However, longer machining time is required since the electrode contours along the location that has passed before.

Conventional EDM processes use liquid dielectric fluid. Research in dry EDM using gas as the dielectric medium has been studied under the EDM milling configuration using the tubular copper electrode (Kunieda et al., 1997, 2001, and 2003, Wang and Kunieda, 2004, Yoshida and Kunieda, 1999, Yu et al., 2004 and 2005). Due to the reattachment of debris to the machined surface, dry EDM milling may have limitations of meeting the combined material removal rate and surface roughness requirements. The accuracy of surface profile deteriorates with the debris deposition. This problem can be overcome in near-dry EDM by replacing the gas with the mixture of gas and dielectric liquid (Tao et al., 2008). Compared to the conventional EDM process, near-dry EDM milling has another advantage. It does not require a bath of dielectric fluid. Only a small amount of liquid dielectric fluid is used.

## 1.2 Research Motivations

There are two motivations in this research. The first motivation is the reduction of the production time of dies and molds by using near-dry EDM milling. The second motivation is the achievement of precision accuracy by using a five-axis near-dry EDM milling.

Near-dry EDM milling significantly shortens the machining time. The conventional way to produce dies and molds using an EDM die-sinker requires multiple electrodes. Machining of multiple electrodes increases the total production time. To survive in the competitive market, the delivery time of the final product is critical. Near-dry EDM milling eliminates the need to produce multiple electrodes.

Near-dry EDM milling in five-axis improves the precision accuracy by providing more flexibility in machining of dies and molds. By adding two extra degrees of freedom, the electrode can be oriented freely with respect to the workpiece surface and precision machining with shorter machining time can be achieved.

## 1.3 Research Objectives and Frameworks

The objectives of this research are to understand the fundamental aspects of EDM milling in near-dry condition and apply the knowledge to five-axis near-dry EDM milling. The fundamental understanding of machining process can improve the performance limits of the current state-of-the-art near-dry EDM milling. Three major topics have been identified for the research as the following:

1. Electrode orientation
2. Trajectory planning
3. Gap control strategy

### 1.3.1 Investigation of Effect of Electrode Orientation

A five-axis machine enables to freely orient the electrode. In three-axis EDM milling, the electrode can only travel in X, Y, and Z-axis directions, and the electrode is always perpendicular to the X-Y plane. This causes inefficient flow of high pressure mist in the discharge gap, especially in semi-finishing and finishing. However, the effects of the orientation angle must be understood for optimal control of the machining process.

Preliminary experiments show that the tool inclination with respect to the workpiece influences the material removal rate, tool electrode wear ratio, and surface finish. To fully utilize the capability of the five-axis machine, a fundamental understanding of the effects of tool orientation on the EDM process will be investigated in Chapter 2.

### 1.3.2 Five-Axis Tool Path Planning for Five-Axis Near-Dry EDM Milling

EDM milling of a sculptured surface requires intensive trajectory planning. Since EDM milling is a slow process, inefficient trajectory may lead to a long machining time. EDM milling is a relatively new machining method, and only primitive study has been conducted for three-axis EDM milling.

In order to develop a strategy for five-axis near-dry EDM milling, the differences between conventional machining process and EDM milling were analyzed. It was found that the concept of five-axis trajectory planning for conventional machining process can't be applied to near-dry EDM. In Chapter 3, a trajectory planning strategy for near-dry EDM milling that utilizes the concepts of maximization of mist flow rate through discharge region is developed.

### 1.3.3 Gap Control of Five-Axis Near-Dry EDM Milling

In EDM, the gap distance between the electrode and the workpiece must be controlled at high speed and with high accuracy. After each electric discharge, a small amount of material is removed and floats in the gap, which changes the dielectric properties in the gap. Therefore, an accurate control of gap distance is required to quickly flush the debris away.

There has been no reported work on the control of five-axis near-dry EDM milling. Since the discharge location for five-axis near-dry EDM milling is different from three-axis near-dry EDM milling, a new gap controlling strategy must be developed. In Chapter 4, a new gap controlling strategy for five-axis near-dry EDM milling that retracts the electrode in the direction of electrode orientation rather than along the trajectory is discussed.

# Chapter 2.

# Investigation of Effect of Electrode Orientation

## 2.1 Introduction

The advantage of five-axis near-dry EDM milling is the extra degrees of freedom in electrode orientation. The orientation of rotating electrode relative to the surface and the inlet pressure of the mist through the electrode are two important process parameters that affect the machining characteristics in near-dry EDM milling. Effects of electrode orientation in dry EDM milling and the discovery of the optimum electrode orientation to maximize the material removal rate (*MRR*) have been studied experimentally (Nakao et al., 2005). The increase in inlet pressure monotonically raises *MRR* in near-dry EDM milling was found (Tao et al., 2008). This research conducts experimental study as well as numerical analysis to investigate the effects of electrode orientation and dielectric mist pressure on the *MRR*, tool wear, and surface roughness in near-dry EDM milling.

Although many experimental studies have been conducted in EDM milling, the research on modeling the dielectric fluid flow in the narrow gap between the tubular electrode and machined surface and correlating the model predicted flow rate to experimentally measured *MRR* is lacking. This chapter develops a CFD model to study the flow field of dielectric fluid for various electrode orientation and inlet pressure and predict the flow rate.

Experimental setup to investigate the effects of lead and tilt angles and inlet pressure on machining performance, including *MRR*, tool electrode wear ratio and surface roughness, is first presented. The analysis and discussion of experimental results are followed. Details of CFD models and mesh generation are presented. Finally, CFD analysis results are discussed, analyzed, and compared to machining performance measured from experiments.

## 2.2 Experimental Setup

A die-sinking EDM machine (Model EDMS 150H by EDM Solutions, Elk Grove Village, IL) is modified by adding an EDM spindle (Rotobore by Everest Inc., Huntington Beach, CA) and a mist delivery system (Model 6000 precision applicator by AMCOL, Hazel Park, MI). Pressure regulated air enters the mist delivery system; and two tubes, one containing air and another containing liquid, exit from the system. The two tubes are connected to the atomizer attached on the EDM spindle. The mist of air and liquid mixture exits from the tubular electrode.

Inclined workpiece holders with angles ranging from 5° to 30° at 5° increments are fabricated to orient the workpiece with precise lead angle ($\alpha$) and tilt angle ($\beta$) relative to the electrode in the three-axis EDM machine. Figure 2.1(a) illustrates the definition of $\alpha$ and $\beta$. Three vectors are introduced to define $\alpha$ and $\beta$: the electrode axis vector, $\boldsymbol{A}$, surface normal, $\boldsymbol{N}$, and electrode feed direction, $\boldsymbol{F}$. The cross feed direction vector, $\boldsymbol{F}_{\perp}$, is the component of $\boldsymbol{F}$ perpendicular to the plane created by $\boldsymbol{N}$ and $\boldsymbol{F}$. The vector $\boldsymbol{A}$ projected on a plane created by $\boldsymbol{N}$ and $\boldsymbol{F}$ is denoted as $\boldsymbol{A}_{\alpha}$. The vector $\boldsymbol{A}$ projected on a plane created by $\boldsymbol{N}$ and $\boldsymbol{F}_{\perp}$ is denoted as $\boldsymbol{A}_{\beta}$. The lead angle $\alpha$ is defined as the angle between $\boldsymbol{N}$ and $\boldsymbol{A}_{\alpha}$. The tilt angle $\beta$ is defined as the angle between $\boldsymbol{N}$ and $\boldsymbol{A}_{\beta}$ (Kruth and Klewais, 1994). When the lead and tilt angles are both zero, the electrode is normal to the workpiece surface.

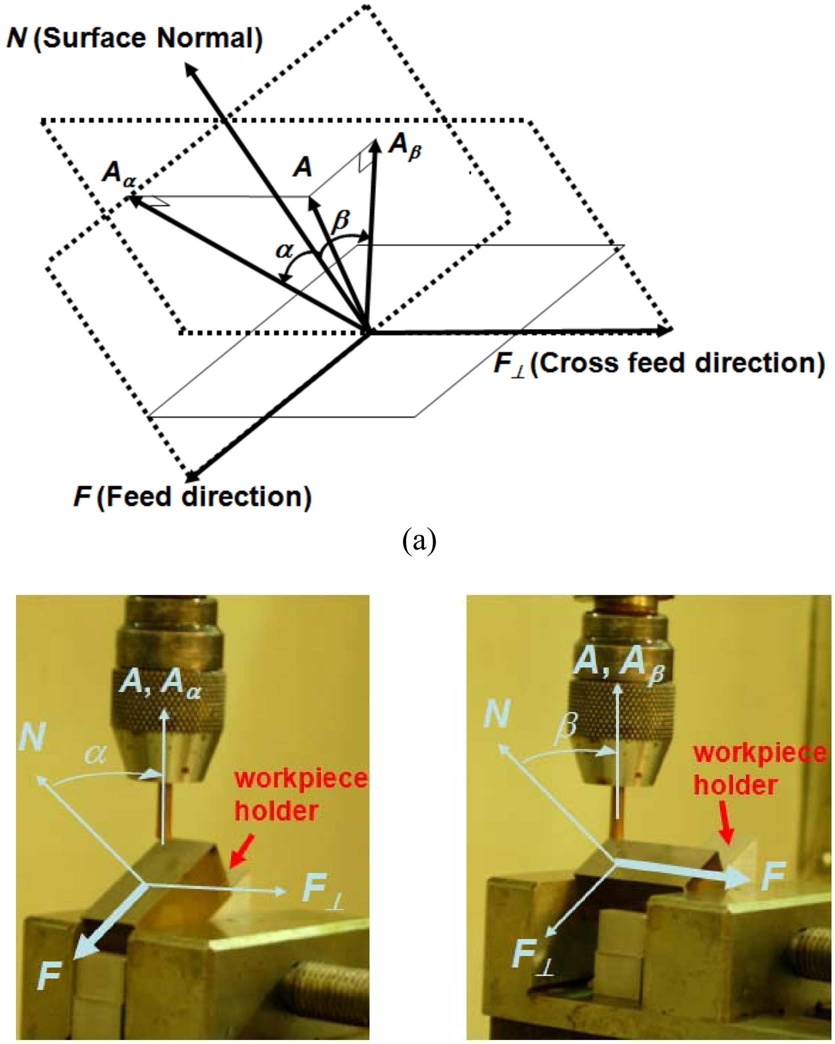

(a)

(b) (c)

Figure 2.1. (a) The lead angle, $\alpha$, and tile angle, $\beta$, and experimental setup (b) lead angle $\alpha$ (with tilt angle $\beta = 0°$) and (c) tilt angle $\beta$ (with lead angle $\alpha = 0°$).

Figures 2.1(b) and (c) illustrate the experimental setup to investigate the effects of $\alpha$ and $\beta$, respectively. Figure 2.1(b) shows the setup for the variable lead angle test with $\boldsymbol{A} = \boldsymbol{A}_{\alpha}$ and $\beta = 0°$. In the study, the negative lead angle configurations are investigated. The workpiece is placed on the inclined workpiece holder to achieve the lead and tilt angles during EDM milling. Figure 2.1(c) shows the setup for the variable tilt angle test with $\boldsymbol{A} = \boldsymbol{A}_{\beta}$ and $\alpha = 0°$.

The EDM milling cuts straight slots, 21 mm in length and 0.5 mm in depth, on a flat surface. Three slots are machined under each EDM condition. Table 2.1 summarizes the EDM process parameters. The work-material is H13 tool steel. The electrode is a copper tube with 3.2 mm outer diameter and 1.6 mm inner diameter. Mist of kerosene in air with 5 ml/min flow rate is used as the dielectric fluid.

Table 2.1. Process parameters used for the near-dry EDM experiment.

| | |
|---|---|
| Electrode rotational speed (rpm) | 500 |
| Polarity | Negative |
| Open circuit voltage $u_i$ (V) | 200 |
| Pulse duration $t_i$ (μs) | 4 |
| Pulse interval $t_o$ (μs) | 8 |
| Discharge current $i_e$ (A) | 20 |
| Gap voltage $u_e$ (V) | 60 |

The weight of the workpiece and electrode before and after the machining are measured using an Ohaus GA110 digital scale with 0.1 mg resolution to calculate the tool electrode wear ratio ($\eta$) and *MRR*. Based on the weight measurements, $\eta$ and *MRR* are calculated as follows:

$$\eta = \frac{\Delta m_{electrode} / \rho_{electrode}}{\Delta m_{workpiece} / \rho_{workpiece}} \tag{2-1}$$

$$MRR = \frac{\Delta m_{workpiece} / \rho_{workpiece}}{t} \tag{2-2}$$

where $\rho_{electrode}$ and $\Delta m_{electrode}$ are the density and mass change of electrode, respectively, $\rho_{workpiece}$ and $\Delta m_{workpiece}$ are the density and mass change of workpiece, respectively, $t$ is the time to machine the slot. In this study, $\rho_{workpiece}$ is 7800 kg/m$^3$ and $\rho_{electrode}$ is 8933 kg/m$^3$. A Taylor Hobson profilometer with 2 μm diamond stylus tip radius is used to measure the surface roughness along the slot. The arithmetical average roughness ($R_a$) is selected as the surface roughness parameter. The average of three measured $R_a$ values is used to represent the surface roughness of the machined slot.

Three sets of experiments were conducted to investigate the effects of electrode orientation and mist inlet pressure. The case with $\alpha$ = 0°, $\beta$ = 0°, and 483 kPa inlet pressure is set as the base model to compare the experiment and simulation results. In experiment I, $\alpha$ is varied from 0 to –30° with –5° increments while constraining $\beta$ = 0° and inlet pressure at 483 kPa. In experiment II, $\beta$ is varied 0° to 30° with 5° while constraining $\alpha$ = 0° and inlet pressure at 483 kPa. In experiment III, the inlet pressure is varied from 276 to 552 kPa with 69 kPa increments while constraining both $\alpha$ and $\beta$ at zero.

## 2.3 CFD Model

CFD analysis of the air and kerosene mist flow through the discharge gap between the tubular electrode and workpiece in near-dry EDM milling was conducted to calculate the flow rate and correlate to the *MRR* under different electrode orientations and inlet pressure.

### 2.3.1 Assumptions

The flow of compressible air and incompressible kerosene liquid mixture is simulated by using the Fluent Ver. 6.2.16 laminar flow solver. To model the mixture flow, a volume of fluid (VOF) model with implicit scheme is utilized. The VOF model uses volume fraction of air and kerosene in the control volume to compute Navier-Stokes equations. Physical parameters of air and kerosene are listed in Table 2.2. Properties are assumed to be at room temperature and temperature-independent.

Table 2.2. Properties of air and kerosene.

| **Parameter** | **Air** | **Kerosene** |
|---|---|---|
| Density $\rho$ (kg/m$^3$) | Ideal-gas (variable) | 780 |
| Specific heat $c_p$ (J/kg-K) | 1006.43 | 2090 |
| Thermal conductivity $\kappa$ (w/m-K) | 0.0242 | 0.149 |
| Viscosity $\mu$ (kg/m-s) | 0.0000179 | 0.0024 |

Using the VOF model, continuity equations for air and kerosene have following form (FLUENT Manual, 2003).

$$\frac{1}{\rho_a}\left[\frac{\partial}{\partial t}\nabla\cdot\left(\rho_a\vec{\upsilon}_a\right)\right]+\nabla\cdot\left(\gamma_a\rho_a\vec{\upsilon}_a\right)=S_{\gamma_a}+\dot{m}_{ka}-\dot{m}_{ak} \tag{2-3}$$

$$\frac{1}{\rho_k}\left[\frac{\partial}{\partial t}\nabla\cdot(\rho_k\vec{\upsilon}_k)\right]+\nabla\cdot(\gamma_k\rho_k\vec{\upsilon}_k)=S_{\gamma_k}+\dot{m}_{ka}-\dot{m}_{ak} \tag{2-4}$$

where $\rho_a$ is the density of air, $\rho_k$ is the density of kerosene, $\vec{\upsilon}_a$ is the velocity of air, $\vec{\upsilon}_k$ is the velocity of kerosene, $\gamma_a$ is the volume fraction of air in the control volume, $\gamma_k$ is the volume fraction of kerosene in the control volume, $S_{\gamma_a}$ mass source of air, $S_{\gamma_k}$ mass source of kerosene, $\dot{m}_{ka}$ is mass transfer from kerosene to air, and $\dot{m}_{ak}$ is mass transfer from air to kerosene. Since each phase share the same control volume, following constraint is applied.

$$\gamma_a+\gamma_k=1 \tag{2-5}$$

Single momentum equation is solved for the VOF model. The velocity field is assumed to be shared among each phase as following:

$$\frac{\partial}{\partial t}(\rho\vec{\upsilon})+\nabla\cdot(\rho\vec{\upsilon}\vec{\upsilon})=\nabla p+\nabla\cdot\left[\mu\left(\nabla\vec{\upsilon}+\nabla\vec{\upsilon}^T\right)\right]+\rho\vec{g}+\vec{F} \tag{2-6}$$

where $\rho$ is the density of fluid mixture, $\vec{\upsilon}$ is the velocity of fluid mixture, $\mu$ is the viscosity of fluid mixture, $p$ is the pressure, $\vec{g}$ is the gravitational force and $\vec{F}$ is the external force. The density, velocity, and viscosity of fluid mixture are expressed as summation of volume fraction of each phase as following:

$$\rho = \gamma_a \rho_a + \gamma_k \rho_k \tag{2-7}$$

$$\vec{\upsilon} = \gamma_k \vec{\upsilon}_k + \gamma_k \vec{\upsilon}_k \tag{2-8}$$

$$\mu = \gamma_k \mu_k + \gamma_k \mu_k \tag{2-9}$$

where $\rho_a$ is the density of air, $\rho_k$ is the density of kerosene, $\vec{\upsilon}_a$ is the velocity of air, $\vec{\upsilon}_k$ is the velocity of kerosene, $\mu_a$ is the viscosity of air, and $\mu_k$ is the viscosity of kerosene. When large difference exists among phases, the VOF model lacks accuracy since the velocity field is shared to solve the momentum equation.

Similar to the momentum equation, single energy equation is solved for VOF model as following:

$$\frac{\partial}{\partial t}(\rho E) + \nabla \cdot (\vec{\upsilon}(\rho E + p)) = \nabla \cdot (\kappa \nabla T) \tag{2-10}$$

where E is energy, $\kappa$ is thermal conductivity and $T$ is the temperature of the mixture. Energy is computed using mass average and thermal conductivity is computed using volume fraction as following:

$$E = \frac{\gamma_a \rho_a E_a + \gamma_k \rho_k E_k}{\gamma_a \rho_a + \gamma_k \rho_k} \tag{2-11}$$

$$\kappa = \gamma_k \kappa_k + \gamma_k \kappa_k \tag{2-12}$$

where $E_a$ is energy of air, $E_k$ is energy of kerosene, $\kappa_a$ is thermal conductivity of air, and $\kappa_k$ is thermal conductivity of air energy of kerosene. Energy of air and kerosene is expressed as following function:

$$E_a = \int_{T_{ref}}^{T} c_{p_a} dT - \frac{p}{\rho_a} + \frac{\upsilon_a^{\,2}}{2} \tag{2-13}$$

$$E_k = \int_{T_{ref}}^{T} c_{p_k} dT - \frac{p}{\rho_k} + \frac{\upsilon_k^{\,2}}{2} \tag{2-14}$$

where $c_{p_a}$ is specific heat of air, $c_{p_k}$ is specific heat of kerosene, and $T_{ref}$ is the reference temperature (298.15 K).

The pressure regulated air and flow rate regulated kerosene were supplied to the inlet of the tubular electrode. The inlet for the mist is set as mass flow boundary condition due to the limitation of available inlet boundary condition for the mixture of gas and liquid in Fluent. Since 99.99% of the volume and about 75% of the mass of the mist is occupied by the air in this study, the mass flow rate inputs of air are taken from the air only solutions with the pressure inlet boundary condition. The kerosene mass flow of 5 ml/min is added in the inlet to have the combined air and kerosene mass flow rate boundary condition for all simulation cases. The outlet boundaries that touch the atmosphere are set as pressure outlet at 0 Pa. Boundaries that touch the electrode are set as walls that rotate at 500 rpm. Boundaries that touch workpiece are set as stationary walls

### 2.3.2 EDM Gaps and Main Discharge Region

The electrode orientation relative to workpiece determines the control volume for CFD analysis. Cross-sectional views of workpiece and electrode along electrode centerline and feed direction for experiment I are shown in Figures 2.2(a), (b) and (c) to illustrate the setups with $\beta = 0°$ and $\alpha = 0°, -10°$, and $-30°$, respectively. The discharge gap between the electrode and workpiece is assumed as 30 μm, which is estimated from the experimental measurement.

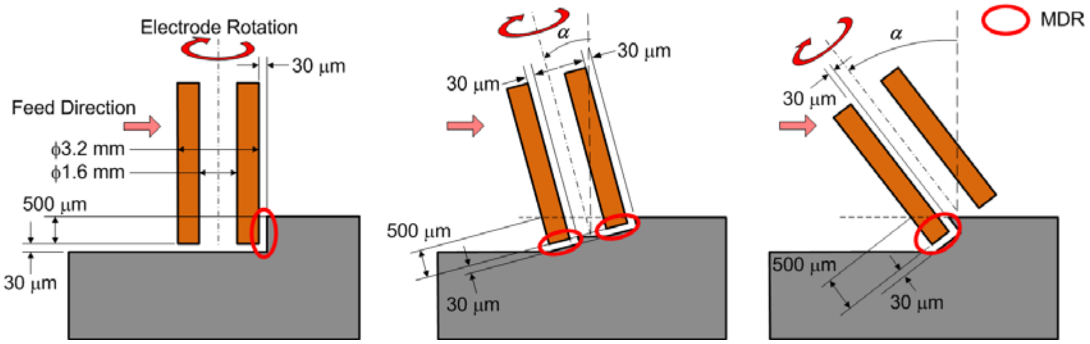

(a) (b) (c)

Figure 2.2. Cross-section of workpiece and electrode along electrode centerline and feed direction and the main discharge region (MDR, represented by circles) for experiment I: (a) $\alpha = 0°$, (b) $\alpha = -10°$, and (c) $\alpha = -30°$.

In EDM milling, the majority of material removal occurs in the main discharge region (MDR). Feed direction, electrode orientation, depth of cut, unmachined workpiece geometry, and step over distance, which is the size of electrode diameter engaged in milling, determine the MDR. The MDR for $\alpha = 0°, -10°$, and $-30°$ in experiment I is marked by circle in Figures 2.2(a) to (c). When $\alpha = 0°$, as shown in Figure 2.2(a), discharges mainly occur at the leading outer face of the electrode below the unmachined workpiece surface. Figure 2.2(a) also illustrates that MDR is the discharge gap excluding the bottom of the electrode. For $\alpha = -10°$ in Figure 2.2(b), MDR is located at the bottom face, leading outer face and trailing inner face of the electrode below the unmachined workpiece surface. When $\alpha$ is further decreased, such as $\alpha = -30°$ in Figure 2.2(c), MDR is moved to the trailing inner face and the portion of bottom face below the unmachined workpiece surface.

Figure 2.3 shows the cross-section views of workpiece and electrode along electrode centerline and cross feed direction for experiment II. Figures 2.3(a) and (b) show the MDR for small $\beta$, such as $\beta = 10°$, and large $\beta$, such as $\beta = 30°$, respectively. The MDR for experiment III is similar to the case when $\alpha = 0°$ and $\beta = 0°$ (Figure 2.2(a)). Discharges mainly occur in the leading front face of the electrode below the unmachined workpiece surface.

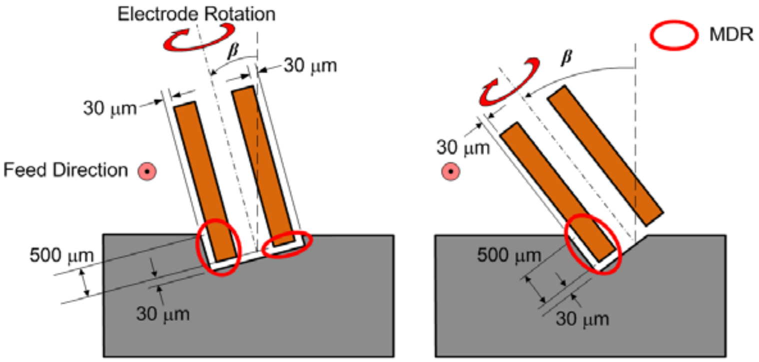

(a) (b)

Figure 2.3. Cross-section of workpiece and electrode along electrode centerline and cross feed direction for experiment II: (a) $\beta = 10°$ and (b) $\beta = 30°$.

### 2.3.3 Meshes for the Base Model

When $\alpha = 0°$ and $\beta = 0°$, the control volume is the simplest to model. However, it must be carefully meshed to avoid divergence solution and long computation time. The 3D models of the electrode and workpiece are created using the SolidWorks software, as shown in Figure 2.4(a). The mist flows through the electrode hole and discharge gap. The inverse of the solid model of the electrode and workpiece is used to generate the 3D control volume to model the flow region. The control volume is imported to Gambit 2.3.16 to create the 3D meshes as shown in Figure 2.4(b). The control volume is divided into six sub-regions, as shown in Figure 2.4(c). Segmenting the control volume to sub-regions enables to finely mesh the 30 μm gap regions in Figures 2.2(a), (b), and (c) and coarsely mesh non-gap regions. Mesh sizes in the gap region are varied to find the grid independence for solutions.

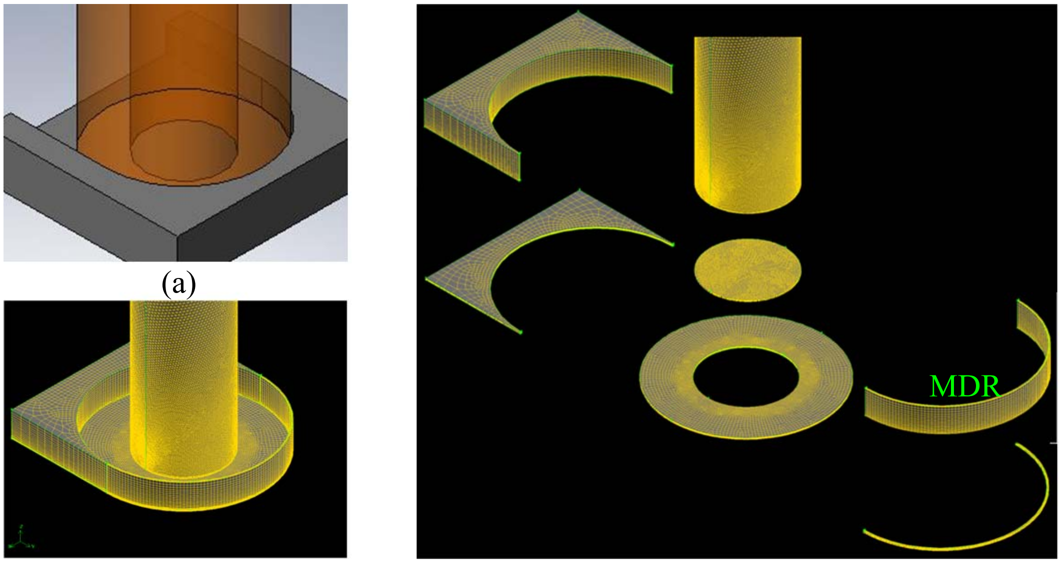

(a)

(b)

(c)

Figure 2.4. (a) 3D model of electrode and workpiece, (b) 3D meshes and (c) exploded view of meshes for $\alpha = 0°$ and $\beta = 0°$.

### 2.3.4 Meshes for Experiment I with $\alpha = -15^\circ$

Figures 2.5(a), (b), and (c) show the solid model of electrode and workpiece, meshes of the control volume, and exploded view of the control volume, respectively, for $\alpha = -15^\circ$ in experiment I. The MDR at the bottom and leading edge of the electrode, corresponding to the MDR marked in Figure 2.2(b), is shown in Figure 2.5(c). The complexity of the control volume and meshes is considerably higher than the base model with $\alpha = 0^\circ$ and $\beta = 0^\circ$. Breaking down the control volume to smaller sub-regions enables to mesh the control volume more efficiently.

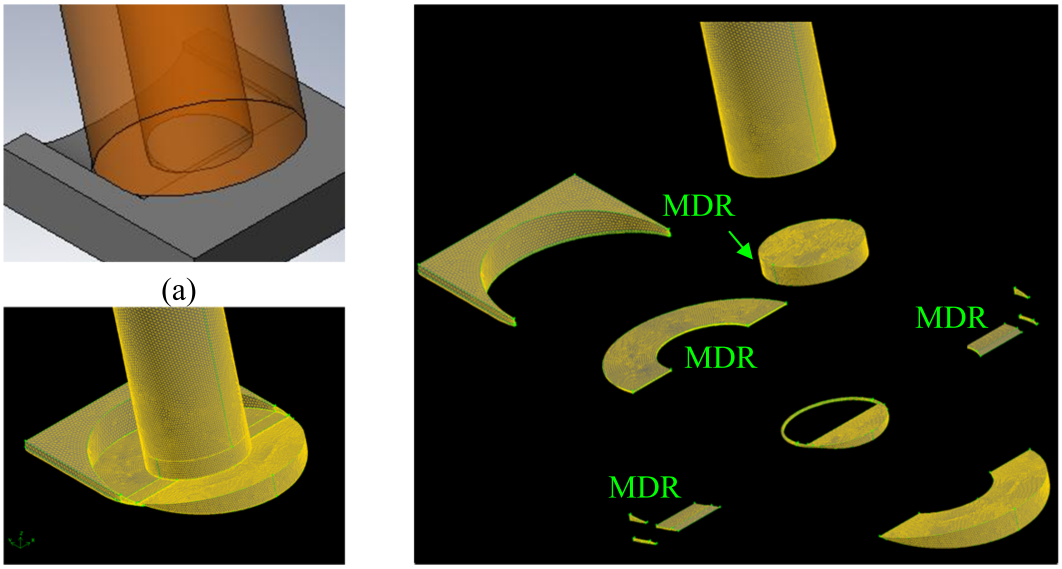

(a)

(b)

(c)

Figure 2.5. (a) 3D model of electrode and workpiece, (b) 3D meshes, and (c) exploded view of meshes for $\alpha = -15^\circ$ and $\beta = 0^\circ$.

For experiment I, the 3D meshes and pictures of machined surface with quick stop of the electrode to show the electrode orientation effect for seven machining configurations of $\alpha$ from 0° to –30° in –5° increment are shown in Figure 2.6. These pictures validate the concept on MDR and geometric relationships between the workpiece and electrode. When $\alpha = -5°$ and $-10°$, a circular profile is observed at the end of the slot. This corresponds to discharge gaps at the bottom face, leading outer face and trailing inner face of the electrode. As $\alpha$ further decreases, the circular profile becomes discontinuous and eventually disappears. As $\alpha$ becomes excessively small (lower than –20°), the discharge only occurs at the inner trailing edge and a part of bottom end of electrode due to the electrode orientation relative to the workpiece surface.

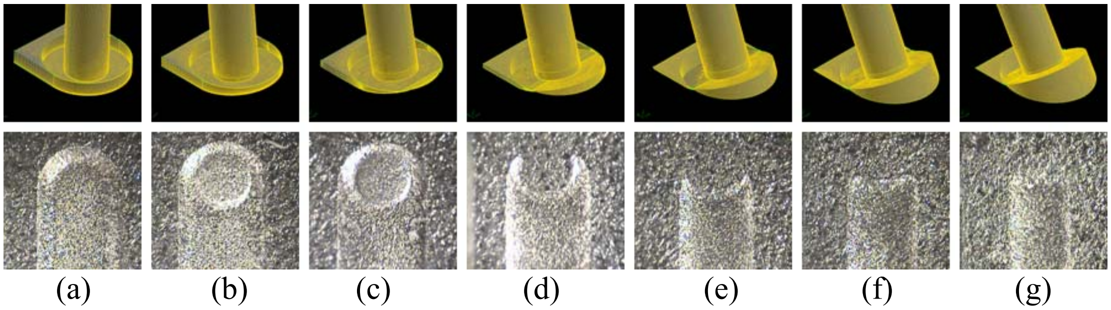

Figure 2.6. CFD 3D meshes and profiles of the machined surface at the end of cut for $\alpha$ = (a) 0°, (b) –5°, (c) –10°, (d) –15°, (e) –20°, (f) –25° and (g) – 30°.

### 2.3.5 Meshes for Experiment II with $\beta = 15°$

The 3D model of electrode and workpiece, 3D meshes of the control volume, and exploded view of broken down control volume for $\alpha = 0°$ and $\beta = 15°$ in experiment II are shown in Figure 2.7. The MDR at leading edge of the electrode, corresponding to the MDR marked in Figure 2.3(a), is shown in Figure 2.7(c). The 3D meshes and pictures of machined surface with quick stop of electrode for $\beta$ from 0° to 30° in 5° increment are shown in Figure 2.8. In experiment II, no circular profiles are observed at the end of slot. It corresponds to discharges mainly occurring at the leading front face of the electrode below the unmachined workpiece surface. Similar to experiment I, pictures in Figure 2.8

further confirm the MDR.

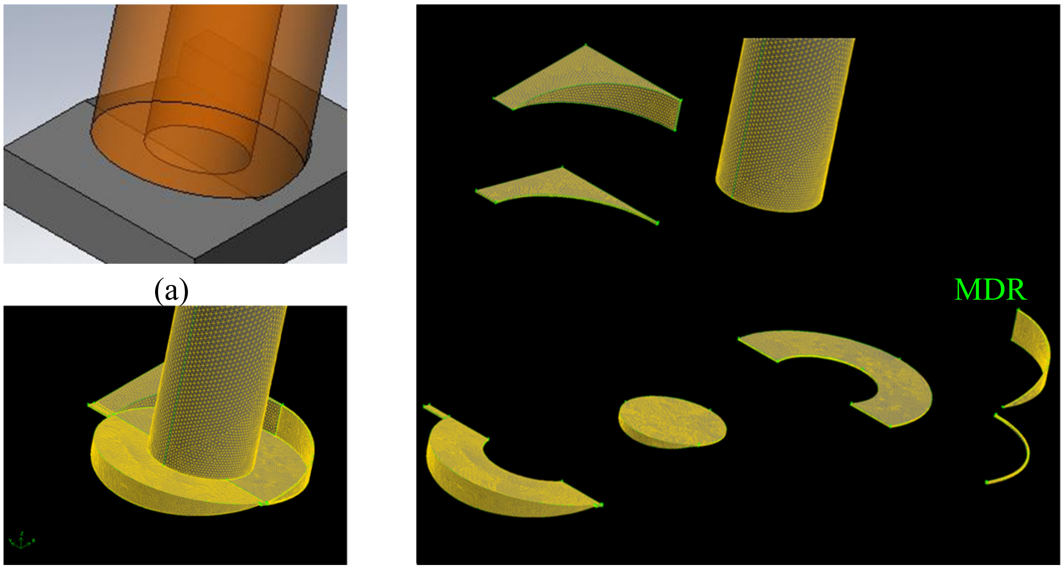

(a)

(b)

(c)

Figure 2.7. (a) 3D model of electrode and workpiece, (b) 3D meshes and (c) exploded view of meshes for $\alpha = 0°$ and $\beta = 15°$.

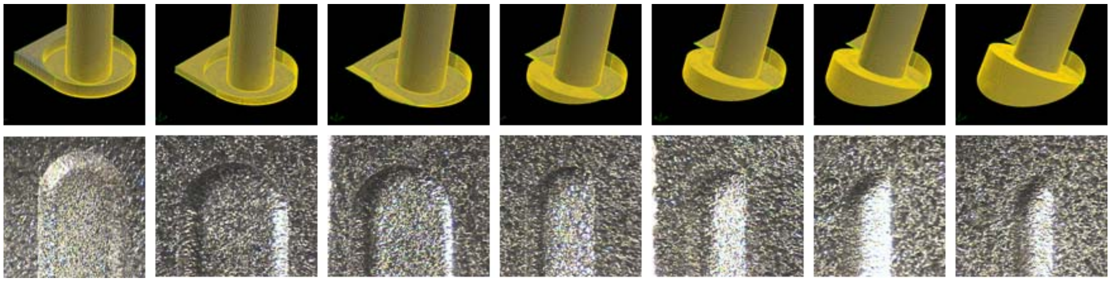

(a) (b) (c) (d) (e) (f) (g)

Figure 2.8. CFD 3D meshes and profiles of the machined surface at the end of cut for $\beta =$ (a) 0°, (b) 5°, (c) 10°, (d)15°, (e) 20°, (f) 25° and (g) 30°.

### 2.3.6 Mesh Size for Gap Region

The CFD mesh size is critical to the accuracy of predicted fluid flow rate in MDR and also affects the computational time. Meshes cannot be too coarse, which causes problem in accuracy, or too fine, which costs high computational time and may result divergence. Grid independence is achieved when the change in mesh size has resulted in insignificant variation of analysis results. The spacing between grids on perimeters along gap regions is varied as 0.05, 0.033 and 0.025 mm. The number of grids along the 30 μm gap is also varied as 3, 5, 7 and 9. The mass flow rate of the fluid through MDR was used as the criterion for grid independence evaluation. To save computation time for grid independence check, the flow was computed only with compressible air (no mist).

Table 2.3 shows the deviation of the mass flow rate of compressible air through the MDR for the base model ($\alpha = 0°$ and $\beta = 0°$) referenced at 5 grids in the 30 μm gap and 0.033 mm grid spacing along perimeters. The two extreme cases of very fine and very coarse mesh are not considered in the analysis. When the number of grids along the 30 μm gap is 7, the analysis results are within 2% mass flow rate variation for three grid intervals along perimeters. However, the computational cost is a trade off. To save the computational cost, the number of grids along the 30 μm gap is reduced to 5 and the grid interval along perimeters is increased until 2% variation is attained. When the number of grids along the 30 μm gap is 5 and grid interval along the perimeter is less than 0.033 mm, the computation time reduces and the solution variation is still less than 2% when the mesh becomes finer. The same procedure is carried out to investigate the grid independence for all cases in experiments I and II with 5 and 7 grids in the 30 μm gap, and 0.05, 0.033 and 0.025 mm grid interval along perimeters. The coarsest mesh size that attained 2% variation when the mesh becomes finer for all cases was 5 grids along the 30 μm gap and 0.033 mm grid interval along the perimeters. Hence in this study, the same CFD mesh size with 5 grids along the 30 μm gap and 0.033 mm grid interval along the perimeters is used for gap regions.

Table 2.3. Deviation of the air mass flow rate through MDR (reference at 5 grids along gap direction and 0.033 mm grid interval along the perimeter) for the base model ($\alpha = 0°$ and $\beta = 0°$).

| Number of grids in the gap direction | Grid interval along perimeters (mm) 0.05 | 0.033 | 0.025 |
|---|---|---|---|
| 3 | -- | –4.68% | –5.79% |
| 5 | –5.79% | 0.0% | –1.01% |
| 7 | 1.90% | 0.86% | 0.08% |
| 9 | 2.49% | 1.16% | -- |

### 2.3.7 Mesh Size for Non-Gap Region

For the mesh not in the gap region, the mesh size varies in different regions. To avoid sudden changes in the mesh size, the grid spacing for edges that touch the gap region is matched with the gap region. Grids on other edges are non-uniformly placed to mesh the control volume away from the gap region coarsely to reduce the computational cost. The mass flow rate through each pressure outlet is used as the grid independence criterion. This process is repeated until less than 2% deviation in mass flow rate is attained.

## 2.4 Results and Discussions

Experimental measurements of *MRR*, tool wear, and surface roughness and CFD analysis of MDR mist flow rate for kerosene in air mist in experiments I, II, and III are presented and compared in the following three sections.

### 2.4.1 Experiment I Results

The CFD model predicted fluid speed, volume fraction of kerosene, and mist density for $\alpha$ = –5° and –15° are compared in Figure 2.9. As shown in Figure 2.9(a), when $\alpha$ = –5°, high speed mist flows through the MDR at about 350 m/s. However, when $\alpha$ = –15°, mist escapes to the non-MDR region. The volume fraction of kerosene and the density of mist drastically decrease as $\alpha$ decreases from –5° to –15°, as shown in Figures 2.9(b) and (c), due to the mist escaping from the electrode hole exposed to open atmosphere.

Experiment I results of the effects of $\alpha$ on the CFD predicted mist flow through MDR and experimentally measured *MRR*, $\eta$, and $R_a$ are shown in Figures 2.10(a), (b), (c), and (d), respectively. As seen in Figure 2.10(a), the mist flow rate through MDR was the highest when $\alpha$ = –5° and –10° and it started to decrease as $\alpha$ decreased. From Figure 2.10(b), the *MRR* was also the highest when $\alpha$ = –5° and started to decrease when $\alpha$ became less than –5°. When $\alpha$ = –5° and –10°, all the mist has to flow through the MDR. However, as $\alpha$ further decreases, the mist can escape from electrode hole exposed in open atmosphere due to the geometric configuration. When more dielectric fluid flows through the discharge gap, debris can be flushed away more effectively. Since less debris floats in the discharge gap, the conductivity of the dielectric medium in MDR decreases and the number of stable discharges increases. Stable discharges increase the average gap voltage and the electrode retracts less often. As the result, an increase in the *MRR* is observed. When less dielectric fluid flows through the discharge gap, debris accumulates in the MDR and dielectric conductivity decreases. The decrease in dielectric conductivity causes more arcing and drop in the average gap voltage. As the result, the electrode retracts more often and *MRR* decreases.

Increase of $\eta$ was observed for $\alpha$ smaller than –20°, as seen in Figure 2.10(c). When the mist flow rate through the MDR is small, the debris tends to contaminate the gap and increases the conductivity of dielectric medium in the discharge gap. Due to the drop in dielectric conductivity, the probability of arcing increases. Arcing damages the electrode and thus increases $\eta$.

The surface roughness $R_a$ is the lowest (2.4 μm) when $\alpha = 0°$, as shown in Figure 2.10(d). When $\alpha$ is not zero, $R_a$ rapidly increases by about three times to over 7 μm. The sudden increase in $R_a$ is caused by the geometric configuration between the electrode and workpiece. When the electrode is oriented perpendicular to the workpiece surface, the entire bottom surface of the electrode machines the workpiece. Since a constant gap distance is maintained between the entire bottom face of the electrode for machining, the surface roughness is better. When the electrode is tilted ($\alpha$ is not equal to 0°), only the trailing outer edge machines the surface and results higher surface roughness.

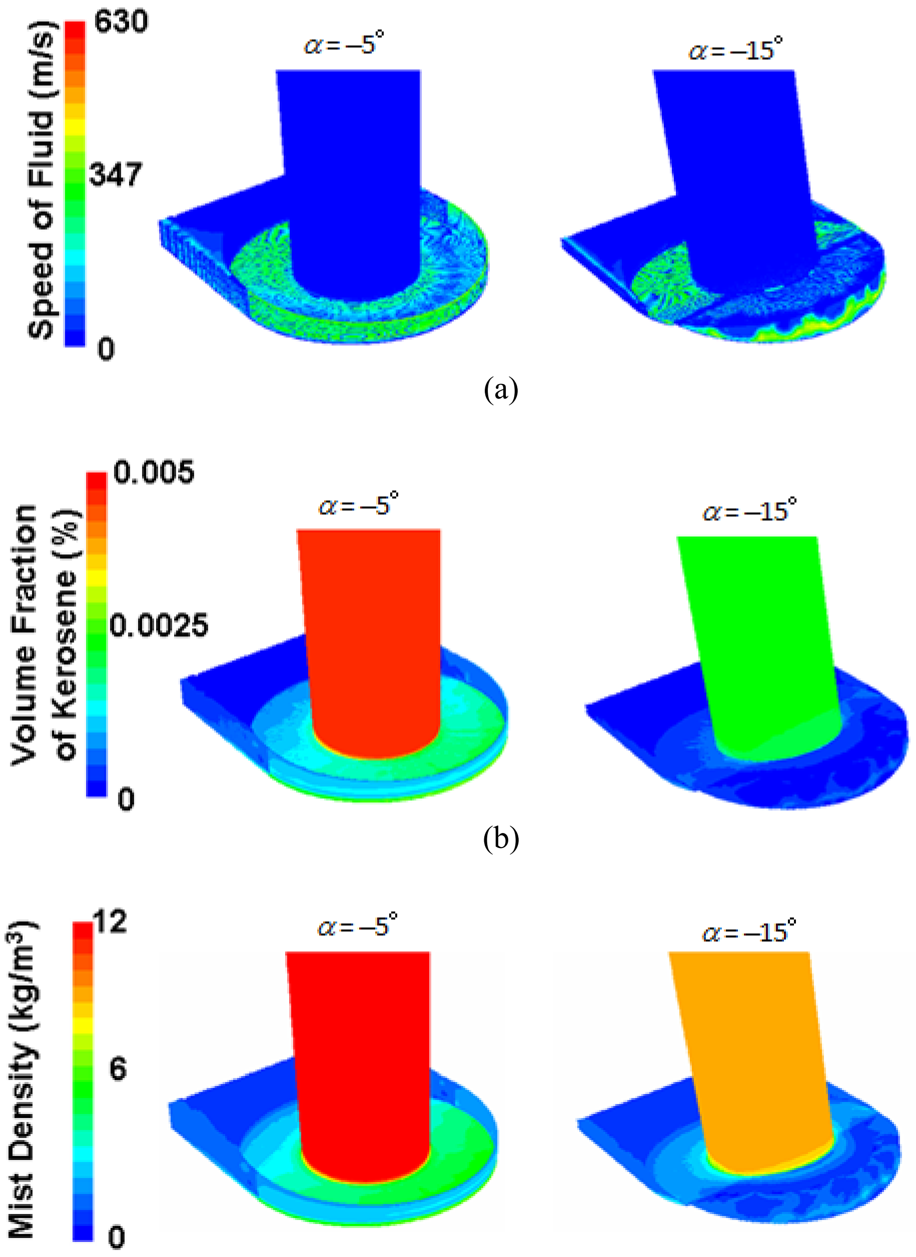

(a)

(b)

(c)

Figure 2.9. CFD simulation results for (a) fluid speed, (b) volume fraction of kerosene, and (c) mist density for $\alpha = -5°$ and $-15°$ in experiment I.

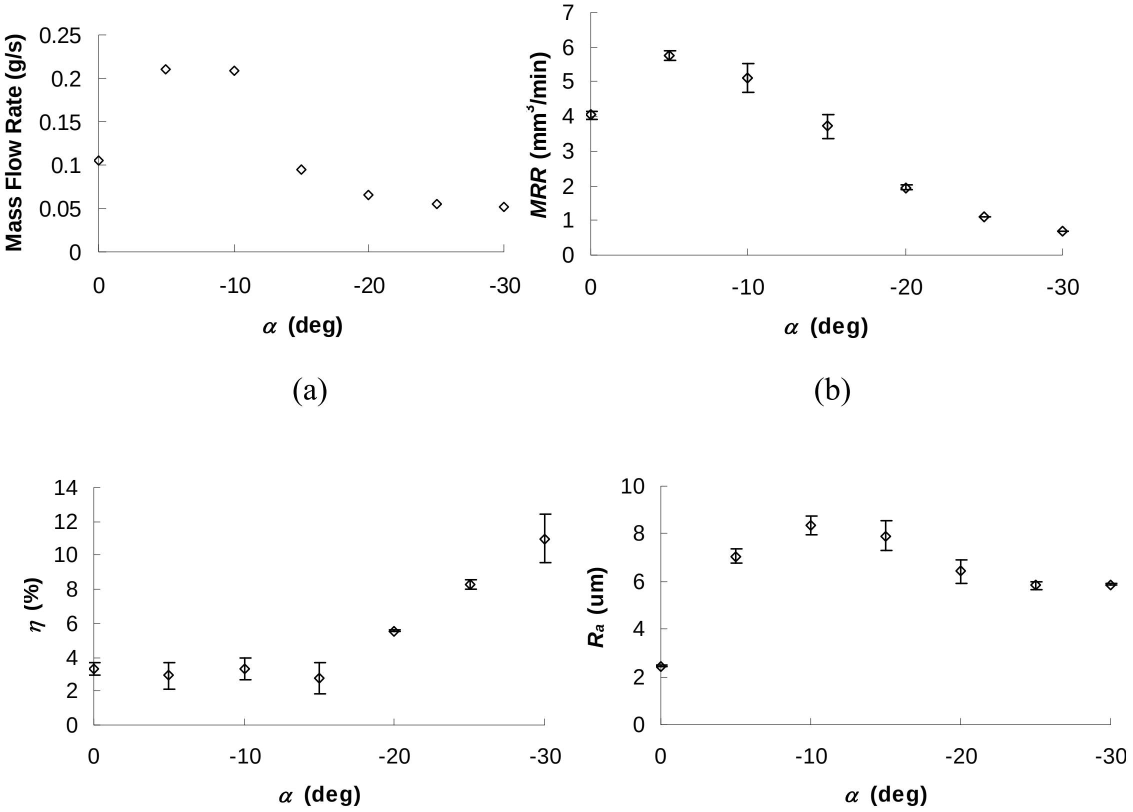

(a) (b)

(c) (d)

Figure 2.10. Experiment I results - effects of $\alpha$ on (a) simulated mist flow (b) *MRR*, (c) $\eta$, and (d) $R_a$.

Effects of mist flow rate through MDR on *MRR*, $\eta$, and $R_a$ are plotted in Figures 2.11(a), (b), and (c), respectively, along with the data from experiments II and III, which will be discussed in the next two sections. For experiment I (represented by solid diamond symbols), the mist flow rate through MDR and *MRR* are almost linearly related to each other. The tool electrode wear ratio, $\eta$, is inversely related to the mist mass flow rate through MDR. $R_a$ does not have any relationship to the mist flow rate through MDR as shown in Figure 2.11(c).

Figure 2.12 plots the relationship between *MRR* and $\eta$, along with the data from experiments II and III. The data in experiment I, also represented by solid diamond symbols, shows almost inverse relationship to each other. When discharge parameters, such as spark on-time $t_i$, spark off-time $t_o$, discharge current $i_e$, and gap voltage $u_e$, are fixed, the discharge gap conditions determine the $MRR$ and $\eta$. Since the optimum $\alpha$ maximized $MRR$, minimized $\eta$, and severely damaged surface roughness, the $\alpha$ is best used for roughing in five-axis near-dry EDM milling. In this study, for the 0.5 μm depth of cut, such optimal $\alpha$ is about –5°.

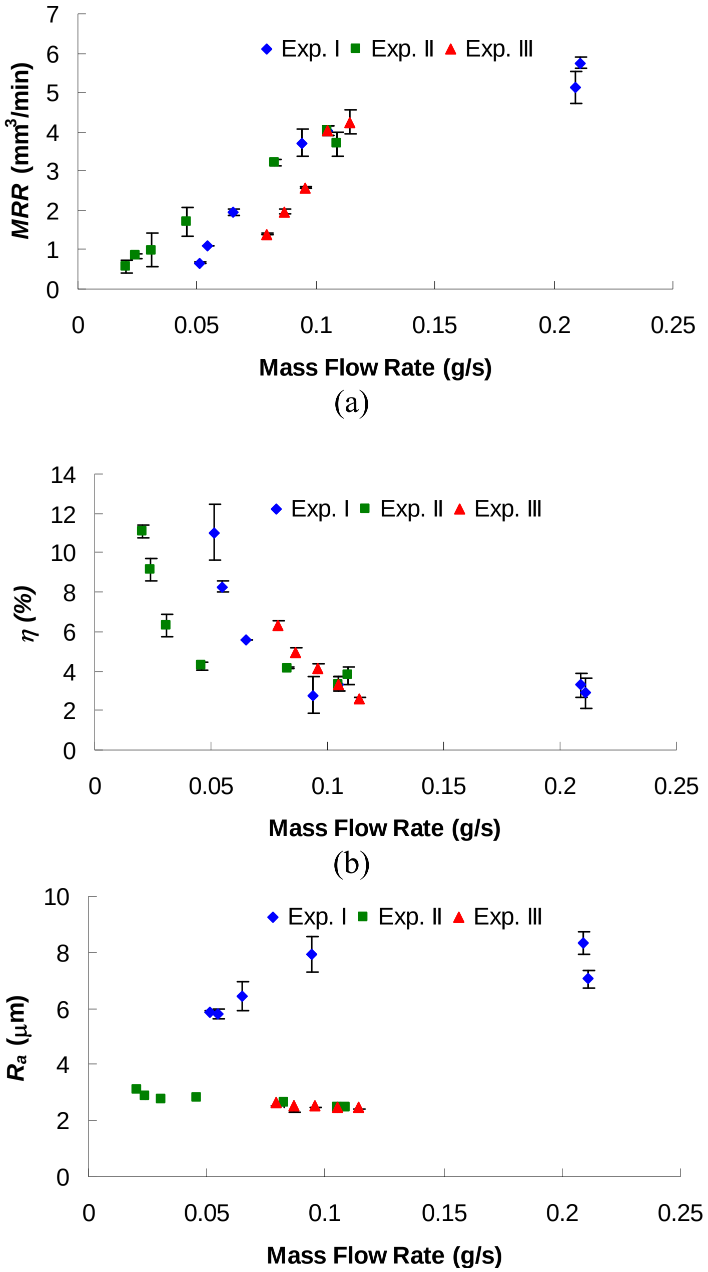

(a)

(b)

(c)

Figure 2.11. Effects of mist mass flow rate through MDR on (a) *MRR*, (b) $\eta$, and (c) $R_a$.

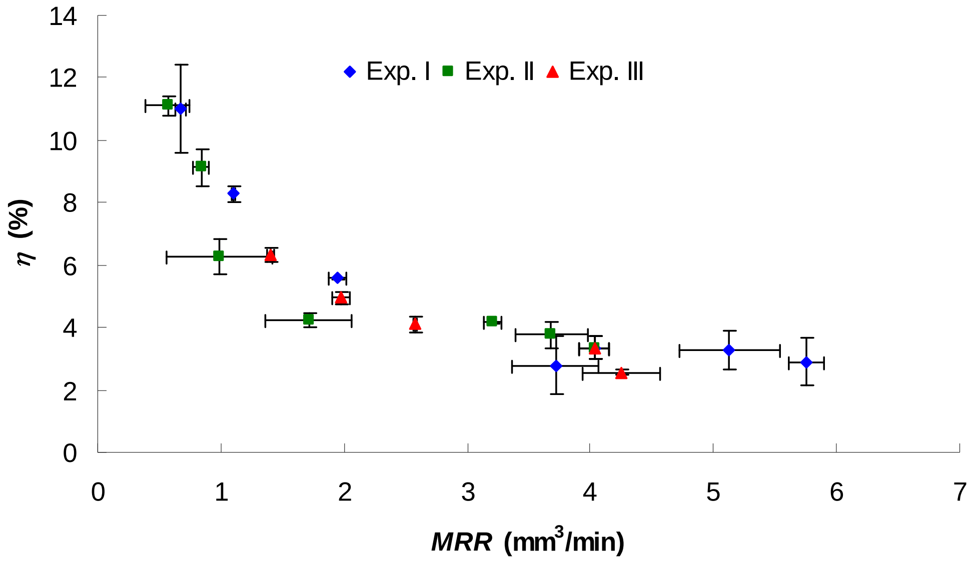

Figure 2.12. *MRR* vs $\eta$.

### 2.4.2 Experiment II Results

The effects of $\beta$ on CFD predicted mist flow rate through MDR and experimentally measured *MRR*, $\eta$, and $R_a$ in experiment II are shown in Figures 2.13(a), (b), (c), and (d), respectively. Figure 2.13(a) shows that the mist flow rate slightly increased when $\beta$ is changed from 0 to 5°, but the mist flow rate started to decrease as $\beta$ further increased beyond 5°. The highest *MRR* occurred at $\beta = 0°$ and started to decrease as $\beta$ increased, as shown in Figure 2.13(b). Like in experiment I, the change in the geometric configuration between the workpiece and electrode due to $\beta$ alters the mist flow rate. When $\beta$ was 5° or 10°, only a small fraction of the mist flow through non-MDR region. However, as $\beta$ further increased, a large fraction of mist flowed through the electrode hole exposed to the open atmosphere. This decrease in the mass flow into the discharge region reduces *MRR* and increases $\eta$, as seen in Figures 2.13(b) and (c), respectively. The geometric configuration between the workpiece and electrode at the bottom of electrode for different tilt angles is similar to that of $\beta = 0°$; therefore, the $R_a$ remains about 2.5 to 3 μm in experiment II.

The mist flow rate through the MDR and *MRR* are also linearly correlated to each other in experiment II, as shown by the solid square symbols in Figure 2.11(a). Figure 2.11(b) shows that the $\eta$ is also almost inversely related to the mass flow rate through MDR. $R_a$ is not correlated to the mass flow rate as seen in Figure 2.11(c). These trends are the same as in experiment I.

As shown by the solid square symbols for experiment II in Figure 2.12, the $\eta$ is also almost inversely related to the *MRR*. Since the increase in $\beta$ does not improve *MRR* and $\eta$, and does not heavily influence $R_a$, $\beta$ can be used to avoid gouging in finishing EDM milling. In finishing, *MRR* and $\eta$ are traded off to avoid gouging while maintaining low $R_a$

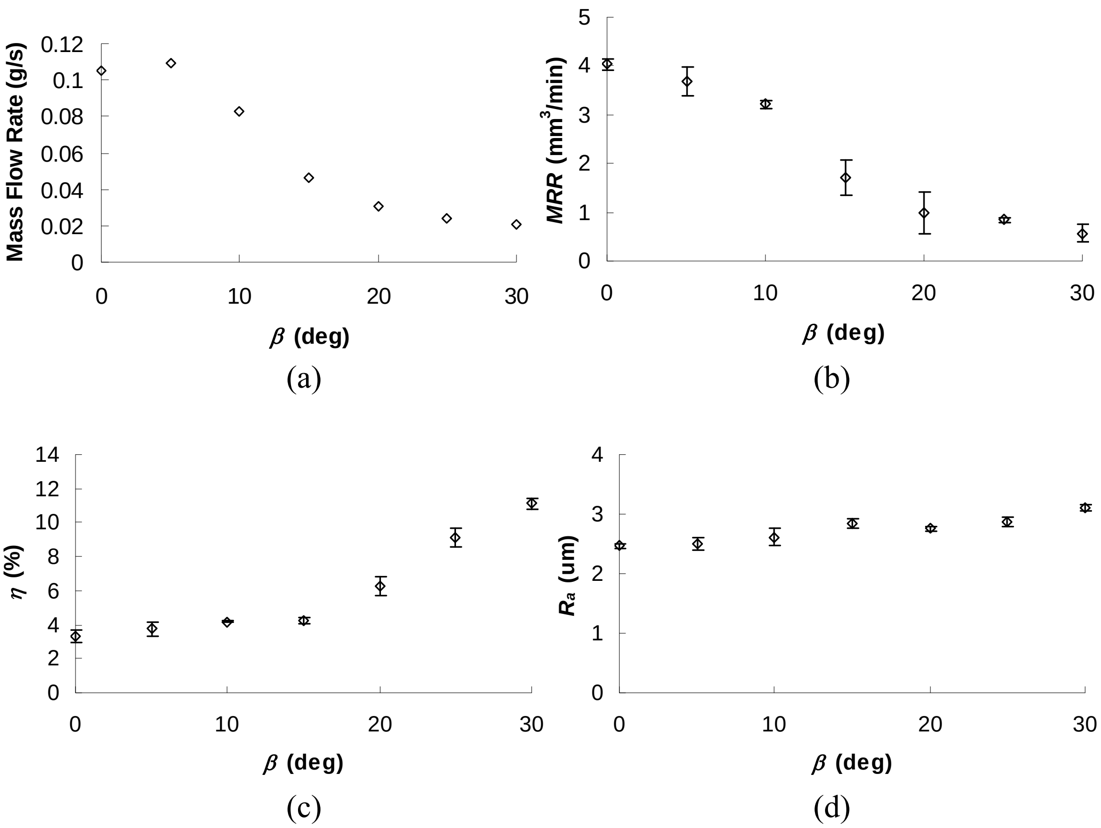

Figure 2.13. Experiment II results - effects of $\beta$ on (a) simulated mist flow and experimentally measured (b) $MRR$, (c) $\eta$, and (d) $R_a$.

### 2.4.3 Experiment III Results

Experiment III identifies the effects of inlet pressure while maintaining $\alpha$ and $\beta$ at 0°. The experimental results only reflect the effects of mist flow rate. The effects of inlet pressure on the mist flow through MDR, $MRR$, $\eta$, and $R_a$ for experiment III are shown in Figure 2.14. Increasing the inlet pressure positively affects the mass flow of the mist in MDR (Figure 2.14(a)) and $MRR$ (Figure 2.14(b)). For $\eta$, as shown in Figure 2.14(c), the increase in inlet pressure reduces the $\eta$ in an almost linear fashion. Compared with results from experiments I and II, the effect of mass flow rate of mist through MDR on machining performance is weaker in experiment III. It may be due to the geometric configuration of workpiece and electrode. The inlet pressure does not affect $R_a$, which remains at about 2.5 μm, as seen in Figure 2.14(d). This confirms the observations in experiments I and II that geometric configuration between the workpiece and electrode is the key factor that affects the surface finish.

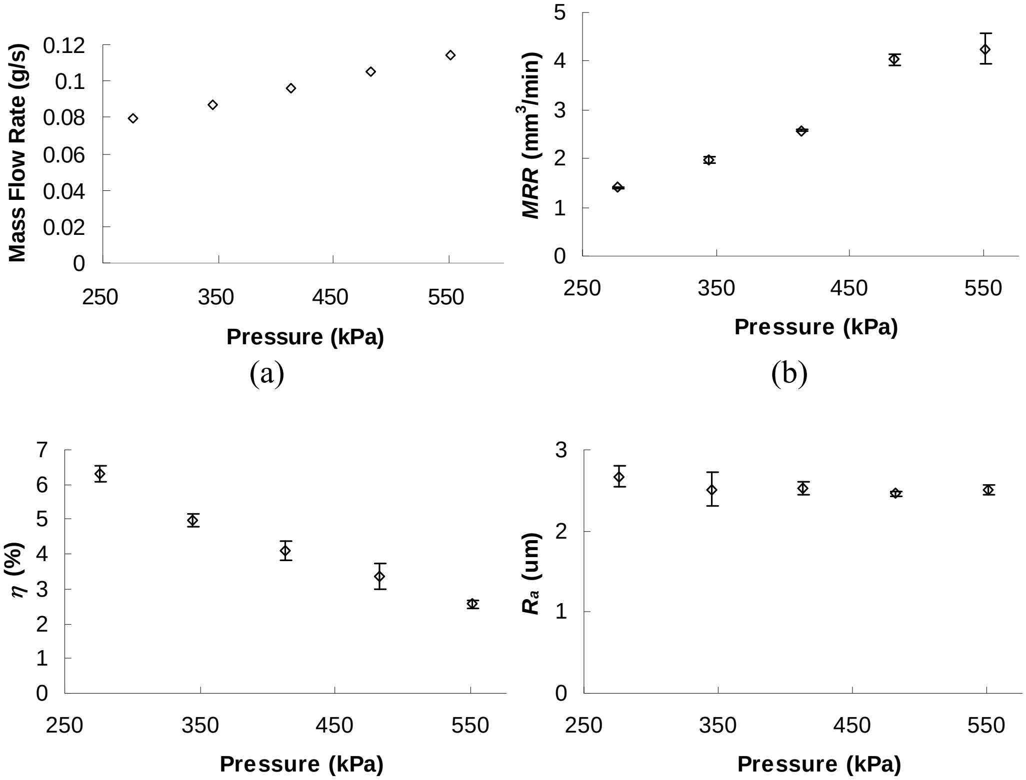

(a) (b)

(c) (d)

Figure 2.14. Experiment III results - effects of inlet pressure on (a) simulated mist flow (b) *MRR*, (c) $\eta$, and (d) $R_a$.

Triangular data points in Figure 2.11 show the effects of mass flow rate through MDR on *MRR*, $\eta$, and $R_a$. It shows the same trends as observed for the data points from experiments I and II, that *MRR* is almost linearly related to the mass flow rate, $\eta$ is almost inversely related to the mass flow rate, and $R_a$ is not correlated to the mass flow rate.

Figure 2.12 shows the relationship between *MRR* and $\eta$ for experiment III (triangular symbol). It is almost inversely related to each other, which also matches the same trend observed in experiments I and II.

## 2.5 Concluding Remarks

CFD model of dielectric fluid flow in EDM milling was developed to predict the mist flow rate and correlated to the experimentally measured *MRR*, $\eta$, and $R_a$ in near-dry EDM milling. Comparison of modeling and experimental results showed the *MRR* was linearly proportional to mist mass flow rate through MDR, and $\eta$ was inversely related to the mist flow rate. The optimum $\alpha$ with high *MRR* maximized the mist mass flow rate through MDR and corresponded to low $\eta$ and high $R_a$. Modeling and experimental results showed that $\beta$ had a negative effects on the mist mass flow rate through MDR, *MRR*, and $\eta$. Unlike $\alpha$, $\beta$ did not affect $R_a$. The increase in the inlet pressure had positive effects in mist mass flow rate through MDR, *MRR,* and $\eta$. Similar to $\beta$, inlet pressure did not affect $R_a$. Compared with experiments with variation of $\alpha$ and $\beta$, the effect of mist flow rate through MDR was weak in the experiments with variation of inlet pressure. Further analysis of mist flow rate through MDR that incorporates the geometry of MDR is needed. The study indicated that $\alpha$ was useful for roughing and $\beta$ was useful to avoid gouging in finishing EDM milling. The results from this study could be further applied to generate the optimum tool path and develop new gap controlling strategy for five-axis near-dry EDM milling, which will be discussed in the following chapters.

# Chapter 3.

# Five-Axis Tool Path Planning for Near-Dry EDM Milling

## 3.1 Introduction

In the last ten years, much research has been conducted in five-axis trajectory planning for conventional CNC milling. However, the physics behind five-axis near-dry EDM milling and conventional five-axis milling are fundamentally different. The five-axis trajectory planning for conventional milling cannot be directly implemented for near-dry EDM milling. In order to develop strategies for five-axis trajectory planning for near-dry EDM milling, the fundamental difference between the conventional milling and near-dry EDM milling must be clarified. In conventional milling, once the trajectory and the feed rate are sent to the CNC, the CNC drives each axis at the specified feed rate. On the other hand, in EDM milling, the feed rate is constantly overridden by a feed rate override function. Hence, the optimal trajectory planning for five-axis conventional milling may not be appropriate for near-dry EDM milling. This chapter aims to develop a tool path generation strategy for five-axis near-dry EDM milling. The strategy to generate the tool path, including methodology to determine the method to engage the electrode into the workpiece, width of cut for machining of workpiece edge, minimum allowable lead angle ($\alpha$) for curvature machining and minimum and maximum path interval, *S*, are presented. Experimental results and analysis are discussed for validation.

## 3.2 Literature Survey

In conventional milling process, there have been many studies to optimize the machining process. Kruth and Klewais (1994) investigated the effect of tool orientation in five-axis conventional milling and reduced the total machining time, improved the geometrical accuracy, and improved surface finish.

In five-axis machining, tool path must be thoroughly checked to avoid collisions. Takeuchi and Watanabe (1992) developed a general method to create collision free five-axis milling path. This work is focused on avoiding collision, however, other important factors, such as scallop height and number of paths, are ignored. Scallops on the workpiece deteriorate the accuracy of the final product, and various efforts have been made to minimize the scallop height while trading off against the total machining time. Scallops are generated by the geometry of the effective cutting edge projected onto the workpiece and the tool path interval. Usually, the tool path is set as small as possible to minimize the scallop height. This method, however, results in long machining time.

To eliminate the redundancy in the tool path, Lee and Ji (1997) and Lee (1998b) investigated the machining strips based on the geometry of the tool and the curvature of the workpiece. Using their method, non-uniform path interval can be used while maintaining the scallop height under tolerances. Once the initial path is chosen at the edge of surface, this method determines the entire tool path to machine the designed surface within the tolerance.

The non-uniform path interval, also known as non-isoparametric path planning, reduces the machining time, but the gouging problems must be incorporated into the strategy. Lee (1997, 1998a) also investigated relationship between the geometry of the tool and the curvature of the surface to map the regions of tool orientations where the gouging problem is avoided. Lo (1999a) investigated the gouging avoidance and iso-scallop height machining, which is similar to work done by Lee. In a similar work, Lo (1999b) also proposed real time cutter contact point compensation.

In a recent work, Jun et al. (2003) developed an algorithm that automatically generates a map of gouging free inclination angles for each cutter contact point. Lai et al. (2003) developed a method to adaptively change the length of linear approximation in a single path to minimize the chord error in machining of large sculptures. Affouard et al. (2004) investigated the singularities in the inverse kinematics and avoided the region of singular region. Erkorkmaz and Altintas (2001) used trajectory defined by splines and considered the jerks from the commanded tool path to achieve high speed machining.

Although intensive research has been done for conventional five-axis machining, the physics behind the machining process of conventional milling and EDM milling are fundamentally different. Trajectory planning developed for five-axis machining can't be applied to five-axis EDM milling. For example, the jerk limiting trajectory planning does not improve the near-dry EDM milling since the feed rate is considerably low.

In the area of multi-axis EDM milling, only a few studies have been done. Ding and Jiang (2004) studied four axis tool path generations for four axis contouring EDM rough milling, but their work was only an extension of conventional milling with discharge gap compensation and electrode shortening compensation.

## 3.3 Tool Path Planning Strategy

To maximize *MRR* for near-dry EDM milling, the mist flow rate through the main discharge region (MDR), defined as the narrow gap between the electrode and wokpiece for spark generation, must be maximized (Fujiki et al.). Three unit vectors, feed direction ( $\hat{x}$ ), cross feed direction ( $\hat{y}$ ), and surface normal direction ( $\hat{z}$ ) are introduced to describe the coordinates at the electrode contact point on the workpiece surface as shown in Figure 3.1.

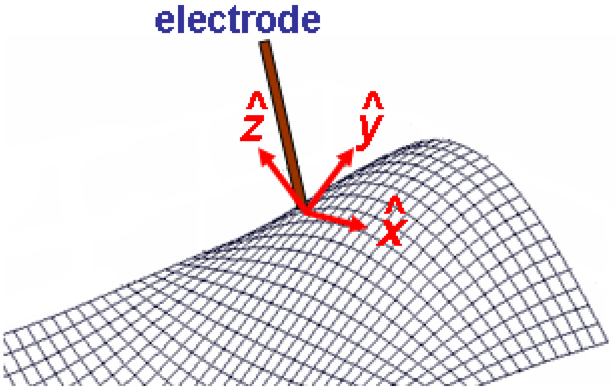

Figure 3.1. Coordinate system at the electrode contact point on the workpiece surface.

### 3.3.1 Methods to Engage Electrode into the Workpiece

Figure 3.2 shows various methods to engage the workpiece and electrode. In conventional end milling, the tool tip position is located below the workpiece surface and engages from the side, as illustrated in Figures 3.2(a) and (b). However, to maximize the mist flow rate through MDR, this approach is not suitable. A majority of mist escapes from the bottom end of electrode. Plunging, as shown in Figures 3.2(c) and (d), is a more suitable method to engage for near-dry EDM milling. However, when $\alpha \neq 0°$ (Figure 3.2(d)), mist can escape from the space between the electrode hole and unmachined work surface. To maximize *MRR*, plunging with $\alpha = 0°$ (Figure 3.2(c)), gradually changing $\alpha$ after the full engagement of electrode, and then starting to move the electrode across the surface is the more suitable method to tool path planning in near-dry EDM milling.

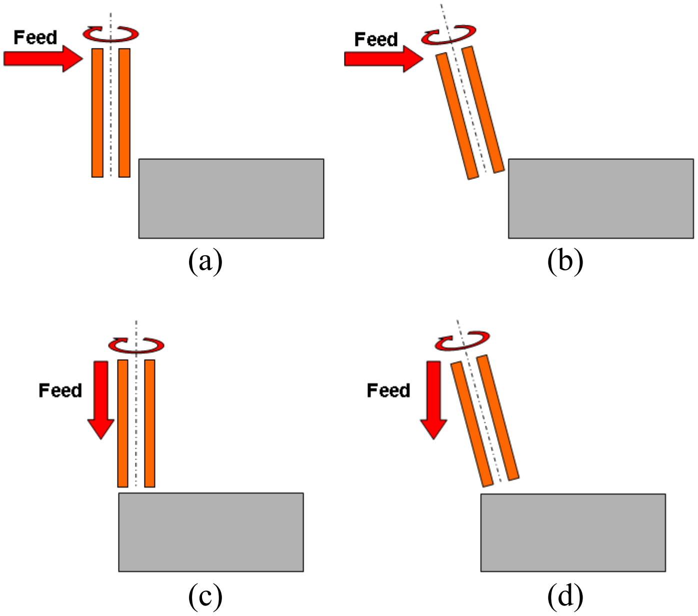

Figure 3.2. Cross-sectional view of methods to engage tool and workpiece: (a) conventional with $\alpha = 0$, (b) conventional with $\alpha \neq 0$, (c) plunge with $\alpha = 0$, and (d) plunge with $\alpha \neq 0$.

### 3.3.2 Width of Cut for Machining of a Workpiece Edge

When a workpiece edge is machined using the near-dry EDM milling, the mist can escape from the open space between the electrode hole and workpiece, as shown in Figure 3.3(a). Figure 3.3 shows the top view of workpiece and electrode when the edge of the workpiece is being machined. To ensure the mist flow through MDR, following condition for the width of cut, *w*, as shown in Eq. (3-1), must be satisfied.

$$\frac{\phi_{OD} + \phi_{ID}}{2} \leq w \leq \phi_{OD} \tag{3-1}$$

where $\phi_{OD}$ is outer diameter of electrode and $\phi_{ID}$ is inner diameter of electrode. If $\frac{\phi_{OD} + \phi_{ID}}{2} \leq w$, a part of electrode hole becomes exposed to the open atmosphere, mist escapes from the location and *MRR* will be significantly reduced (Fujiki et al., 2009). If $w \leq \phi_{OD}$, part of workpiece surface will be left unmachined.

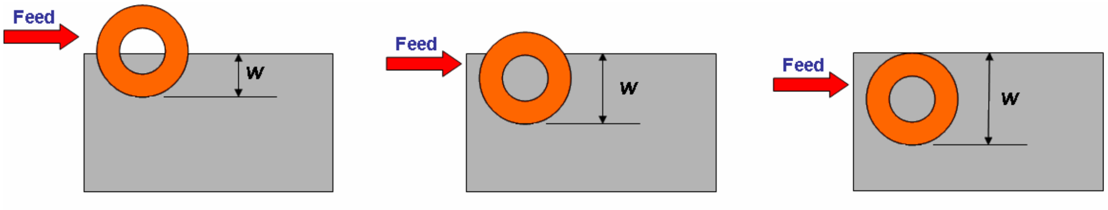

(a) (b) (c)

Figure 3.3. Top view of work and electrode during edge machining when $w =$ (a) $\frac{\phi_{OD}}{2}$, (b) $\frac{\phi_{OD} + \phi_{ID}}{2}$, and (c) $\phi_{OD}$.

### 3.3.3 Curvature Along the Feed Direction

For convex and concave surfaces, two cases exist to determine $\alpha$ for curvature along the feed direction to prevent mist leakage. Figure 3.4(a) shows the workpiece and electrode projected on the $\hat{x}\ \hat{z}$ plane for a convex surface when $\alpha \neq 0$. The bottom face of the electrode, rather than the electrode hole, must be located below the workpiece profile to avoid the mist leakage. A previous study shows only a slight *MRR* decrease from the maximum value as long as the electrode hole is not exposed to the open atmosphere (Fujiki et al.). When $\alpha$ is used in near-dry EDM milling, discharges also occur inside the electrode hole, enlarges $\phi_{ID}$ near the tip, and estimation of actual $\phi_{ID}$ at the tip becomes difficult. The worn electrodes shown in Figure 3.5 are after near-dry EDM milling. When $\alpha \neq 0$, $\phi_{ID}$ is locally enlarged near the tip while not much change is observed in the geometry of outer diameter, and when $\alpha = 0$, $\phi_{ID}$ is not affected, but $\phi_{OD}$ becomes smaller.

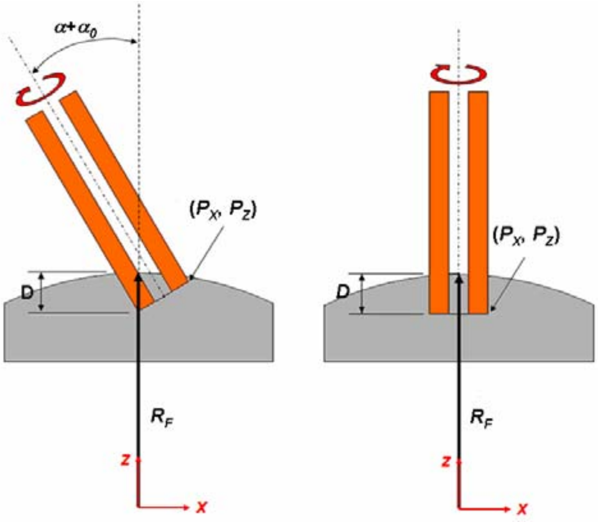

(a) (b)

Figure 3.4. Projection of electrode and workpiece on $\hat{x}\ \hat{z}$ plane for convex surface (a) minimum $\alpha$ and (b) minimum $D$ when $\alpha = 0°$.

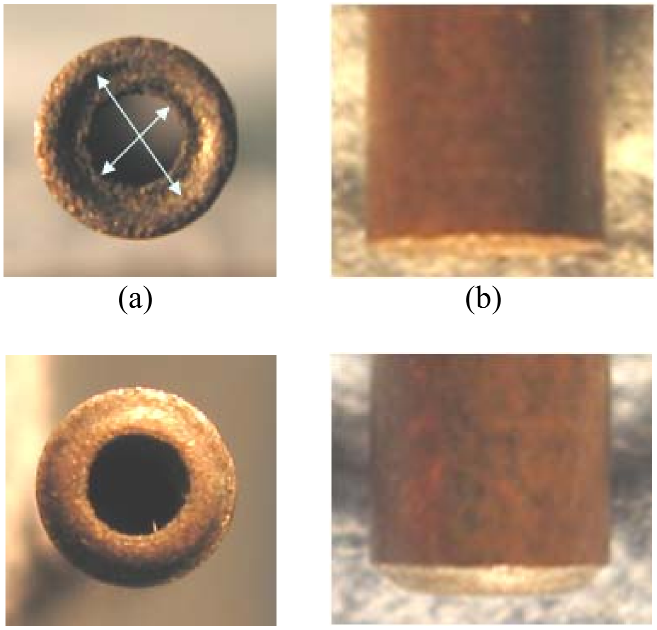

(a) (b)

(c) (d)

Figure 3.5. Picture of a tip of a worn electrode after machining (a) with $\alpha$, front view (b) with $\alpha$, side view, (c) without $\alpha$, front view, and (d) without $\alpha$, side view.

A point ($P_X$, $P_Z$) is created on the electrode's tip on the front most point in *x*-axis for the minimum $\alpha$ so that the point is located below the unmachined workpiece surface. The center of workpiece curvature is set as an origin. For convex surface, location of the point can be expressed as following:

$$P_X = \phi_{OD} \cos(\alpha + \alpha_0) \quad (3\text{-}2)$$

$$P_Z = \phi_{OD} \sin(\alpha + \alpha_0) + R_F - D \quad (3\text{-}3)$$

where $\alpha_0$ is offset angle to avoid mist leakage due to tool wear, $R_F$ is curvature of workpiece along feed direction and $D$ is the depth of cut. The detail of $\alpha_0$ is discussed in Section 3.5.1. To maintain the point below the workpiece surface, Eq. (3-4) must be satisfied.

$$P_X{}^2 + P_Z{}^2 < R_F{}^2 \tag{3-4}$$

Substituting Eqs. (3-2) and (3-3) into Eq. (3-4) yields the range of $\alpha$ for a convex surface to avoid mist leakage.

$$0 \geq \alpha \geq -\sin^{-1}\left( \frac{2R_F D - D^2 - \phi_{OD}{}^2}{2\phi_{OD}\left(R_F - D\right)} \right) + \alpha_0 \tag{3-5}$$

Minimum $D$ also exist for convex surface when $\alpha$ = 0°. Figure 3.4(b) shows projection of the workpiece and electrode on $\hat{x}\ \hat{z}$ plane for convex surface when $\alpha$ = 0°. In this configuration, the expression of the point ($P_X$, $P_Z$) is:

$$P_X = \frac{\phi_{OD}}{2} \tag{3-6}$$

$$P_Z = R_F - D \tag{3-7}$$

Substituting the above equations to Eq. (3-4) yields the expression for the minimum $D$ when $\alpha$ = 0°.

$$D \geq \frac{2R_F - \sqrt{4R_F{}^2 - \phi_{OD}{}^2}}{2} \tag{3-8}$$

If $D$ is less than the minimum value or $\alpha$ is less than the minimum value, a section of the bottom face of the electrode is exposed to the open atmosphere and mist escapes from the location.

When the surface is concave, the maximum $\alpha$ to avoid gouging and the minimum $\alpha$ to avoid a section of electrode exposing to the open atmosphere exist. Figure 3.6 shows the concave workpiece and electrode projected on the $\hat{x}\ \hat{z}$ plane. To avoid mist leakage and gouging, the point ($P_X$, $P_Z$) must be located between the unmachined and desired surface curve. Location of the point for concave surface changes as follows.

$$P_X = \phi \cos(\alpha + \alpha_0) \tag{3-9}$$

$$P_Z = -\phi \sin(\alpha + \alpha_0) + R_F + D \tag{3-10}$$

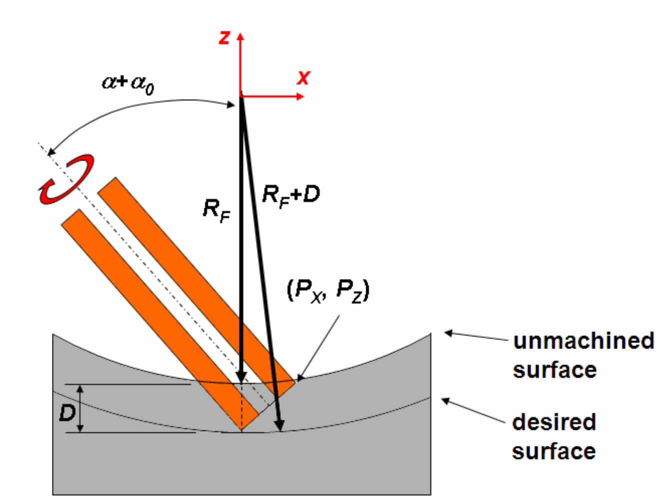

Figure 3.6. Projection of electrode and workpiece on the $\hat{x}\ \hat{z}$ plane for a concave surface.

To locate the point between two curves, the following conditions must be satisfied.

$$R_F^{\ 2} \geq P_X^{\ 2} + P_Z^{\ 2} \geq \left(R_F + D\right)^2 \tag{3-11}$$

Substituting Eqs. (3-9) and (3-10) to Eq. (3-11) yields the range of $\alpha$ to avoid mist leakage. To compute for the maximum $\alpha$, $\alpha_0$ is set zero since no safety is needed.

$$-\sin^{-1}\left(\frac{2R_F D + D^2 + \phi_{OD}^{\ 2}}{\phi_{OD}\left(R_F + D\right)}\right) + \alpha_0 \leq \alpha \leq -\sin^{-1}\left(\frac{\phi_{OD}}{2\left(R_F + D\right)}\right) \tag{3-12}$$

### 3.3.4 Curvature Along Cross Feed Direction

Figures 3.7(a) and (b) show the workpiece and electrode projected on $\hat{y}\ \hat{z}$ plane for the concave and convex surface curvatures along the cross feed direction, respectively. When the electrode is projected on the plane, the outer boundary of its tip becomes an ellipse as described in Eq. (3-13).

$$\frac{4y^2}{\phi_{OD}^{\ 2}} + \frac{4z^2}{\phi_{OD}^{\ 2}\sin^2\left(\alpha + \alpha_0\right)} = 1 \tag{3-13}$$

where $y$ and $z$ are the coordinate along the $\hat{y}$ and $\hat{z}$ direction. To maintain the entire electrode tip submerged below the unmachined workpiece surface and gouging, this ellipse must be located between the unmachined workpiece and the desired curvature. For convex surfaces, the unmachined workpiece and desired curvatures can be expressed as in Eqs. (3-14) and (3-15), respectively.

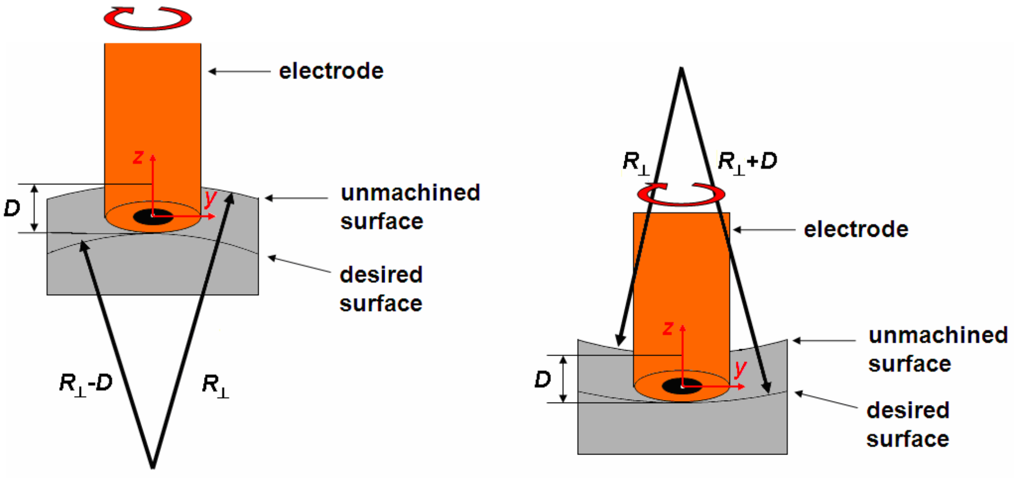

(a) (b)

Figure 3.7. Projection of electrode and workpiece on the $\hat{y}\ \hat{z}$ plane for (a) convex and (b) concave surface.

$$y^2+\left(z+R_\perp-D+\frac{\phi_{OD}\sin(\alpha+\alpha_0)}{2}\right)^2=R_\perp{}^2 \tag{3-14}$$

$$y^2+\left(z+R_\perp-D+\frac{\phi_{OD}\sin(\alpha+\alpha_0)}{2}\right)^2=(R_\perp+D)^2 \tag{3-15}$$

where $R_\perp$ is the curvature of the workpiece in the cross feed direction. For convex surface, the ellipse in Eq. (3-13) may intersect with the unmachined workpiece surface as described in Eq. (3-14) at zero, one or two point. To solve for the minimum $\alpha$ so the two curves do not intersect, Eq. (3-13) is solved for $z$, which is then substituted into Eq. (3-14) and solved for the roots of $y$ as following:

$$y^2 + \left( \begin{array}{l} \frac{1}{2}\sin(\alpha+\alpha_0)\sqrt{-4y^2+\phi_{OD}{}^2} + R_\perp \\ -D + \frac{\phi_{OD}\sin(\alpha+\alpha_0)}{2} \end{array} \right)^2 = R_\perp{}^2 \tag{3-16}$$

$$y = \pm\frac{\sqrt{2}}{-1+\sin^2\alpha} \left( \begin{array}{l} (2D\phi_{OD} - 2R_\perp\phi_{OD})\sin^3(\alpha+\alpha_0) \\ + \left( \begin{array}{l} -4R_\perp{}^2 - \phi_{OD}{}^2 \\ -2D^2 + 4R_\perp D \end{array} \right) \sin^2(\alpha+\alpha_0) \\ + (-2R_\perp D + 2D\phi_{OD})\sin(\alpha+\alpha_0) \\ + 4R_\perp D - 2D^2 \\ \pm\sin(\alpha+\alpha_0) \left( \begin{array}{l} -D + 2R_\perp \\ + \phi_{OD}\sin(\alpha+\alpha_0) \end{array} \right) \\ \left( \begin{array}{l} 4R_\perp{}^2\sin^2(\alpha+\alpha_0) \\ + 4\phi_{OD}(R_\perp - D)\sin(\alpha+\alpha_0) \\ + \phi_{OD}{}^2 + 4D^2 - 8R_\perp D \end{array} \right)^{\frac{1}{2}} \end{array} \right)^{\frac{1}{2}} \tag{3-17}$$

Since two curvatures must not intersect to avoid mist leakage, the expressions inside square roots in Eq. (3-17) must be imaginary. The range of $\alpha$ can be solved:

$$-\sin^{-1}\left( \frac{ \begin{array}{l} -R_\perp\phi_{OD} + D\phi_{OD} + \\ \sqrt{ \begin{array}{l} -2R_\perp\phi_{OD}{}^2 D + D^2\phi_{OD}{}^2 \\ -4R_\perp{}^2 D^2 + 8R_\perp{}^3 D \end{array} } \end{array} }{2R_\perp{}^2} \right) + \alpha_0 \le \alpha \le 0 \tag{3-18}$$

$$\text{for } \frac{2R_F - \sqrt{4R_F{}^2 - \phi_{OD}{}^2}}{2} < D < \frac{\phi_{OD}{}^2}{2R_\perp}$$

and

$$-\sin^{-1}\left(\frac{D}{\phi_{OD}}\right)+\alpha_0 \le \alpha \le 0 \text{ for } D \ge \frac{\phi_{OD}{}^2}{2R_\perp} \tag{3-19}$$

For concave surface, the projected electrode in Eq. (3-13) must be placed between the unmachined workpiece and desired curvatures as in Eqs. (3-20) and (3-21), respectively.

$$y^2+\left(z-R_\perp-D+\frac{\phi_{OD}\sin(\alpha+\alpha_0)}{2}\right)^2=R_\perp{}^2 \tag{3-20}$$

$$y^2+\left(z-R_\perp-D+\frac{\phi_{OD}\sin\alpha}{2}(\alpha+\alpha_0)\right)^2=(R_\perp+D)^2 \tag{3-21}$$

For any *D*, the ellipse only intersects with the unmachined workpiece curve at one point. The range of $\alpha$ to prevent mist leakage is:

$$\alpha \ge -\sin^{-1}\left(\frac{D}{\phi_{OD}}\right)+\alpha_0 \tag{3-22}$$

The maximum $\alpha$ exists to avoid gouging. Gouging occurs when the ellipse intersects with the desired surface curve. Solving Eq. (3-13) for *z*, setting $\alpha_0$ to zero and substituting the negative solution into Eq. (3-21) yields and solving for the roots of *y* yields:

$$y^2+\begin{pmatrix}-\frac{1}{2}\sin(\alpha)\sqrt{-4y^2+\phi_{OD}{}^2} \\ -R_\perp - D + \frac{1}{2}\phi_{OD}\sin\alpha\end{pmatrix}^2 = (R_\perp + D)^2 \tag{3-23}$$

Therefore,

$$y = 0, \pm \frac{\sqrt{\begin{aligned}&\sin^3\alpha(2R_\perp\phi_{OD}+D\phi_{OD})\\&+\sin^2\alpha(-8R_\perp D-4D^2-\phi_{OD}{}^2-4R_\perp{}^2)\\&+\sin\alpha(R_\perp\phi_{OD}+2D\phi_{OD})\end{aligned}}}{(\sin\alpha+1)(\sin\alpha-1)} \tag{3-24}$$

Solving Eq. (3-23) for $\alpha$, so the expression inside the square roots becomes negative, yields following maximum value for $\alpha$ to avoid gouging.

$$\alpha \le -\sin^{-1}\left(\frac{\phi_{OD}}{2(R_\perp + D)}\right) \tag{3-25}$$

Combining Eqs. (3-22) and (3-25) yields the range of $\alpha$ for machining curvature along the cross feed direction to prevent gouging and mist leaking.

$$-\sin^{-1}\left(\frac{\phi_{OD}}{2(R_\perp + D)}\right) \le \alpha \le -\sin^{-1}\left(\frac{D}{\phi_{OD}}\right) + \alpha_0 \tag{3-26}$$

### 3.3.5 Path Interval

In conventional milling, $S$ is usually chosen based on desired scallop height (Lee, 1998b). However, for near-dry EDM milling, the minimum $S$ also exists so that the electrode hole in the new path is not exposed to the cavity created by the previous path. Figure 3.8 shows the projection of workpiece and electrodes from new and old path on the $\hat{y}\ \hat{z}$ plane for convex and concave surfaces. The $\hat{y}\ \hat{z}$ projection is from the old path and $\hat{y}'\ \hat{z}'$ projection is from the new path.

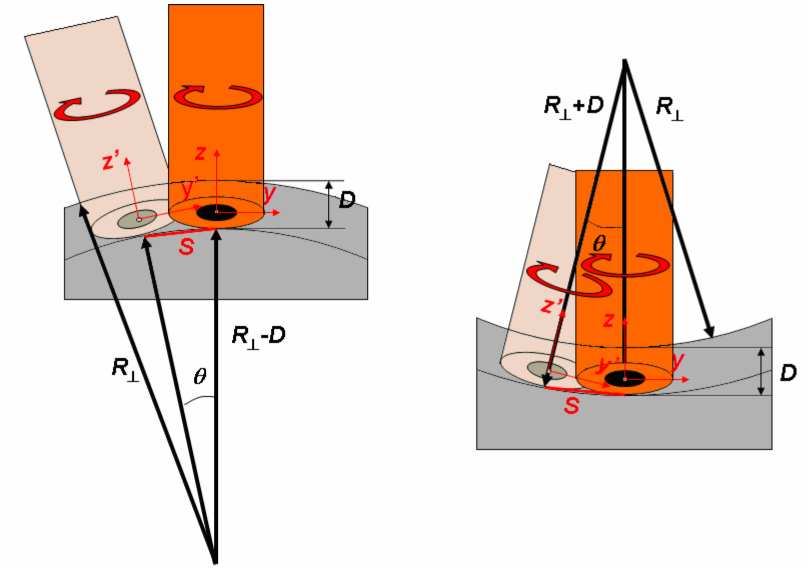

(a) (b)

Figure 3.8. Projection of electrode from current path, old path, and workpiece on the $\hat{y}\ \hat{z}$ plane for (a) convex and (b) concave surface.

To compute the minimum $S$ for convex curvature, body fixed coordinate systems are first created on the centers of ellipses from the old ($y'$, $z'$) and new ($y$, $z$) path. The coordinate transformation can be expressed as:

$$\theta = 2\sin^{-1}\left(\frac{S}{2R_\perp}\right) \tag{3-27}$$

$$y' = y\cos\theta + z\sin\theta + \left(R_\perp + \frac{\phi_{OD}\sin\alpha}{2}\right)\sin\theta \tag{3-28}$$

$$z' = -y\sin\theta + z\cos\theta - \left(R_\perp + \frac{\phi_{OD}\sin\alpha}{2}\right)(1-\cos\theta) \tag{3-29}$$

The minimum $S$ is numerically computed so that two ellipses as described in Eqs. (3-30) and (3-31) do not intersect.

$$\frac{4y^2}{\phi_{ID}^{\ 2}} + \frac{4z^2}{\phi_{ID}^{\ 2}\sin^2\alpha} = 1 \tag{3-30}$$

$$\frac{4y'^2}{\phi_{OD}^{\ 2}} + \frac{4z'^2}{\phi_{OD}^{\ 2}\sin^2\alpha} = 1 \tag{3-31}$$

For concave curvature, the coordinate transformation, as described in Eqs. (3-28) and (3-29), changes to the following.

$$y' = y\cos\theta - z\sin\theta + \left(R_\perp - \frac{\phi_{OD}\sin\alpha}{2}\right)\sin\theta \tag{3-32}$$

$$z' = y\sin\theta + z\cos\theta + \left(R_\perp - \frac{\phi_{OD}\sin\alpha}{2}\right)(1-\cos\theta) \tag{3-33}$$

## 3.4 Experimental Setup

A die-sinking EDM machine (Model AQ55L by Sodick, Schaumburg, IL), as shown in Figure 3.9, is modified by adding a rotary table (Model HA5CB by Haas Automation, Inc., Oxnard, CA), an EDM spindle (Rotobore by Everest Inc., Huntington Beach, CA), and a mist delivery system (Model 6000 precision applicator by AMCOL, Hazel Park, MI) to realize the 4.5-axis near-dry EDM milling. A C-axis made by Sodick is attached to the Z-axis column and a rotary table, model HA5CB made by HAAS, is mounted on the worktable. The C-axis is synchronized with the EDM gap controller. The A-axis which controls the tilt of the workpiece is controlled by an external controller and only moves in stepping rotation. The path generation strategy described in Section 3.3 is tested individually. A reference ball is used to measure the distance between the tool electrode tip to the center of C-axis rotation.

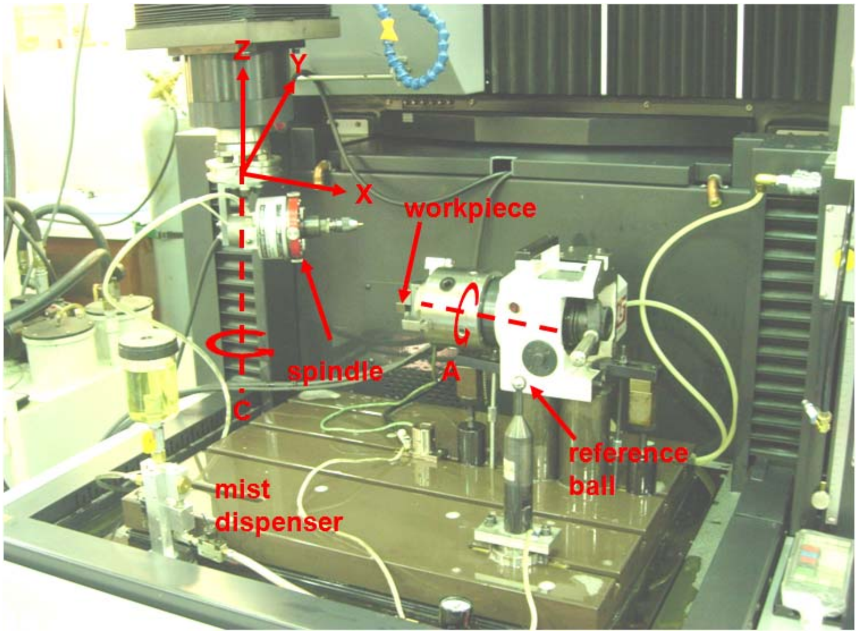

Figure 3.9. Experimental set up for 4.5-axis near-dry EDM milling.

UGS NX 5.0 is used to generate the tool path and Postbuilder 5.0.3 is used to create a post processor for the tool path generated by NX 5.0. The post processor converts the toolpath generated in NX 5.0 to series of commands (G-codes) that can be read by Sodick controller.

Table 3.1 lists the discharge parameters for near-dry EDM milling. The work material is H13 tool steel and the electrode is a copper tube. Electrode outer diameter, $\phi_{OD}$, is 3.2mm and electrode inner diameter, $\phi_{ID}$, is 1.6 mm. Depth of cut, *D*, is set at 0.5 mm for all experiments. Electrode rotational speed is set to 500 rpm. Compressed air at 517 kPa and kerosene liquid at 5 ml/min flow rate is supplied to the inlet.

Table 3.1. Discharge parameters for near-dry EDM milling experiment.

| Polarity | Negative |
|---|---|
| Open circuit voltage $u_i$ (V) | 200 |
| Pulse duration $t_i$ (μs) | 4 |
| Pulse interval $t_o$ (μs) | 8 |
| Discharge current $i_e$ (A) | 20 |
| Gap voltage $u_e$ (V) | 60 |

The weight of the workpiece before and after the machining is measured using an Ohaus GA110 digital scale with 0.1 mg resolution to calculate *MRR*. Based on the weight measurements, and *MRR* is calculated as follow:

$$MRR = \frac{\Delta m_{workpiece} / \rho_{workpiece}}{t} \tag{3-34}$$

where $\rho_{workpiece}$ and $\Delta m_{workpiece}$ are the density and mass change of workpiece, respectively,

$t$ is the time to machine. In this study, $\rho_{workpiece}$ is 7800 kg/m$^3$. In this study, the tool electrode wear ratio and surface roughness are not evaluated since tool path generation strategy discussed in this study is for roughing. In semi-finishing and finishing process, which uses low discharge energy, the depth of cut is less than 50 μm, which makes the minimum $\alpha$ close to zero.

Six sets of experiment were conducted to study:

Experiment I: Offset angle
Experiment II: Methods to engage electrode into the workpiece
Experiment III: Width of cut for machining of a workpiece edge
Experiment IV: Curvature along the feed direction
Experiment V: Curvature in the cross feed direction
Experiment VI: Path interval.

Tool wear is not compensated during the experiment. Each experiment is repeated three times and average and standard deviation of *MRR* are calculated.

## 3.5 Experimental Procedures and Results

Experimental measurements of *MRR* in experiments I to VI are presented and compared in the following six sections.

### 3.5.1 Experiment I: Offset Angle

Tool wear shortens the electrode and, as shown in Figure 3.10(a), moves the point ($P_X$, $P_Z$) to outside the workpiece surface and decreases the *MRR*. The offset angle, $\alpha_0$, is applied to adjust the lead angle of electrode so that the point remains below the workpiece surface even with the tool wear, as shown in Figure 3.10(b).

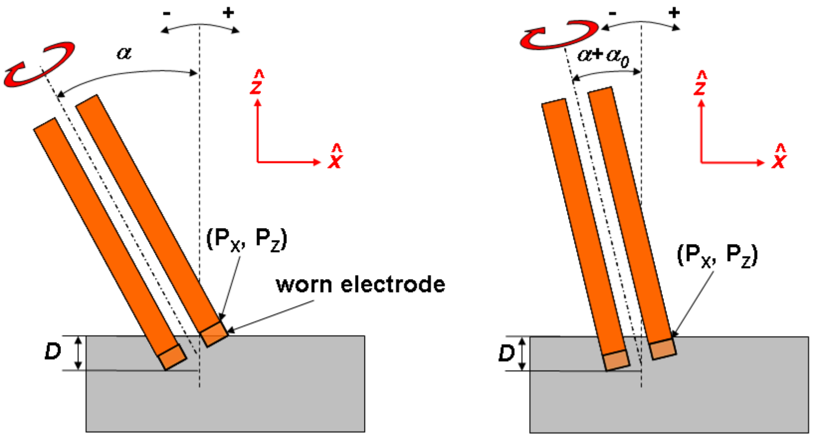

(a) (b)

Figure 3.10. Projection of electrode and workpiece on the $\hat{x}$ $\hat{z}$ plane for a flat surface (a) without $\alpha_0$ and (b) with $\alpha_0$.

Slots were machined on a flat surface to find $\alpha_0$ for this particular study with 20 mm slot length and 0.5 mm depth of cut (*D*). This offset angle is applied to other slot near-dry EDM tests of the same length and depth of cut in the study with curvature in the feed and cross-feed directions.

Based on Eq. (3-5), the range of $\alpha$ for a flat surface ($R_F \rightarrow \infty$) can be computed as following.

$$0 \geq \alpha \geq -\sin^{-1}\left(\frac{D}{\phi_{OD}}\right) + \alpha_0 \qquad (3\text{-}35)$$

Solving Eq. (3-35) using the setup parameters listed in Section 3.4, the range of $\alpha$ is between 0° to $-9.0° + \alpha_0$. Tests were conducted to find the $\alpha_0$ that maximizes the *MRR*. Tests in the range of $\alpha$ between –4° to –8° in one degree increment and at 0° at the benchmark were conducted. As shown in the results of experiment in Figure 3.11, the highest *MRR* occurs at $\alpha = -5°$, which corresponds to $\alpha_0 = 4°$. This $\alpha_0$ is applied to all following experiments (experiments II to VI).

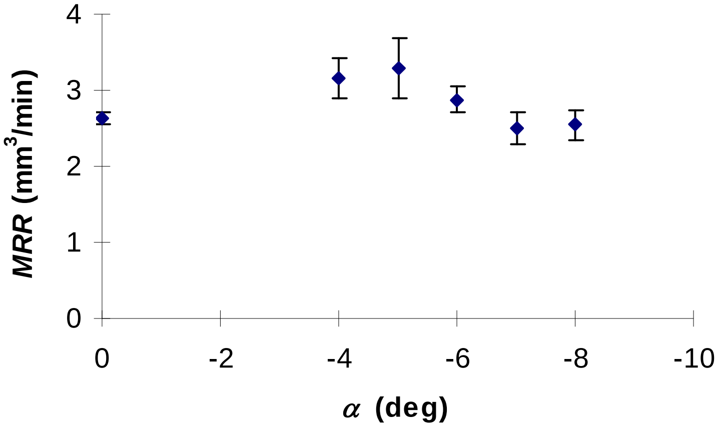

Figure 3.11. Experiment I results – *MRR* at different offset angles.

### 3.5.2 Experiment II: Methods to Engage Electrode into Workpiece

The methods to engage the electrode, as discussed in Section 3.3.1, are experimentally investigated. Four configurations illustrated in Figure 3.2 are examined.

Figure 3.12 shows the *MRR* from the electrode engaging experiments. The plunge method (the configuration in Figure 3.2(c)) had the highest *MRR* followed by plunge method with $\alpha$, conventional method, and conventional method with $\alpha$. The conventional engaging methods regardless of $\alpha$ value have considerably low *MRR* because of the mist leakage while engaging the workpiece. Compared with plunge method, 26% decrease in *MRR* was observed for conventional method and 62% decrease was observed for conventional method with $\alpha \neq 0$, while plunge method with $\alpha \neq 0$ has only 6% decrease.

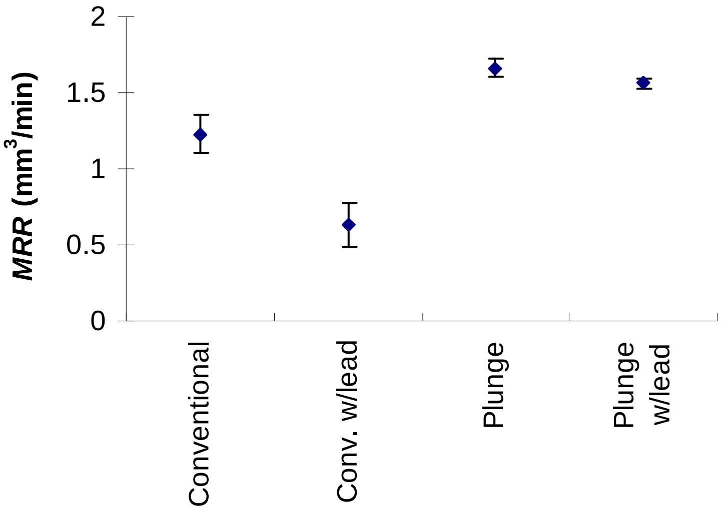

Figure 3.12. Experiment II results – *MRR* using four engagement methods ($\alpha = -5°$).

### 3.5.3 Experiment III: Width of Cut for Machining of a Workpiece Edge

The minimum *w* to machine the edge of workpiece, from Section 3.3.2, is verified. Theoretically, the electrode hole must not be exposed to open atmosphere as shown in Figures 3.3(b) and (c) to avoid the drop in *MRR*. Using the setup parameters discussed in the Section 3.4 and Eq. (3-1), the minimum distance from the edge (*w*) is 2.4 mm for the electrode used in this study. In this experiment, $w$ = 1.6 mm (50% of $\phi_{OD}$, which causes the mist leakage), 2.4 mm (minimum distance), and 3.2 mm (maximum distance) are examined.

Figure 3.13 shows experimental results from workpiece edge machining. The *MRR* was high and not significantly different for $w$ = 2.4 and 3.2 mm. However, when $w$ = 1.6 mm, the electrode hole is exposed to the open atmosphere and a 31% decrease in *MRR* is observed.

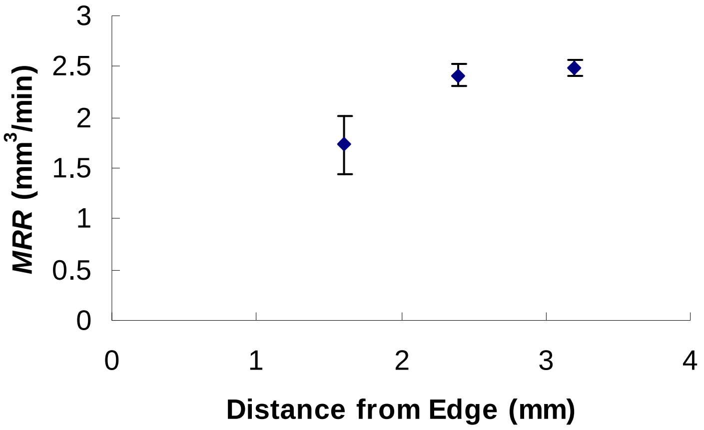

Figure 3.13. Experiment III results – *MRR* for edge machining.

Combining the results from the engaging methods experiment, tool path for near-dry EDM milling must place the electrode hole inside the workpiece boundary. If the electrode hole travels outside the workpiece boundary, mist leaks and the decrease in *MRR* is expected during the re-engaging and edge machining.

### 3.5.4 Experiment IV: Curvature Along the Feed Direction

The maximum and minimum $\alpha$ for the curvature along the feed direction to prevent mist leakage, as discussed in Section 3.3.3, are experimentally investigated. For the experiment, workpiece with convex and concave $R_F$ = 25 mm, as seen in Figures 3.14(a) and (b), is prepared. The electrode is plunged into the workpiece until *D* reaches 0.5 mm and a 20 mm slot along the curvature is machined.

For convex surface, solving Eq. (3-5) using parameters listed in Section 3.4 yields $0° \geq \alpha \geq -5.2° + \alpha_0$, which is the range of $\alpha$ that prevents mist leakage. Three tests were conducted with $\alpha$ at 0° (the maximum $\alpha$), –1.2° (the minimum $\alpha$ with $\alpha_0 = 4°$), and –6.2° (1° larger than the minimum $\alpha$ without $\alpha_0$). Only three tests are conducted at $\alpha$ that are the minimum and maximum of $\alpha$ with $\alpha_0$ (limits obtained in the theoretical analysis) and a test condition outside this range. The purpose of this experiment is to validate the proposed analytical model, not to find the angle with the maximum *MRR*.

At $\alpha$ = –6.2°, the mist will leak from the electrode hole from the start of slot machining. Figure 3.15(a) shows experimental *MRR* results. The highest *MRR* occurs at $\alpha$ = –1.2° and, compared to that at $\alpha$ = 0°, 17% improvement is observed due to the improvement of mist flow rate through the MDR (Fujiki, 2009), where the most of machining action occurs in near-dry EDM milling. Mist leakage is not the only criterion that determines the *MRR*. Although the mist leaks from the electrode hole at $\alpha$ = –6.2°, *MRR* is higher than that at $\alpha$ = 0°, which has no mist leakage. This happens because when $\alpha$ = 0°, part of the mist does not flow through the MDR.

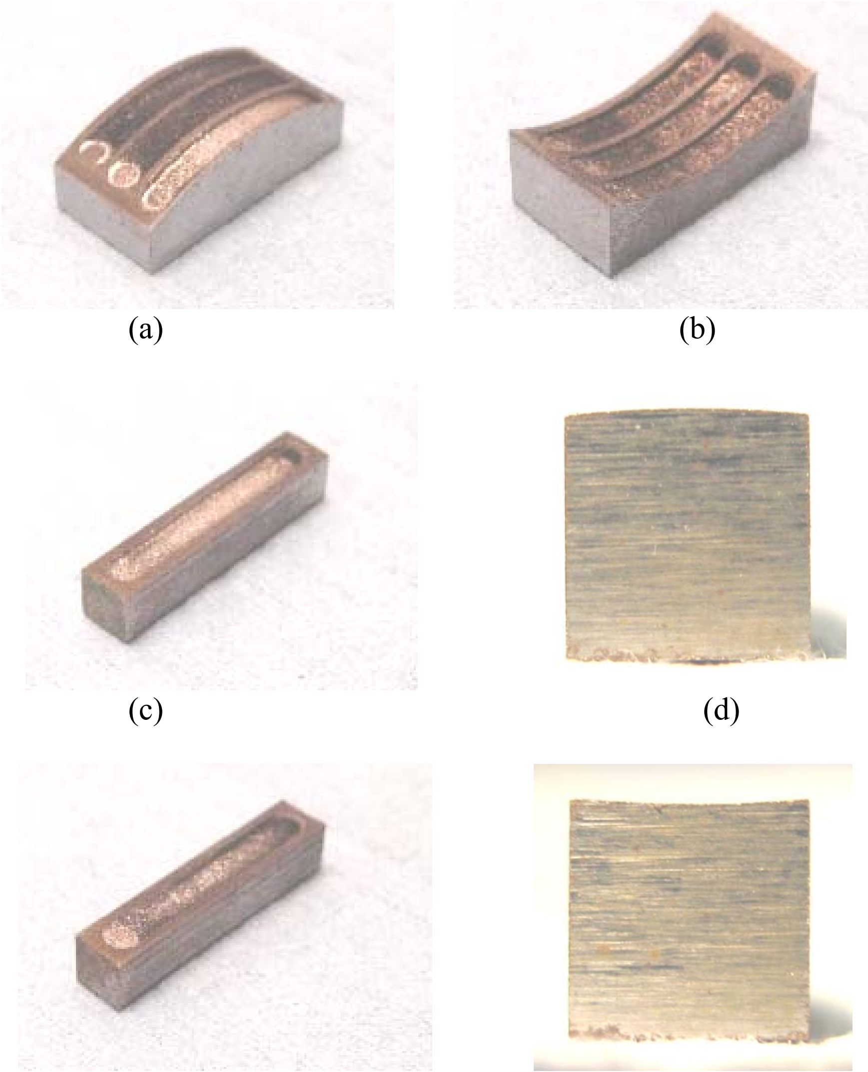

(a) (b)

(c) (d)

(e) (f)

Figure 3.14. Workpiece with 25 mm curvature for machining experiments (a) convex curvature along feed direction, (b) concave curvature along feed direction, (c) convex curvature along cross-feed direction, (d) side view of convex curvature along cross-feed direction, (e) concave curvature along cross-feed direction, and (f) side view of concave curvature along cross-feed direction.

For concave surface, solving Eq. (3-12) using parameters listed in Section 3.4 yields $-3.6^\circ \geq \alpha \geq -12.5^\circ + \alpha_0$, which is the range of $\alpha$ that prevents the mist leakage. Three tests were conducted with $\alpha$ at –3.6° (the maximum $\alpha$), –8.5° (the minimum $\alpha$

with $\alpha_0$ = 4°), and –13.5° (1° larger than the minimum $\alpha$ without $\alpha_0$). Like for the convex surface, three tests are selected at the range of $\alpha$ that avoids gouging and mist leakage, not to find the optimal $\alpha$ for *MRR*. At $\alpha$ = –13.5°, the mist leaks from the electrode hole from the start of slot machining. As shown in the experimental *MRR* results in Figure 3.15(b), the *MRR* is maximized at $\alpha$ = –8.5° and, compared to *MRR* at $\alpha$ = –3.6°, 34% improvement is observed due to the improvement of mist flow through MDR. Similar to the results from convex surface, *MRR* for $\alpha$ = –13.5°, which causes mist leakage, has slightly higher *MRR* than the one from $\alpha$ = –3.6°, which has no mist leakage but limited mist flow rate through the MDR.

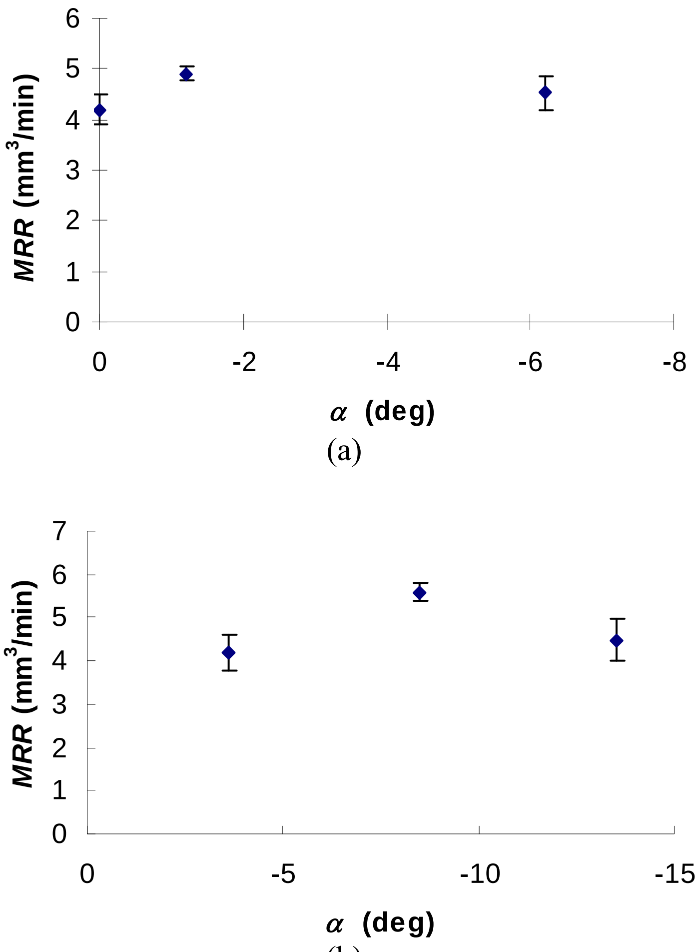

(a)

(b)

Figure 3.15. Experiment IV results - *MRR* from $R_F = 25$ mm for the (a) convex and (b) concave surfaces.

Experiment IV results conclude that the minimum $\alpha$ with offset angle $\alpha_0$ is the lead angle selection for high *MRR* in near-dry EDM machining with curvature in the feed direction.

### 3.5.5 Experiment V: Curvature Along the Cross Feed Direction

The maximum and minimum $\alpha$ for the curvature along the cross feed direction, as discussed in Section 3.3.4, are experimentally investigated. For the experiment, workpiece with convex and concave $R_\perp$ = 25 mm, as shown in Figures 3.14(c) and (e), respectively, is prepared. Similarly to experiment IV, the electrode is plunged into the workpiece until $D$ reaches 0.5 mm and a 20 mm slot is machined.

For convex surface, the equation to solve the range of $\alpha$ that avoids mist leakage depends on $D$. Because $0.5 = D \geq \frac{{\phi_{OD}}^2}{2R_\perp} = 0.2$, Eq. (3-18) is solved using parameters listed in Section 3.4 to find the range of $\alpha$, $0° \geq \alpha \geq -9.0° + \alpha_0$, without the mist leakage. Similar to experiment IV, three tests were conducted with $\alpha$ = 0° (the maximum $\alpha$), –5° (the minimum $\alpha$ with $\alpha_0$ = 4°), and –10° (1° larger than the minimum $\alpha$ without $\alpha_0$) to validate the feasible range of $\alpha$. Figure 3.16(a) shows the experimental results. The *MRR* is maximized when $\alpha$ = –5° and, compared with the *MRR* at $\alpha$ = 0°, 31% improvement is observed. The leakage of mist at $\alpha = -10°$ has an adverse effect on the *MRR*.

For concave surface, solving Eq. (3-26) using parameters listed in Section 3.4 yields $-3.7° \geq \alpha \geq -9.0° + \alpha_0$, which is the range of $\alpha$ that does not cause the mist leakage. Three tests were conducted with $\alpha$ at –3.7° (the maximum $\alpha$), –5° (the minimum $\alpha$ with $\alpha_0$ = 4°), and –10° (1° larger than the minimum $\alpha$ without $\alpha_0$). The experimental results in Figure 3.16(b) shows the highest *MRR* at $\alpha$ = –5°. It is a 3% improvement of *MRR* compared with that of $\alpha = -3.7°$. The *MRR* improvement was low for the concave case due to the small difference between the minimum and maximum $\alpha$. The leakage of mist at $\alpha = -10°$ also has a significant effect on the reduction of *MRR*.

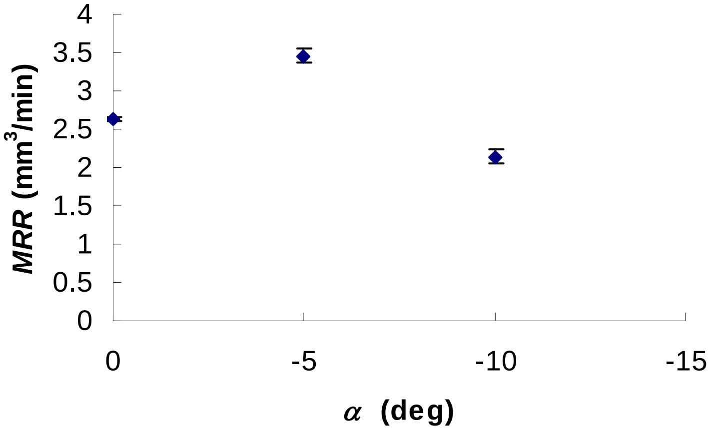

(a)

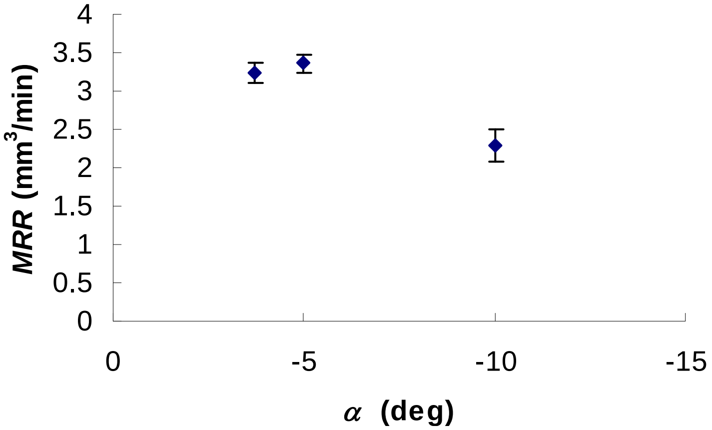

(b)

Figure 3.16. Experiment V results – *MRR* from $R_{\perp}$ = 25 mm for the (a) convex and (b) concave surfaces.

The same conclusion as in experiment V, the minimum $\alpha$ with offset angle $\alpha_0$ is the lead angle to improve the *MRR* for machining workpiece with either convex or concave curvature cross the feed direction.

### 3.5.6 Experiment VI: Path Interval

The minimum and maximum path interval, as discussed in Section 3.4.5, is experimentally verified for near-dry EDM milling. A flat surface ($R_{\perp} \rightarrow \infty$), instead of concave or convex surfaces, is machined. Based on Eq. (3-36), the range of $S$ for a flat surface are:

$$\frac{2\phi_{OD} - \phi_{ID}}{2} \leq S \leq \phi_{OD} \qquad (3\text{-}36)$$

Solving Eq. (3-36) using parameters discussed in Section 3.4 yields $2.4\,\text{mm} \leq S \leq 3.2\,\text{mm}$, which is the range of $S$ that prevents the mist leakage.

Three tests were conducted at $S$ = 1.6 mm (50% of $\phi_{OD}$, with mist leakage), 2.4 mm (minimum $S$), and 3.2 mm (the maximum $S$). For all three tests, $\alpha = -5°$ is used. Figure 3.17 shows results from path interval experiment. The maximum $S$ (3.2 mm) has the highest *MRR*. 14% and 16% drop in *MRR* was observed at the minimum $S$ (2.4 mm) and S that causes mist leakage (1.6 mm). At minimum $S$, a small change in the *MRR* was expected, similar to the machining of edge experiment, which is discussed in Section 3.5.3 and Figure 3.13 ($w$ = 2.4 and 3.2 mm). The drop in *MRR* at minimum $S$ is caused by electrode wear. When $\alpha$ is used in near-dry EDM milling, discharges also occur within the electrode hole and locally enlarge $\phi_{ID}$, as shown in Figure 3.5(a). The mist escapes from the enlarged hole and lowers *MRR*. Hence, the enlarged $\phi_{ID}$ must be used to compute the minimum $S$.

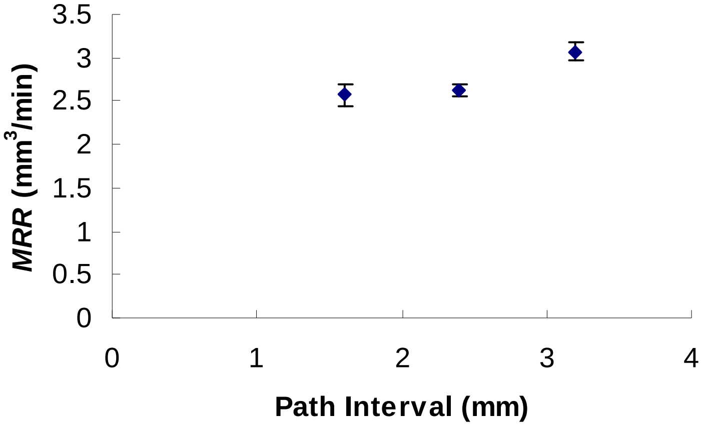

Figure 3.17. Experiment VI results – *MRR* of three path interval tests ($\alpha = -5°$).

Experiment VI shows that the maximum *S* should be used to maximize *MRR*, but it can be lowered to the minimum *S* to reduce the scallop height.

## 3.6 Concluding Remarks

Electrode tool path planning strategy, including the engaging method, edge machining, curvature machining, and path interval to improve the *MRR* for five-axis near-dry EDM milling was presented. Each strategy was experimentally validated on the *MRR*. To maximize *MRR*, mist flow rate through MDR is the first priority to plan a path for five-axis near-dry EDM milling, rather than minimization tool path length, which is prioritized in conventional milling. The electrode tip must remain below the workpiece surface when lead angle is used and the electrode hole must not be exposed to the open atmosphere. This maximizes mist flow rate through MDR and results in maximum *MRR*.

Current study is limited to approximating the curvature with a locally cylindrical surface. In the future work, 3D expression of surface using non-uniform rational B-spline (NURBS) or tetrahedral should be used for machining of sculpture surface.

# Chapter 4.

# Gap Control of Five-Axis Near-Dry EDM Milling

## 4.1 Introduction

The control of EDM process is different from conventional CNC machining (Snoeys et al., 1982). As shown in Figure 4.1, an extra control loop besides the servo control, called gap control loop, is used in EDM control. The average voltage during discharge, called gap voltage, $u_e$, is constantly monitored and the feed rate is overridden based on the difference between the reference gap, $u_{eref}$, and monitored $u_e$, as shown in Figure 4.2. Therefore, the feed rate constantly changes in EDM.

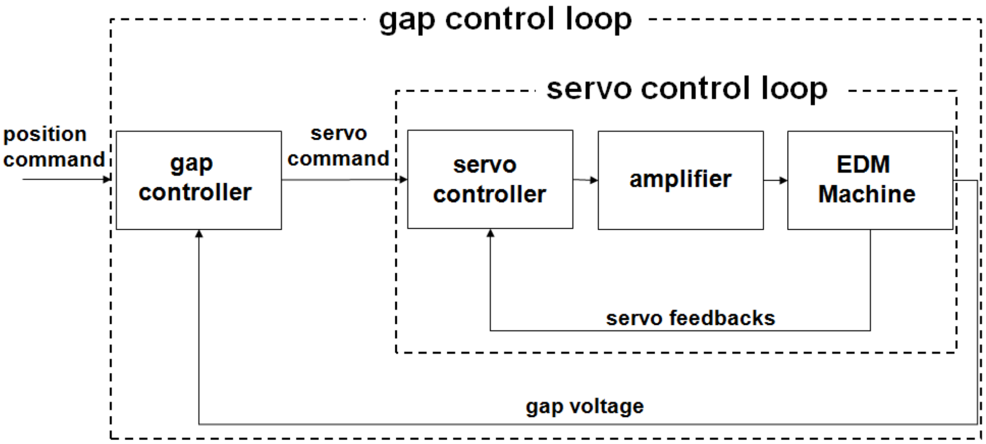

Figure 4.1. Typical control loop in EDM.

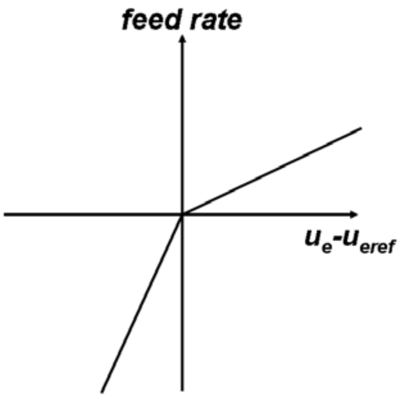

Figure 4.2. Feed rate override function in EDM.

Much work has been done in the control of EDM, but investigation lacks of control strategies best suited to improve the mist flow and MRR in five-axis near-dry EDM milling. The mist flow rate through the main discharge region (MDR) changes depending on the electrode orientation (Fujiki et al., 2009). The study also shows that negative lead angle helps to improve MRR and tilt angle has negative effect on MRR due to the changes in the mist flow rate through MDR. Hence, the proposed gap control strategy is based on the concept of further improvement of the dielectric medium flow in the discharge gap when negative lead angle is used. By improving the flow, the discharge gap condition can be enhanced by increasing the debris flushing, and the feed rate override function does not need to retract the electrode as often. As a result, overall MRR increases. This research develops a new control strategy specialized for near-dry EDM milling with lead angle using a piezoelectric actuator for gap condition control. This technology can be applied for five-axis near-dry EDM milling. The MDR under five-axis configuration is unique and requires a different gap control approach compared with conventional EDM process.

In this chapter, the gap control strategy for retracting the tubular electrode in

EDM milling is first presented. Experimental setup to investigate the control strategy is followed. Detailed structure of a spindle system that retracts the electrode at high bandwidth is also discussed. Finally, experimental results on machining performance (MRR, tool electrode wear ratio, and surface roughness) using the proposed strategies are discussed, analyzed and compared with the traditional gap control method.

## 4.2 Literature Survey

To improve the number of effective discharges, Kruth et al. (1979) developed an adaptive control system that searches the optimum reference gap voltage. Snoeys et al. (1980) improved the adaptive control by Kruth et al. by incorporating the discharge interval as another variable to be optimized. The adaptive control by Kruth et al. and Snoeys et al. is based on the maximization of effective discharge count and their concept is widely used by the EDM machine manufacturers.

Much work has been done to determine the output value of the manual feed rate override (MFO) function. Chang (2002) developed a variable structure system (VSS) control to control the gap distance with the robustness. Zhang et al. (2002) developed an adaptive fuzzy controller for the gap distance control. Kao et al. (2008a and 2008b) also developed fuzzy controller using piezo stage for micro EDM hole drilling. Nowadays, research in gap control based on fuzzy control is becoming more popular since it utilizes the know-how of skilled operators (Ho and Newman, 2003). The drawback of fuzzy controller, however, is that it only controls the feed rate. To maximize the MRR for five-axis near-dry EDM milling, controlling methods beyond feed rate override is required since conventional feed rate override does not efficiently enlarge discharge gap for five-axis near-dry EDM milling due to relative orientation of electrode and workpiece surface.

Research in development of local actuator to enhance the flow of dielectric medium in the discharge gap has proven to improve the MRR in EDM processes. Ultrasonic vibration can enhance the dielectric fluid flow in the discharge gap (Murthy ahd Philip, 1987). The ultrasonic vibration did not change the key discharge profiles, such as ignition time delay and average discharge energy, but decreased the number of short circuit and arcing. As a result, ultrasonic vibration improved the overall efficiency of machining process by 27%. Other studies showed that ultrasonic vibration increases MRR (Kremer et al., 1989 and 1991, Enache et al., 1990, Zhang et al., 1997, Gao and Liu, 2003). However, it also increased the tool electrode wear ratio and surface roughness. Ultrasonic vibration has proven to increase MRR in dry EDM (Zhang et al., 2002, 2006a and 2006b). One problem with ultrasonic vibration is that it does not optimize the mist flow rate through the discharge region, which is critical in near-dry EDM milling (Fujiki et al., 2009).

High bandwidth electrode positioning has also been investigated to enhance the MRR. A piezo actuator attached on an electrode can improve the MRR in EDM micro hole drilling (Imai et al., 1996). Further extension of the study has been made using electro-magnets (Imai et al., 2004). A system that can position a small electrode in a three-dimensional space with high bandwidth has also been developed (Beltrani et al., 2004). In dry EDM milling, a piezo actuator is attached beneath the workpiece and improvements in MRR and tool electrode wear ratio were observed (Kunieda et al., 2004).

## 4.3 Proposed Gap Control Strategy

In conventional EDM, machine is controlled by retracting electrode along a commanded trajectory based on the gap voltage regardless of type of EDM process. Figures 4.3(a), (b), and (c) illustrate the feed and retract direction for sinking EDM, wire EDM, and three-axis EDM milling, respectively. This gap control strategy is adequate for these EDM configurations since the direction of retraction is always orthogonal to the MDR. The electrode retraction direction being orthogonal to the main discharge plane maximizes the efficiency of gap enlargement, which results in better debris flushing. For five-axis EDM milling, retracting the electrode along the trajectory is not efficient because the MDR is typically not orthogonal to the retract direction. Figure 4.4 shows two MDR regions, denoted as MDR 1 and MDR 2, in EDM milling with lead angle. MDR 1 is located at the bottom tip of electrode and MDR 2 is located at the inner trailing face of electrode. To efficiently enlarge the gap distance, the electrode should retract in the direction of the electrode orientation, in the direction of Retraction 1 as shown in Figure 4.4, using a piezo actuator rather than in the direction of Retraction 2. In this study, a novel method to control the gap by moving the electrode in both direction of Feed/Retraction 1 and 2 as shown in Figure 4.4 in near-dry EDM will be investigated.

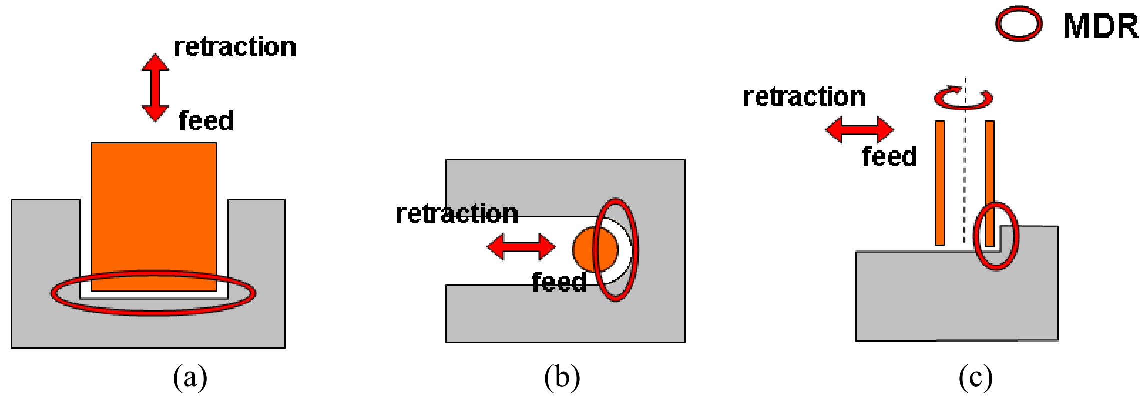

Figure 4.3. Gap control in conventional EDM control for three types of EDM configurations: (a) die-sinking, (b) wire EDM, and (c) three-axis EDM milling.

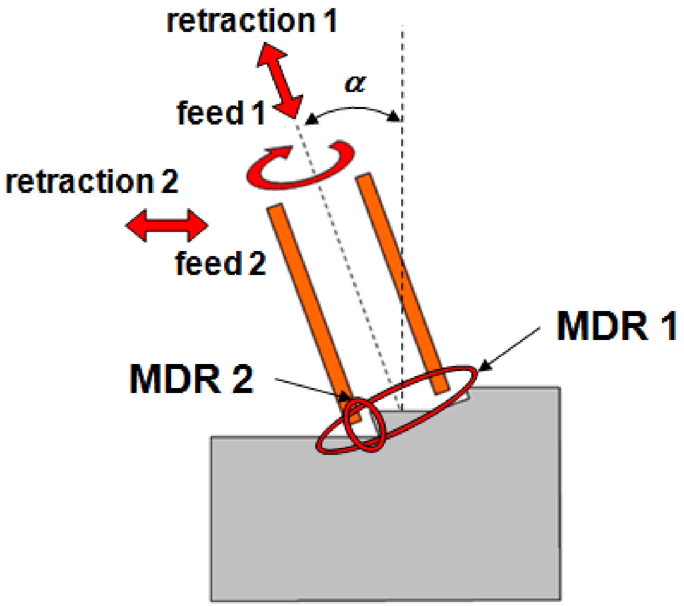

Figure 4.4. The ideal gap control for five-axis near-dry EDM milling.

A control structure that separates the electrode retraction and electrode feed along the path is the key to the proposed control strategy. The feed rate override function in Figure 4.2 cannot be implemented directly to the near-dry EDM milling with lead angle

(Figure 4.4) since the feed direction and the electrode retraction direction do not align. Figure 4.5 shows the block diagram of the proposed control algorithm. The movement of electrode is separated into two parts, one is the motion along the planned trajectory (XYZ axes) and the other is the auxiliary axis motion, which is defined as the movement of the electrode along the direction of electrode orientation. Two controllers exist in the proposed architecture. The proposed controller controls the position of auxiliary axis driven by a piezo actuator based on the difference between the reference gap voltage, $u_{eref}$, and the average gap voltage feedback, $u_e$. The proposed controller also regulates the motion of X, Y, and Z-axes by outputting modified average gap voltage, $u_{eout}$ to the EDM controller. The EDM controller changes the feed rate based on the difference between $u_{eout}$ and $u_{eref}$. The motion of X, Y, Z, and auxiliary axis changes the gap distance to maintain stable discharges.

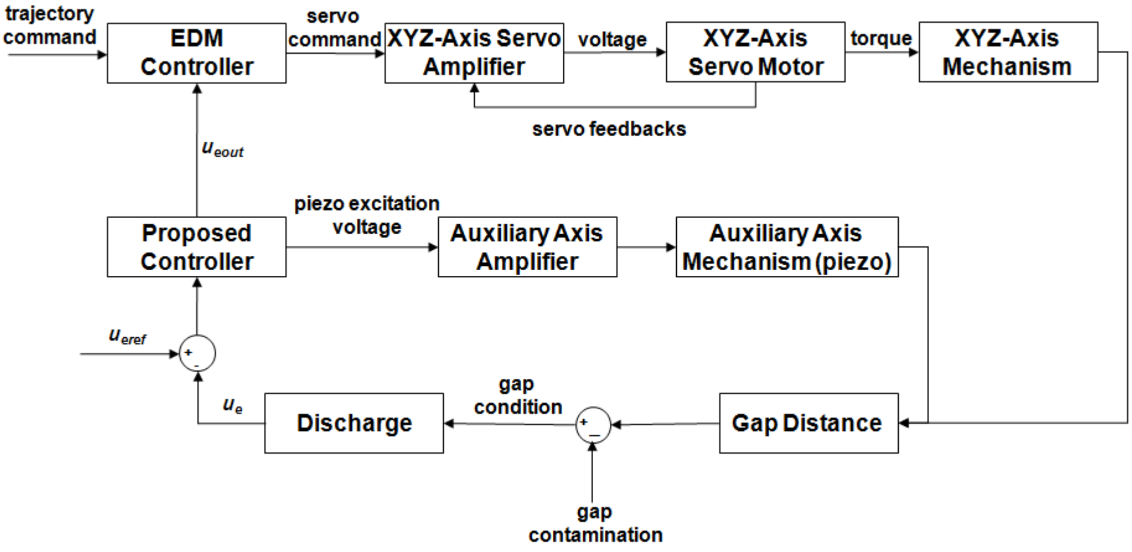

Figure 4.5. Block diagram of proposed controller.

Figure 4.6 show the flowchart of the proposed control algorithm. Two control modes exist in the proposed controller. The first is trajectory mode in which the electrode moves forward along the planned trajectory. The second is the auxiliary axis mode in which electrode moves in its orientation direction. The controller switches back and forth between these two modes based on a status of a parameter, $M$. When the mode $M$ is 0, the controller runs in trajectory mode, and when $M$ switches to 1 controller runs in auxiliary axis mode in the next sampling time, and vice versa.

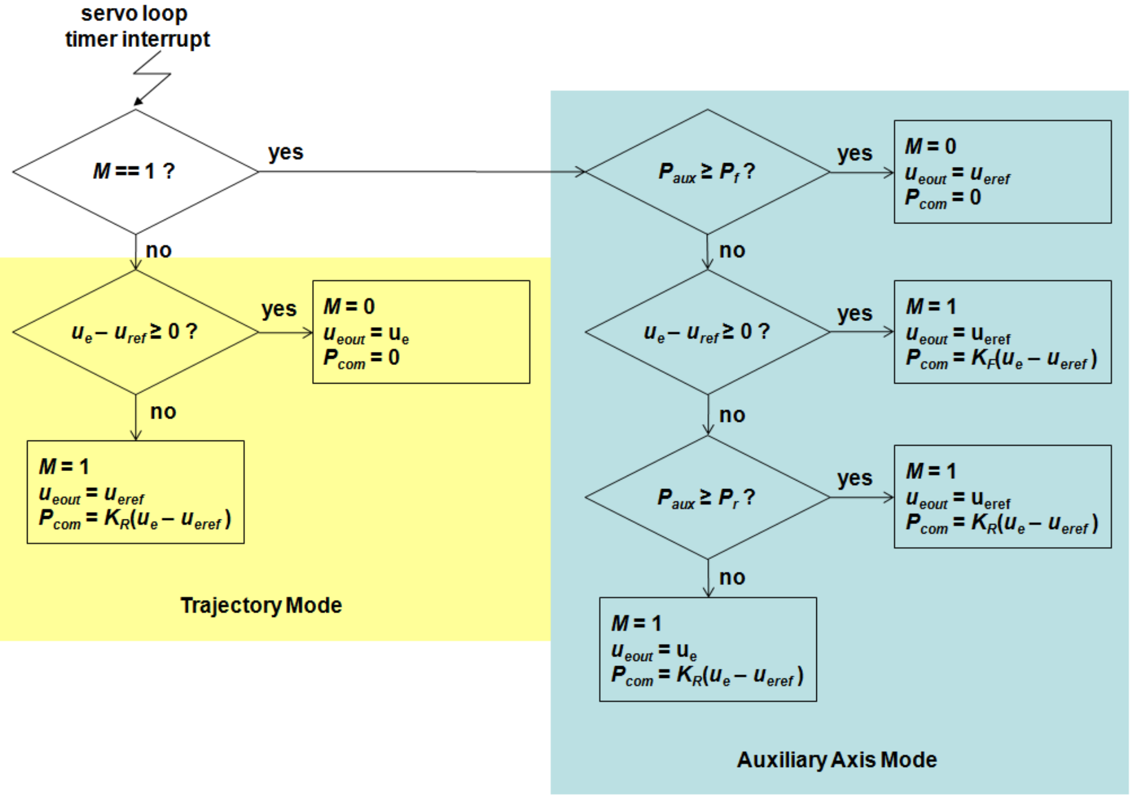

Figure 4.6. Flowchart of proposed controller.

The proposed controller has one input and two outputs. The input is gap voltage from the machine ($u_e$), and the outputs are, gap voltage output to the EDM machine's controller ($u_{eout}$), and incremental position command to the auxiliary axis ($P_{com}$). At the beginning of the servo loop, the controller checks $M$ to decide which control mode it will run. Detailed algorithm of each control mode is discussed in the following section.

### 4.3.1 Trajectory Mode (*M*= 0)

The controller first checks the difference between reference gap voltage, $u_{eref}$, and gap voltage from the machine, $u_e$. If the voltage differential is positive, the controller maintains $M$ at 0, outputs $u_e$ to EDM machine's main controller, and sets $P_{com}$ to 0. The output runs the controller in trajectory mode in the next sampling time, and moves electrode along the trajectory while maintaining the auxiliary axis to the current position.

When the voltage difference is negative, the controller changes $M$ to 1, outputs $u_{eref}$ to the EDM machine's main controller, and sets $P_{com}$ as following:

$$P_{com} = K_R\left(u_{eref} - u_e\right) \tag{4-1}$$

where $K_R$ is the constant gain in proportional control for retracting. The output runs the controller in the auxiliary axis mode in the next sampling time and retracts the electrode only along the auxiliary axis. The electrode does not move along the planned trajectory since the EDM machine's main controller receives gap voltage signal which makes the machine's feed rate to zero after feed rate override ($u_e = u_{eref}$).

### 4.3.2 Auxiliary Axis Mode (*M* = 1)

The controller first checks $P_{aux}$, which is the position of auxiliary axis, to determine whether it has reached the position before electrode retraction started. If $P_{aux} \geq$

$P_F$ (the position of auxiliary axis to switch to trajectory mode), controller changes $M$ to 0, outputs $u_{eref}$ to the EDM machine's main controller, and sets $P_{com}$ to 0. The output runs the controller in trajectory mode in the next sampling time while maintaining the current electrode position along trajectory and auxiliary axis. If the position of auxiliary axis was not checked before switching to trajectory mode, the machined surface would become wavy because it causes constant change in the depth of cut in the range of auxiliary axis motion.

If $P_{aux} < P_F$, the controller checks the difference between $u_{eref}$ and $u_e$. If the voltage differential is positive, the controller maintains $M$ at 1, outputs $u_{eref}$ to the EDM machine's main controller, and sets $P_{com}$ as following

$$P_{com} = K_F \left( u_{eref} - u_e \right) \tag{4-2}$$

where $K_F$ is the constant gain in proportional control for forwarding. The output runs the controller in auxiliary axis mode in the next sampling time and moves the electrode forward along the auxiliary axis while maintaining the electrode position along the trajectory.

If the voltage differential is negative, it checks the position of electrode along auxiliary axis. If $P_{aux} \geq P_R$ (the position of auxiliary axis to start retracing the electrode along the path), the controller maintains $M$ at 1, outputs $u_{eref}$ to the EDM machine's main controller, and sets $P_{com}$ as in Eq. (1). The output runs the controller in auxiliary axis mode in the next sampling time and moves the electrode backward along the auxiliary axis while maintaining the electrode position along the trajectory.

If $P_{aux} < P_R$, the controller maintains $M$ at 1, outputs $u_e$ to the EDM machine's main controller sets $P_{com}$ as in Eq. (1). The outputs run the controller in auxiliary axis mode in the next sampling time, retracts the electrode along the auxiliary axis and trajectory. The reason that the electrode also retracts along the trajectory is the MDR also exists at the inner trailing face of electrode as shown in Figure 4.4

## 4.4 Spindle with High Bandwidth Electrode Retraction

A spindle system that can retract in high bandwidth is designed and fabricated to realize retraction along the electrode orientation direction. Its design and performance is discussed in the following sections.

### 4.4.1 Design of Spindle System

Figures 4.7(a) and (b) show the perspective and cross-sectional view of the spindle system, respectively. Figure 4.8 shows fabricated spindle system installed on EDM machine. A piezo actuator (Model P-845.30 by Physik Instrumente GmbH, Karlsruhe, Germany) is used to retract the electrode with high bandwidth. To maximize the bandwidth, the load carried by the piezo actuator is minimized. Thrust bearings unit (Model 51101 by SKF, Göteborg, Sweden) and linear spline (Model LTR10AUUCL+50L-PK by THK, Tokyo, Japan) are used to transmit axial motion from the piezo actuator while allowing rotation. A DC motor (Model 82 830 009 by Crouzet, Coppell, Texas) connected by pulleys drives the linear spline to transmit rotational motion. The detailed design of the system is discussed in Appendix.

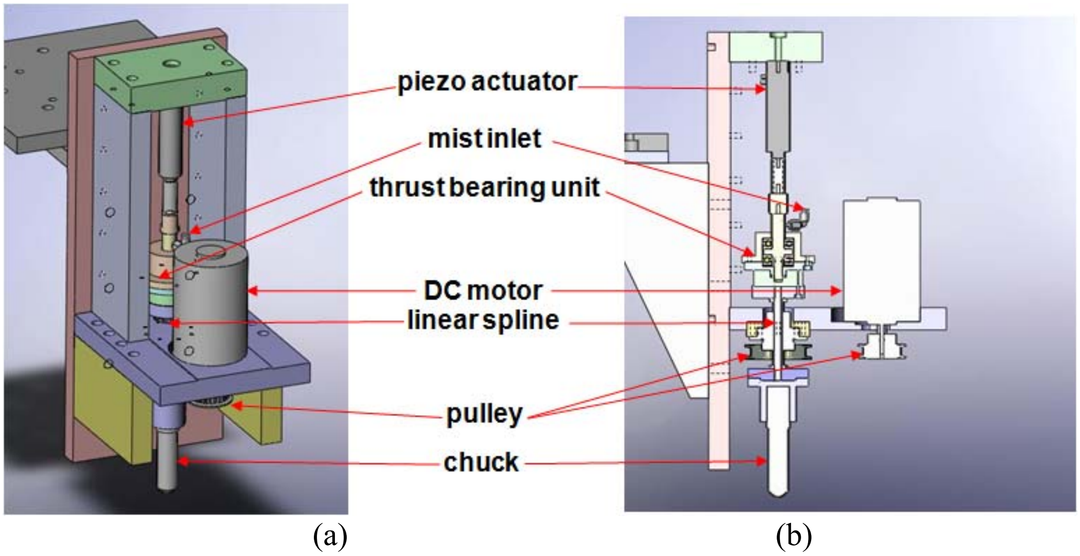

Figure 4.7. Spindle system (a) 3D solid model and (b) cross section view.

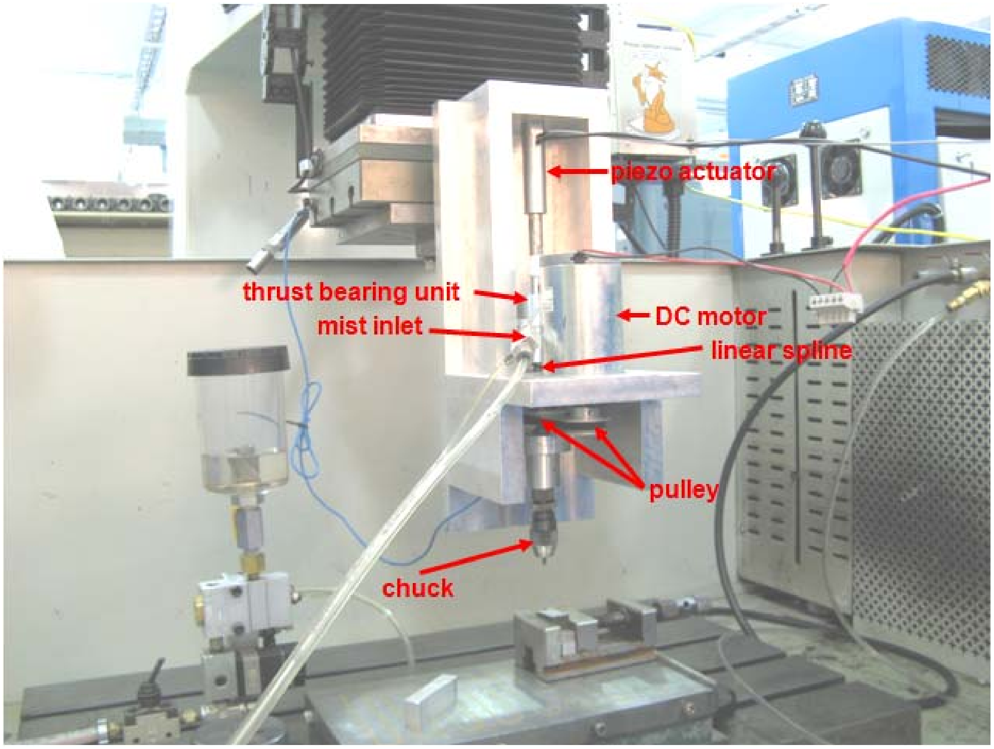

Figure 4.8. Fabricated spindle and installed on EDM machine.

### 4.4.2 Performance of Spindle System

The rigidity of the spindle frame is important. The design of spindle frame in this study is analyzed using the finite element analysis module in Solidworks. A load of 700 N, which is piezo actuator's maximum pulling force, is applied to the location where the piezo actuator is mounted. The part of structure connected to the L-shaped bracket is set as non-moving constraint. Figure 4.9 shows the simulated deformation of the spindle structure. As seen in the figure, the simulated deformation with piezo actuator's maximum pulling force is 2.3 μm.

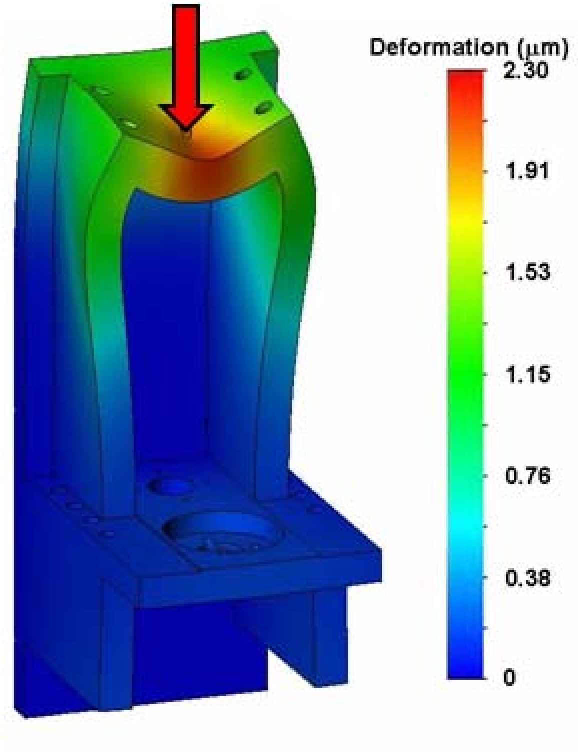

Figure 4.9. Simulated deformation of spindle structure.

The spindle tip displacement is measured using a laser interferometer (Model ML10 by Renishaw, Gloucestershire, United Kingdom). Figure 4.10 plots the voltage command given to the piezo actuator and the displacement of spindle tip. Total displacement of 46 μm, small enough for this application, is observed.

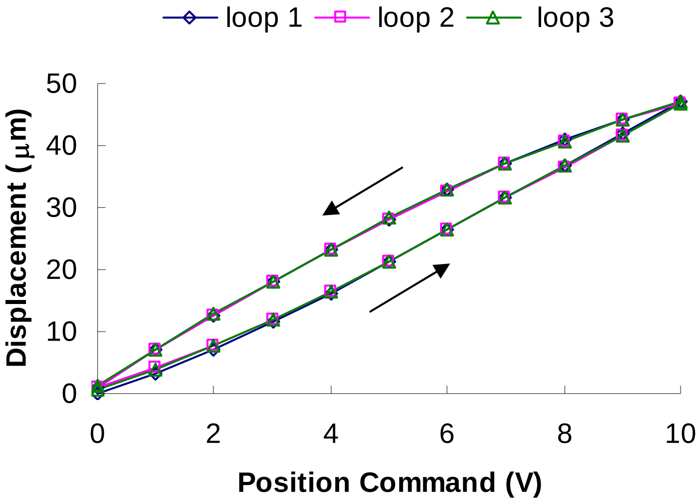

Figure 4.10. Calibration of piezo actuator.

The hysteresis effect, which is common in piezo actuator, in the range of 8 μm is observed in Figure 4.10. The piezo actuator is controlled in open loop for its simplicity. Although the position hysteresis cannot be fixed in open loop, only the incremental motion along the auxiliary axis is important in the proposed gap controller. This hysteresis effect does not significantly affect the control system performance. A first order low pass (with 500 Hz cutoff frequency) and a second order infinite impulse response (IIR) notch filter at 563 Hz with quality factor = 3 are applied to the voltage output to the piezo actuator to suppress the structural vibration. Strain gage sensor (SGS) mounted within the piezo actuator is used to read the position response, and an accelerometer is attached near the tip of spindle to measure the axial vibration.

To evaluate the performance of the piezo actuator system, a step response is performed. Figures 4.11(a) and (b) show the step response of piezo actuator's displacement and acceleration at the tip of spindle, respectively. The system has less than 2 ms step response with small axial vibration.

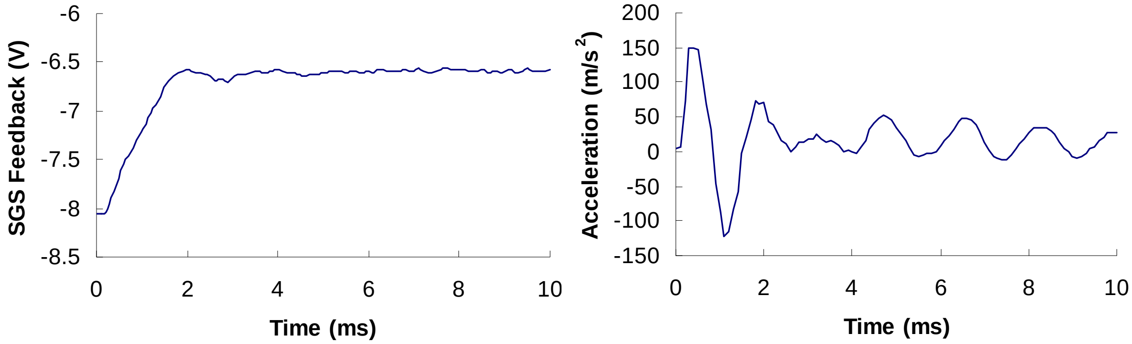

(a) (b)

Figure 4.11. Step response of the system (a) piezo actuator's displacement and (b) acceleration at the tip of spindle.

## 4.5 Experimental Setup

A die-sinking EDM machine (Model EDMS 150H by EDM Solutions, Elk Grove Village, IL) is used as a base machine. An external controller board (Model ds1104 by dSPACE, Paderborn, Germany) is used to execute the proposed controller discussed in Section 4.3. The spindle unit, external controller, and EDM machine's main controller (Model TNC 409 by Heidenhain, Traunreut, Germany) are wired as shown in the block diagram in Figure 4.12. Unlike a conventional EDM controller, as shown in Figure4.13, the gap voltage is serially passed through the external controller to realize the proposed controller. Other key output from the external controller is analog position command. The position command is amplified by the piezo amplifier module (Model E-501 and E-505 by Physik Instrumente, Karlsruhe, Germany) to excite the piezo actuator.

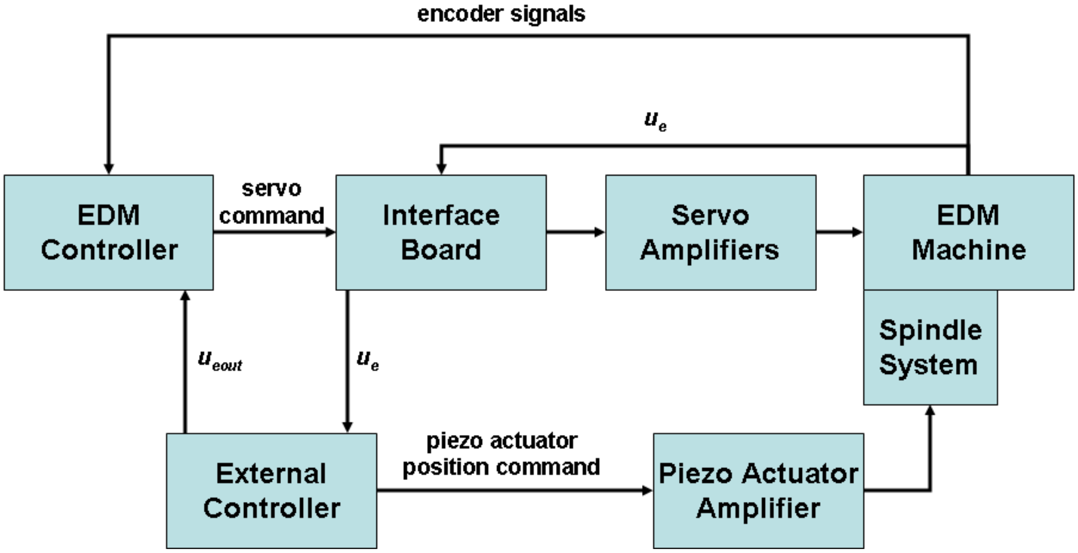

Figure 4.12. System wiring diagram.

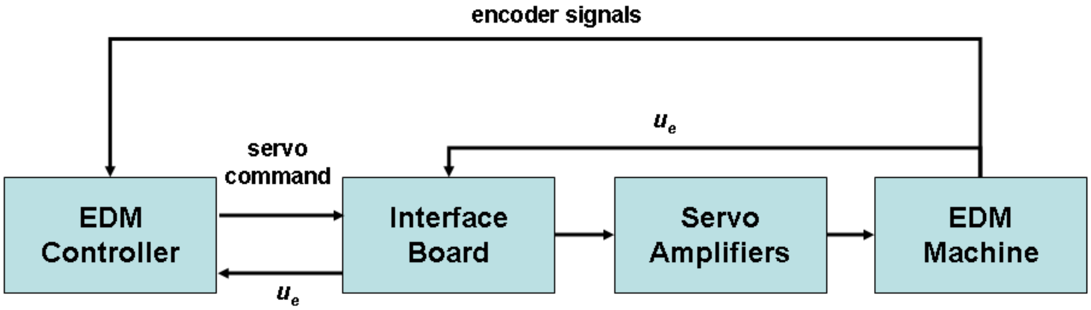

Figure 4.13. System wiring diagram for a conventional EDM machine.

Table 4.1 lists the discharge parameters for near-dry EDM milling with –5° lead angle, which is the electrode orientation with optimal MRR in the current near-dry EDM milling setup (Fujiki, 2009). The lead angle is negative since the electrode is oriented away from the feed direction. Table 4.2 lists the controller parameters used in the proposed controller. The work-material is H13 tool steel and the electrode is a copper tube. Electrode outer diameter is 3.2 mm and electrode inner diameter $\phi_{ID}$ is 1.6 mm.

Slots with 20 mm length and 0.5 mm depth of cut are machined. Electrode rotational speed is set to 500 rpm. Compressed air at 517 kPa and kerosene liquid at 5 ml/min flow rate is supplied to the inlet.

Table 4.1. Discharge parameters for near-dry EDM milling experiment.

| Polarity | Negative |
|---|---|
| Open circuit voltage $u_i$ (V) | 200 |
| Pulse duration $t_i$ (μs) | 4 |
| Pulse interval $t_o$ (μs) | 8 |
| Discharge current $i_e$ (A) | 20 |
| Gap voltage $u_e$ (V) | 60 |

Table 4.2. Control parameters for near-dry EDM milling experiment.

| | |
|---|---|
| Reference voltage $u_{eref}$(V) | 3 |
| Forwarding constant $K_F$ | 0.1 |
| Retracting constant $K_R$ | 0.5 |
| Position to switch to trajectory mode $P_F$ | 8 |
| Position to start retracting along trajectory $P_R$ | 7 |
| Sampling time (ms) | 0.1 |
| Low pass filter cutoff frequency (Hz) | 500 |
| Notch filter frequency (Hz) | 563 |

The weight of the workpiece and electrode before and after the machining are measured using an Ohaus GA110 digital scale with 0.1 mg resolution to calculate the tool electrode wear ratio ($\eta$) and *MRR*. Based on the weight measurements, $\eta$ and *MRR* are calculated as follows:

$$\eta = \frac{\Delta m_{electrode} / \rho_{electrode}}{\Delta m_{workpiece} / \rho_{workpiece}} \tag{4-3}$$

$$MRR = \frac{\Delta m_{workpiece} / \rho_{workpiece}}{t} \tag{4-4}$$

where $\rho_{electrode}$ and $\Delta m_{electrode}$ are the density and mass change of electrode, respectively, $\rho_{workpiece}$ and $\Delta m_{workpiece}$ are the density and mass change of workpiece, respectively, $t$ is the machining time. In this study, $\rho_{workpiece}$ is 7800 kg/m$^3$ and $\rho_{electrode}$ is 8933 kg/m$^3$. A Taylor Hobson profilometer with 2 μm diamond stylus tip radius is used to measure the surface roughness along the slot. The arithmetical average roughness ($R_a$) is selected as the surface roughness parameter. The experiments were repeated three times, and the average $R_a$ value is used to represent the surface roughness of the machined slot.

## 4.6 Experimental Results

The performance of the proposed controller in terms of $MRR$, $\eta$, and $R_a$ is compared with that of the conventional controller. Figures 4.14(a), (b), and (c) show the experimental comparison of the proposed controller and conventional controller in $MRR$, $\eta$, and $R_a$, respectively. Bars represent the average value, and error bars represent the maximum and minimum value from the experiment. As seen in the figure, a 30 % increase in $MRR$ and small differences in $\eta$ and $R_a$ are observed. To interpret the results of the experiment, analysis of variance (ANOVA) is carried out for $MRR$, $\eta$, and $R_a$. The results are summarized in Tables 4.3, 4.4, and 4.5. A 5% significance level was used as the criteria to determine whether the proposed controller has statistically significant effect. Therefore, results with P-value smaller than 0.05 are statistically significant. The P-value for $MRR$, $\eta$, and $R_a$ are 0.014, 0.439, and 0.551, respectively. Hence the controller improved the *MRR* by 30% without having statistically significant effect on $\eta$ and $R_a$.

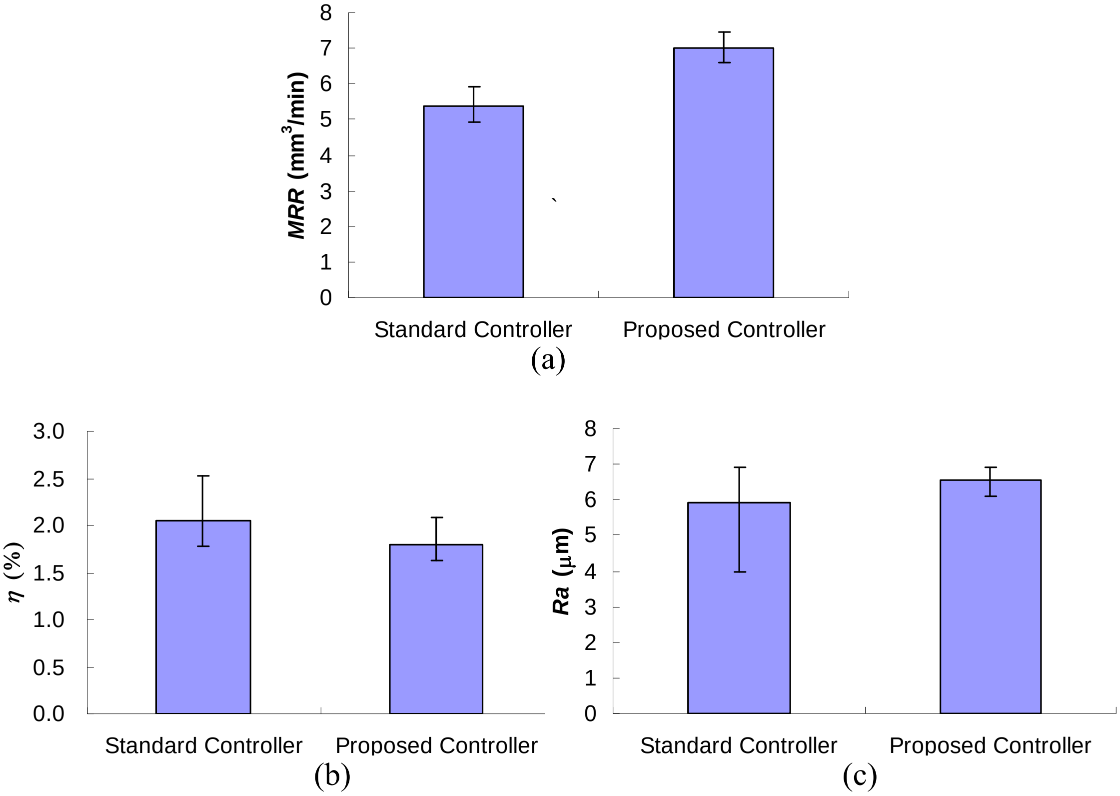

(a)

(b)

(c)

Figure 4.14. Comparison of proposed controller and conventional controller (a) *MRR*, (b) $\eta$, and (c) $R_a$.

Table 4.3. ANOVA result from the computed *MRR*.

| Source | DF | Seq SS | Adj SS | Adj MS | F | P |
|---|---|---|---|---|---|---|
| Method | 1 | 3.8879 | 3.8879 | 3.8879 | 17.78 | 0.014 |
| Error | 4 | 0.8748 | 0.8748 | 0.2187 | | |
| Total | 5 | 4.7616 | | | | |

Table 4.4. ANOVA result from the computed $\eta$.

| Source | DF | Seq SS | Adj SS | Adj MS | F | P |
|---|---|---|---|---|---|---|
| Method | 1 | 0.0904 | 0.0904 | 0.0904 | 0.74 | 0.439 |
| Error | 4 | 0.4895 | 0.4895 | 0.1224 | | |
| Total | 5 | 0.5798 | | | | |

Table 4.5. ANOVA result from the measured $R_a$.

| Source | DF | Seq SS | Adj SS | Adj MS | F | P |
|---|---|---|---|---|---|---|
| Method | 1 | 0.611 | 0.611 | 0.611 | 0.42 | 0.551 |
| Error | 4 | 5.790 | 5.790 | 1.148 | | |
| Total | 5 | 6.401 | | | | |

## 4.7 Discussion - Gap Control Efficiency and Tuning of $K_F$ and $K_R$

Retracting the electrode in the axial direction for near-dry EDM milling with lead angle improves the gap widening efficiency. Figures 4.15(a) and (b) show a simplified drawing of electrode retraction for MDR 1 using proposed and conventional controller, respectively. Geometry of tool electrode wear and electrode hole is omitted because they are more related to MDR 2. Since the proposed controller also retracts along the trajectory, which widens MDR 2 (same retraction direction as the conventional controller), geometry that is related to MDR 2 can be omitted to compare and analyze the effect of electrode retraction. The actual gap widening for conventional controller is $r_{\mathrm{act}} = r\sin(-\alpha)$, where $r_{act}$ is the actual gap widening, $r$ is the retraction distance by the electrode, and $\alpha$ is the lead angle. For the proposed controller, $r_{act} = r$, since the direction of electrode retraction is orthogonal to MDR 1. The efficiency of gap widening of conventional controller compared with proposed controller is equal to $\sin(-\alpha)$ by taking a ratio of $r_{act}$ from conventional and proposed controller. Since $\alpha = -5°$ is used for this study, conventional controller widens only 8.7% of the gap the proposed controller does with the same retraction distance.

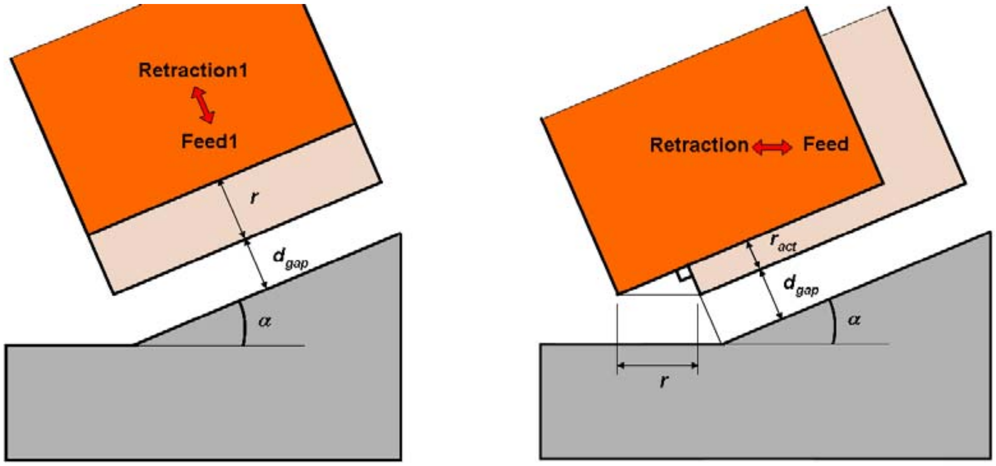

(a) (b)

Figure 4.15. Simplified schematic of gap widening efficiency for (a) proposed controller and (b) conventional controller.

More efficiently enlarged gap improves the mist flow rate through MDR, which helps to maintain a good discharge gap condition by flushing debris. However, the change in gap distance is sensitive to the electrode motion along the electrode orientation. Therefore, controller gains, the value of $K_F$ and $K_R$, are sensitive to the EDM performance. Figures 4.16(a), (b), and (c) show the $u_e$ from machine, $u_{eout}$ sent to EDM controller, and total auxiliary axis position command, respectively, using the proposed controller high controller gains with $K_F = 4$ and $K_R = 8$. The controller is unstable since the $u_e$ and total auxiliary axis position command oscillates constantly. To avoid unstable discharges, the $K_F$ must be reduced, so the electrode does not move forward excessively and cause arcing. The other controller gain, $K_R$ could be increased to avoid unstable discharges since retracting the electrode enlarges the gap distance and decreases the chance of arcing. However, when $K_R$ is too high, gap distance become too large and no discharge occurs. To tune the controller gains, the profile of $u_e$ is monitored during discharge. The controller gains are adjusted to make the $u_e$ not oscillating as in Figure 4.16.

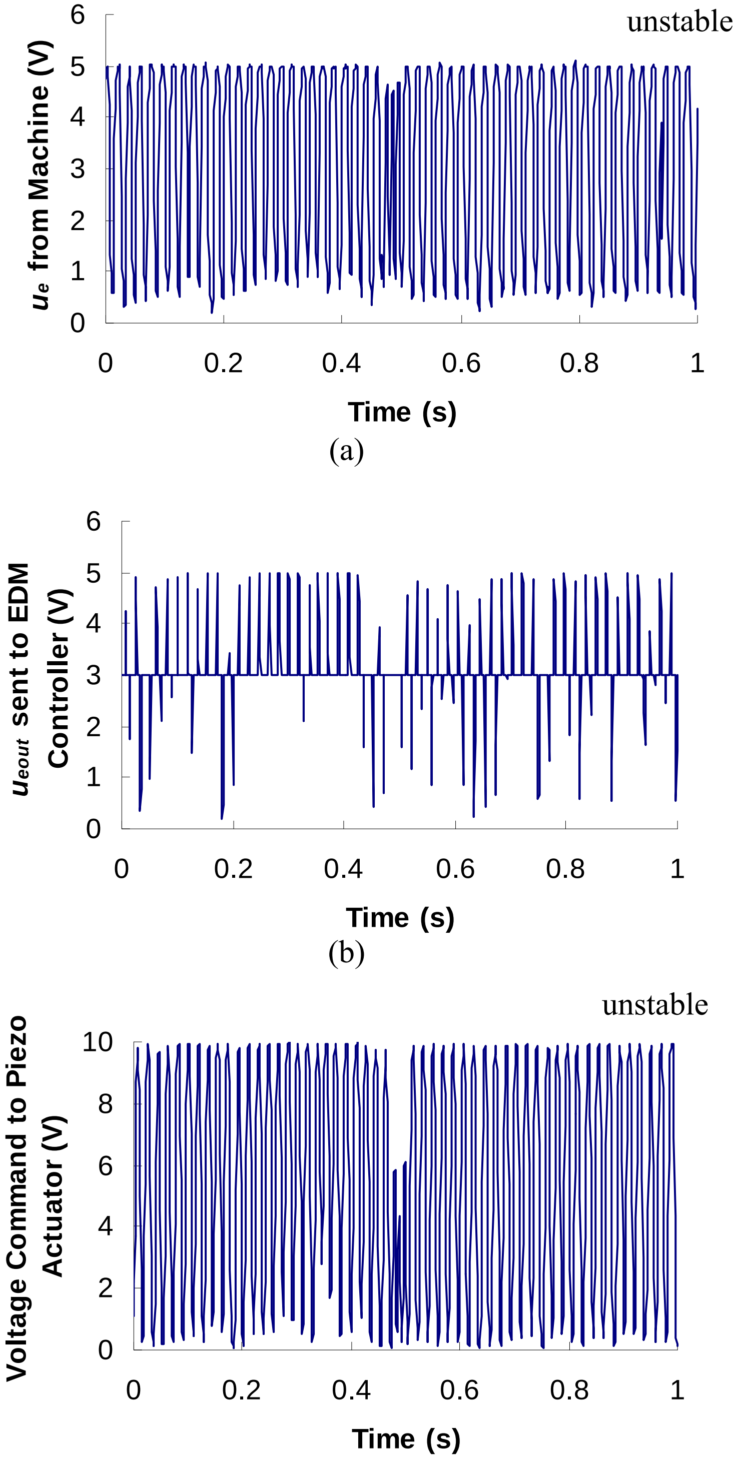

(a)

(b)

(c)

Figure 4.16. Proposed controller with $K_F = 4$ and $K_R = 8$: (a) $u_e$ from machine, (b) $u_{eout}$ sent to EDM controller, and (c) total auxiliary axis position command.

Figures 4.17(a), (b), and (c) show $u_e$ from machine, $u_{eout}$ sent to EDM controller, and total auxiliary axis position command, respectively, using tuned proposed controller with $K_F = 0.1$ and $K_R = 0.5$. Compared with $u_e$ from machine using conventional controller, as shown in Figure 4.18, $u_e$ recovers faster when the proposed controller is used. When $u_{eout}$ becomes less than 3 V (Figure 4.17(b)), the electrode retracts along the trajectory as well. Also small electrode retraction distance using the proposed controller should be noted (Figure 4.17(c)). The piezo actuator only retracts one third of its motion range due to the efficient electrode retraction using the proposed controller algorithm.

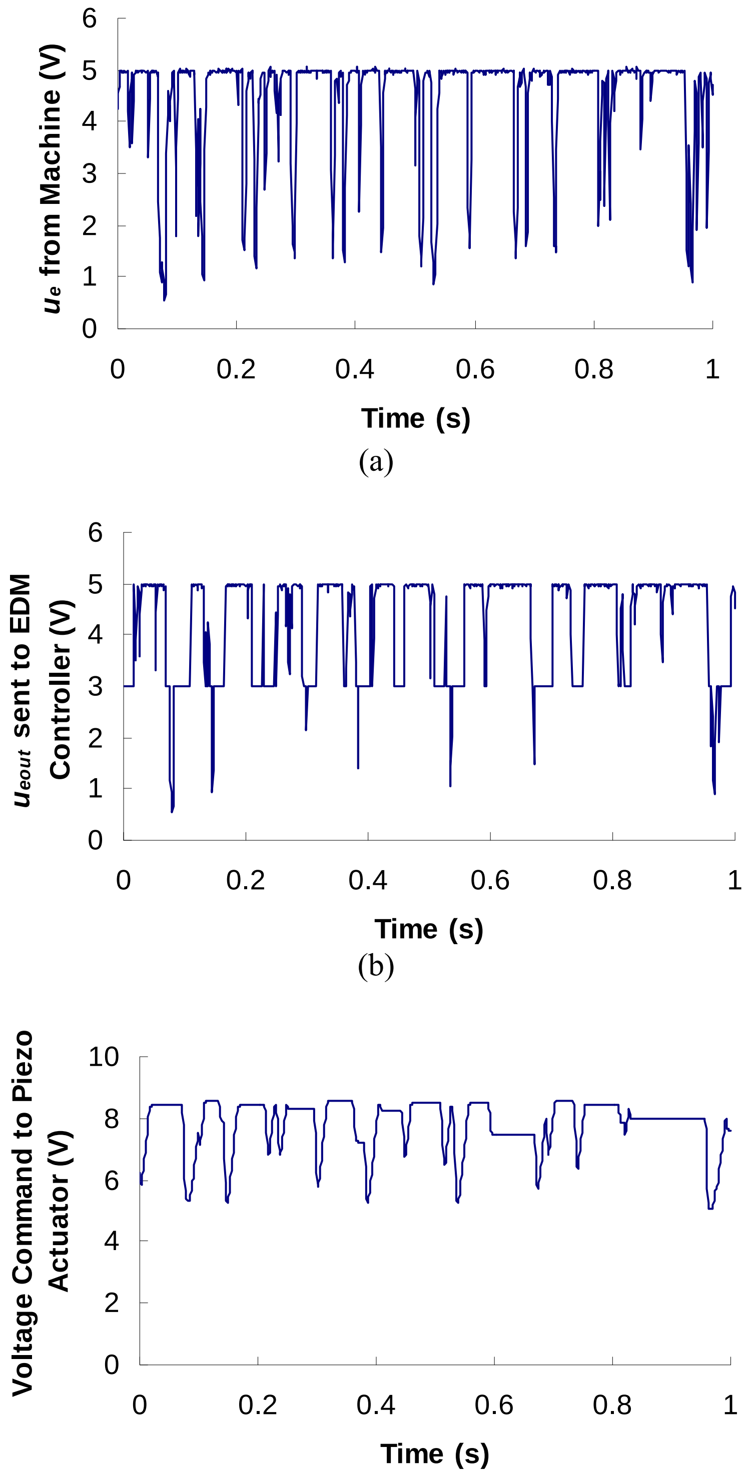

(a)

(b)

(c)

Figure 4.17. Proposed controller with $K_F = 0.1$ and $K_R = 0.5$: (a) $u_e$ from machine, (b) $u_{eout}$ sent to EDM controller, and (c) total auxiliary axis position command.

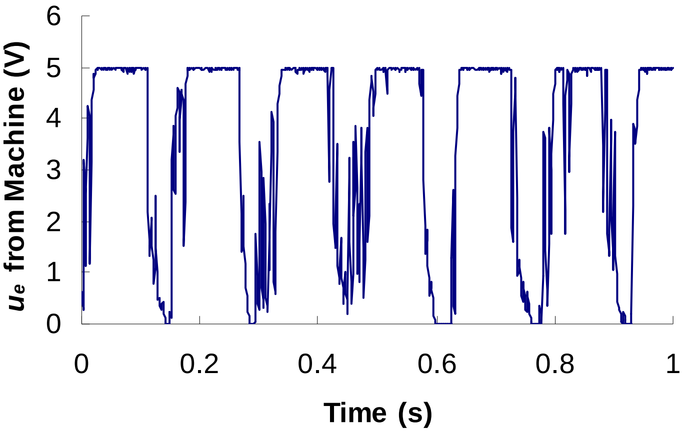

Figure 4.18. $u_e$ from the machine using conventional controller.

## 4.8 Concluding Remarks

A new gap controller for five-axis near-dry EDM milling was presented. The proposed gap controller has the capability to rapidly retract the electrode in its axis direction to more efficiently enlarge the gap distance. The new controller yielded 30% higher *MRR* without sacrificing tool electrode wear ratio and surface roughness. The new gap controller significantly improved the efficiency of electrode retraction on gap distance, increased the mist flow rate through MDR and resulted in the *MRR* improvement.

Current study is utilizes simple simple feed rate override function and requires an external controller and special spindle. An integrated EDM control system can further improve the performance. In the future work, the internal controller within the EDM machine should be modified to control the discharge gap more effectively.

# Chapter 5.

# Summary and Contributions

## 5.1 Summary

This research investigated five-axis near-dry EDM milling. To fully utilize a five-axis machine, the effects of mist flow rate through main discharge region and the electrode orientation on the machining performance were studied. A new tool path planning strategy for five-axis near-dry EDM milling was developed based on the mist flow rate through main discharge region. To flush the debris more efficiently, a new gap control strategy was developed.

### 5.1.1 Investigation on the Effects of Electrode Orientation

The electrode orientation changed the mist flow rate through main discharge region and affected the material removal rate, tool electrode wear ratio, and surface roughness. The followings are the results from the investigation.

- The material removal rate was maximized when the lead angle was 5 degrees. As the lead angle further increased, the material removal rate started to decrease.
- Increase in the surface roughness was observed when lead angle was used.

- Tilt angle had negative effects in material removal rate and tool electrode wear ratio.
- Tilt angle did not affect the surface roughness.
- Inverse relationship between material removal rate and tool electrode wear ratio was observed when discharge parameters were fixed.
- Linear relationship between mist flow rate through main discharge region and material removal rate was observed.
- Inverse relationship between mist flow rate through main discharge region and tool electrode wear ratio was observed.

### 5.1.2 Five-Axis Tool Path Planning for Near-dry EDM Milling

A new tool path planning strategy for five-axis near-dry EDM milling was developed. The effects of the mist flow rate through discharge region on machining performance were considered in the proposed strategy. The proposed strategy consists method to engage, machining of workpiece edge, curvature along feed direction, curvature along cross feed direction and path interval. The experimental verification yielded highest *MRR*.

### 5.1.3 Gap Control of Five-Axis Near-Dry EDM Milling

A new gap controlling strategy for five-axis near-dry EDM milling was developed. The proposed strategy retracts the electrode more efficiently to flush the debris from the discharge region. It retracts the electrode in the direction of electrode orientation while the conventional gap controller retracts the electrode along the trajectory. To implement the controller, a spindle system that can retract the electrode along its orientation was designed and fabricated. The proposed controller improved the material removal rate by 30% compared with conventional controller.

## 5.2 Scientific Contributions

Comprehensive research on five-axis near-dry EDM milling is new. The current state-of-the-art is limited to three-axis EDM milling in wet or dry condition. Active research in EDM milling are mainly concentrated on electrode shortening compensation, investigation of discharge parameters, high bandwidth gap control, and ultrasonic vibration to enhance the debris flushing. This research aims to optimize the EDM milling process by effectively utilizing a five-axis machine.

The scientific contributions of this research are summarized as follows.

- Analysis of the high pressure mist flow in the discharge gap established a relationship between the flow of dielectric fluid in the discharge gap and the machining performance.
- Incorporation of fluid flow rate with the new tool path planning strategy extended the performance limits of the current state-of-the-art in EDM milling.
- The development of new proposed gap controlling strategy based on the improvement of mist flow rate contributed to further extension of performance limit for five-axis EDM milling.

## 5.3 Future work

Future work for this study includes following three areas:

1. Detailed analysis of fluid flow rate through MDR and machining performance
2. Development of CAM for five-axis near-dry EDM milling
3. Improvement of proposed gap controller.

Experiments with the effect of electrode orientation and mist flow rate through MDR indicated the mist flow rate has weaker effects on machining performance when the inlet pressure was varied. Further analysis of mist flow rate through MDR and machining performance that incorporates the geometry of MDR will be investigated.

Current path planning strategy is limited for cylindrical surface. In order to develop the CAM system, 3D expression of sculptured surface using non-uniform rational B-spline (NURBS) or tetrahedral will be used.

To improve the proposed gap controller, position of the piezo actuator will be closed using the strain gage sensor mounted within the actuator. EDM machine's main controller will also be modified to find the optimum retraction direction.

# Appendix.

# Design of Spindle

The spindle system consists of three subassemblies. The first subassembly separates the rotational motion from the axial motion from piezo actuator. The second subassembly transmits rotational motion while allowing axial motion. The third subassembly is the spindle frame that minimizes structural deformation caused by the excitation of piezo actuator. Table A.1 shows the bills of material for the spindle system.

Table A.1. Bill of Material for the Spindle System.

| Part # | Vendor | Quantity |
|---|---|---|
| 101 | Fabricated | 1 |
| 102 | Fabricated | 1 |
| 103 | Fabricated | 1 |
| P-845.30 | Physik Instrumente | 1 |
| P-176.60 | Physik Instrumente | 1 |
| 51101 | SKF | 2 |
| M02470303 | Norgren | 1 |
| 201 | Fabricated | 1 |
| 202 | Fabricated | 1 |
| 203 | Fabricated | 1 |
| 204 | Fabricated | 1 |
| 205 | Fabricated | 1 |
| 206 | Fabricated | 1 |
| 207 | Fabricated | 1 |
| TG30 0 0100 T29 | Busak-Shamban | 1 |
| 0.465x0.70 70BNB | Apple Rubber Products | 1 |
| OR1000500-N | Busak-Shamban | 2 |
| LTR 10[a] | THK | 1 |
| TNTR10-1-0-3 | Misumi | 2 |
| R20-2020 | Everest Industries | 1 |
| 301 | Fabricated | 1 |
| 302 | Fabricated | 1 |
| 303 | Fabricated | 2 |
| 304 | Fabricated | 1 |
| 305 | Fabricated | 1 |
| 306 | Fabricated | 2 |
| 82-830-0 | Crouzet | 1 |
| IKF200-A-120-B75-X45-F56-Y35-G140 | Misumi | 1 |

Following pages show assembly and the detailed design of fabricated components.

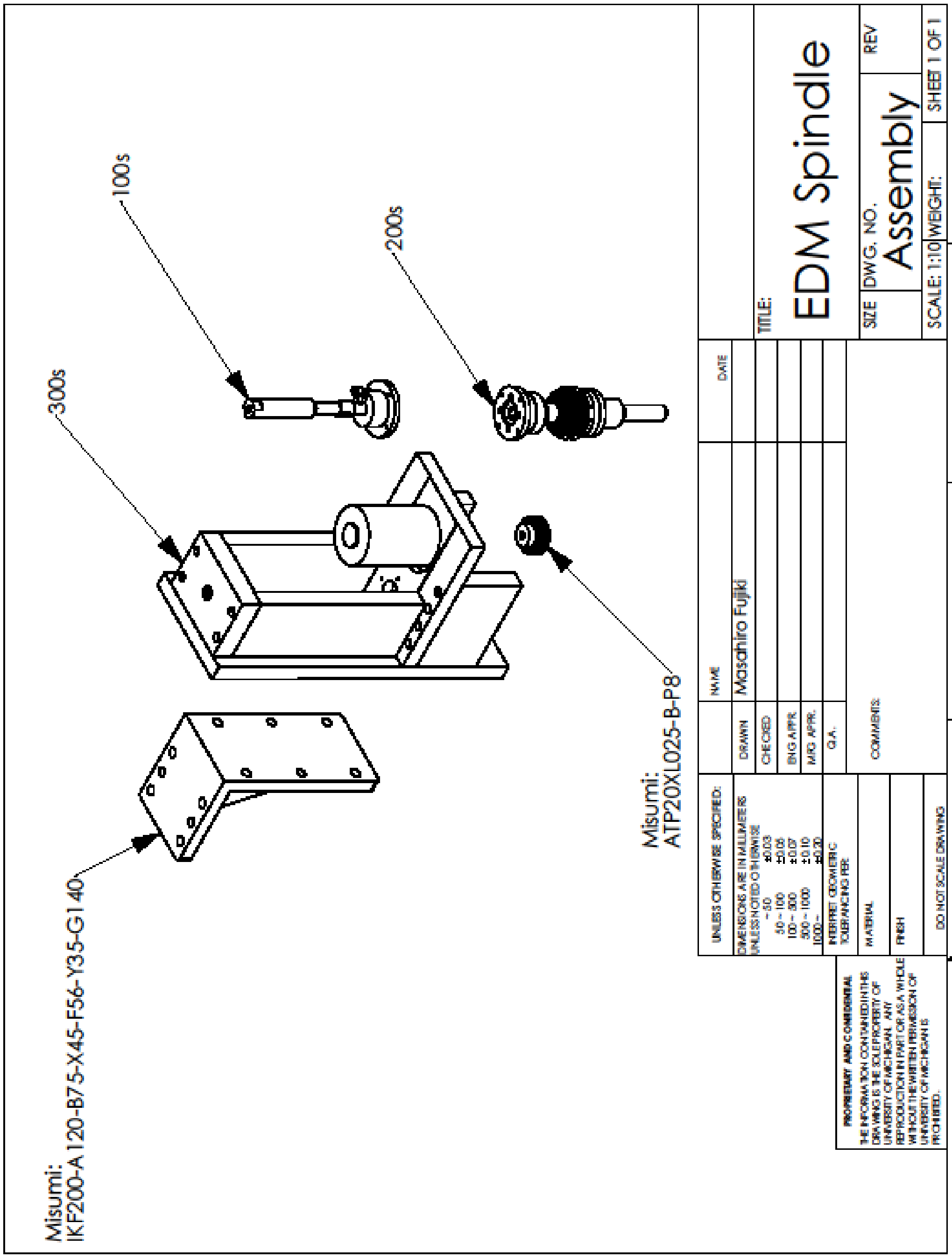

Figure A.1. Assembly of the spindle system.

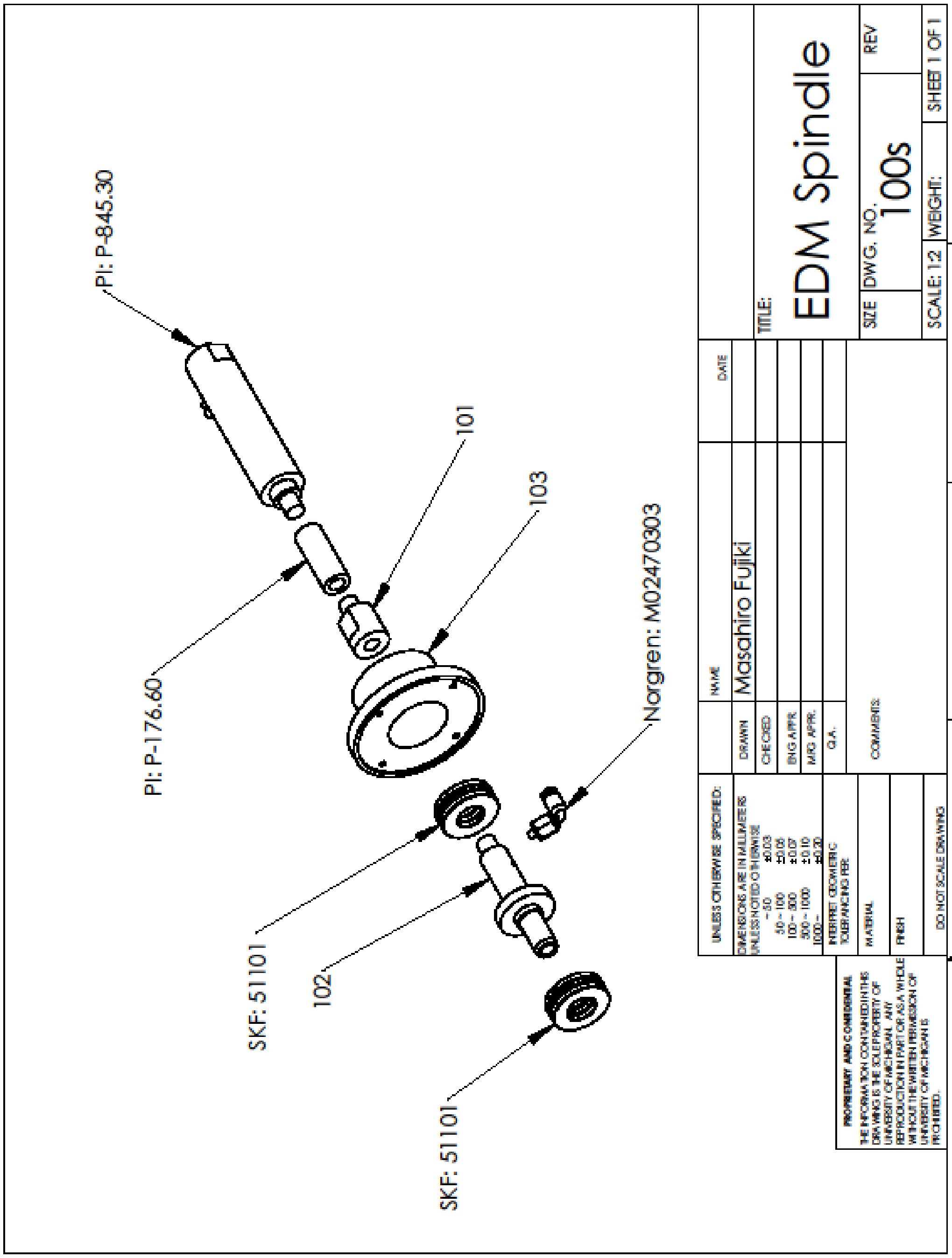

Figure A.2. Subassembly of 100’s series.

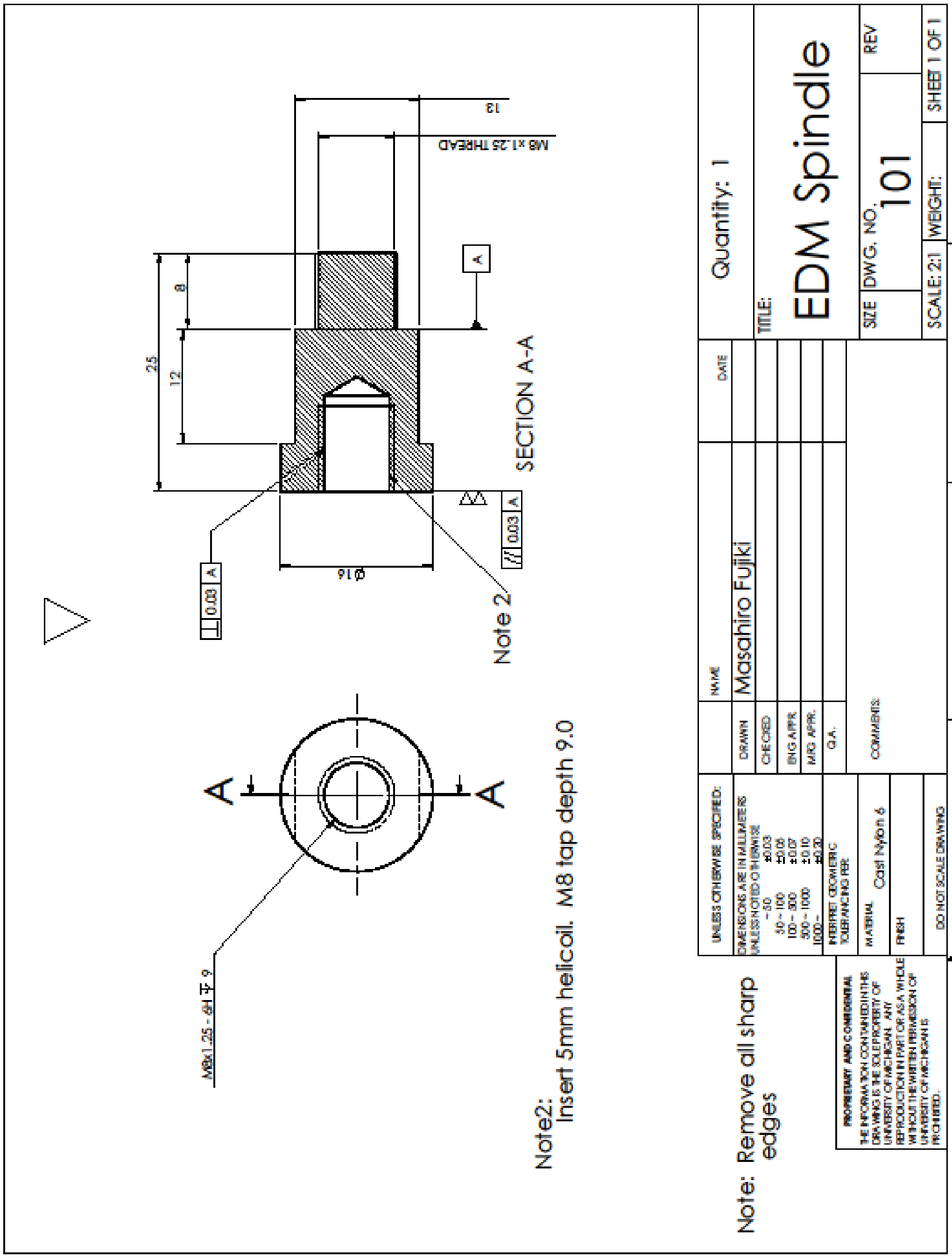

Figure A.3. 2D CAD drawing of part 101.

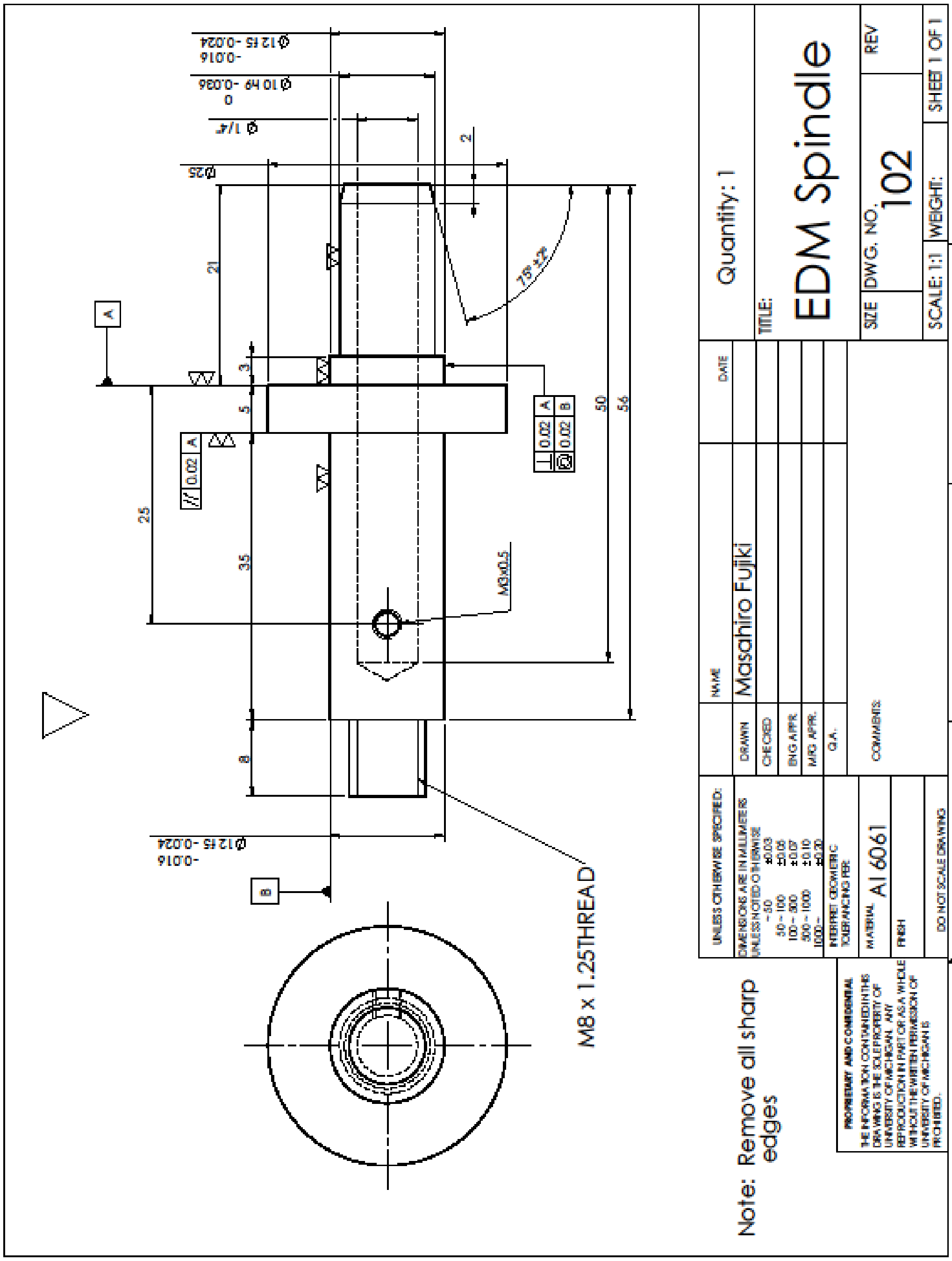

Figure A.4. 2D CAD drawing of part 102.

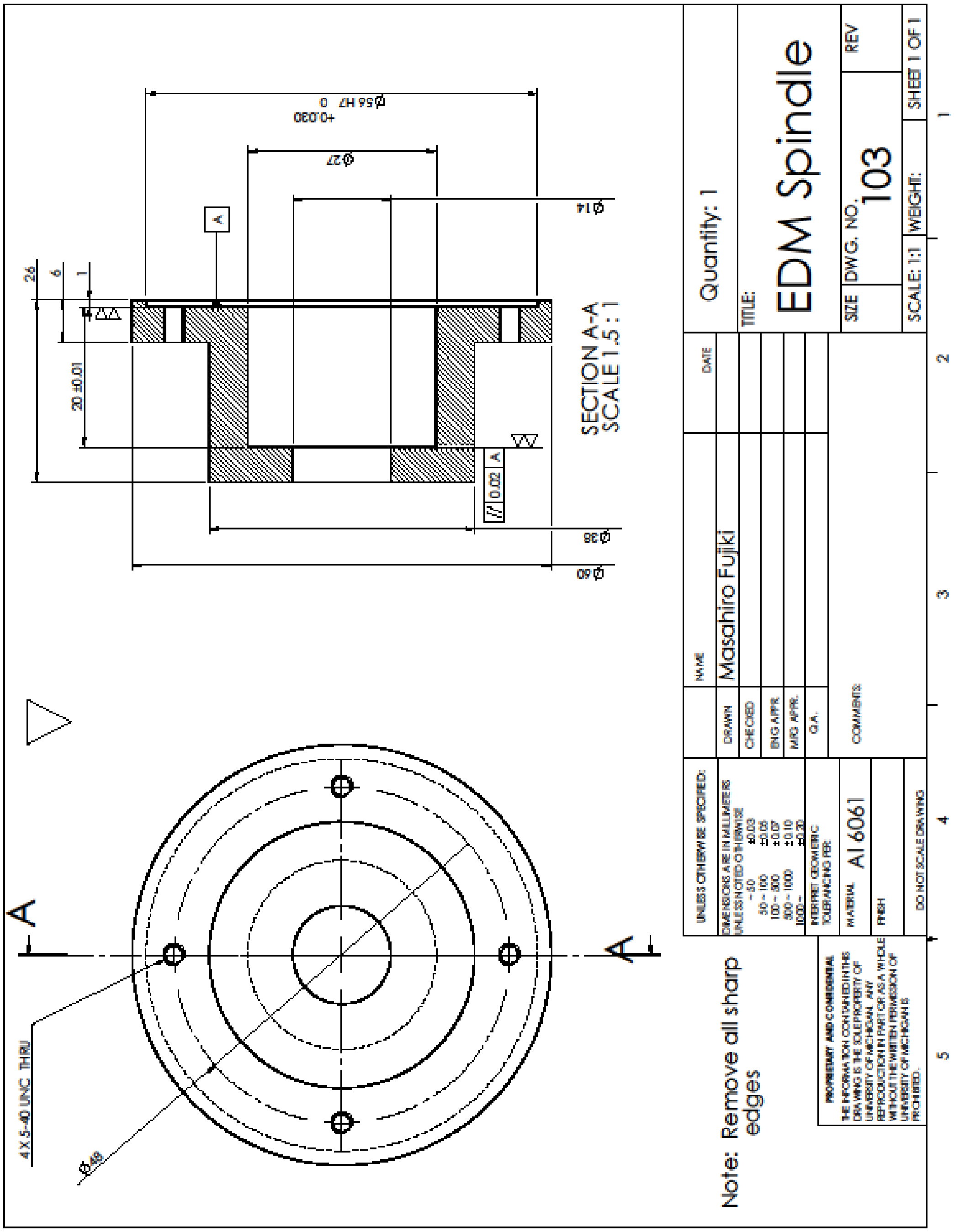

Figure A.5. 2D CAD drawing of part 103.

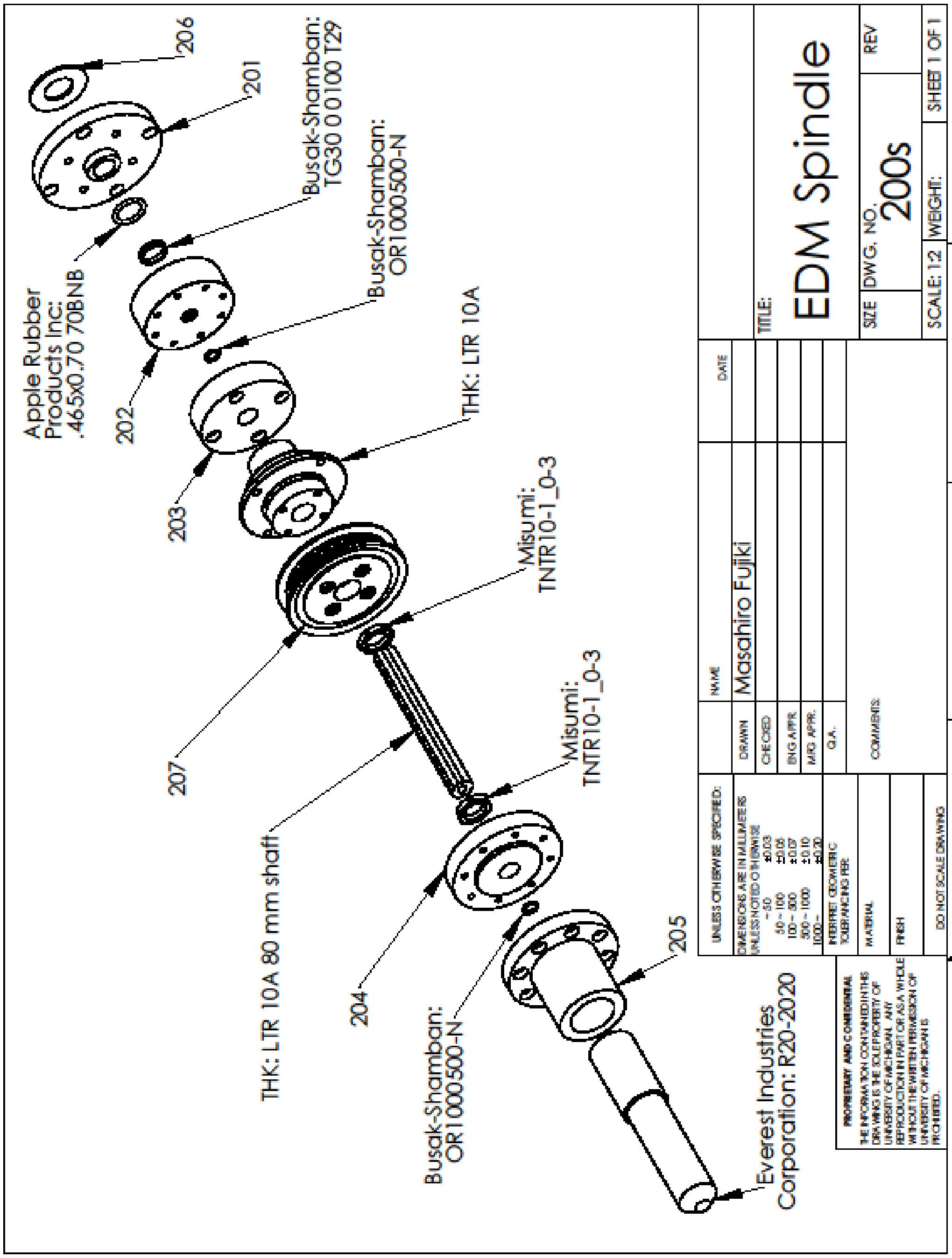

Figure A.6. Subassembly of 200's series.

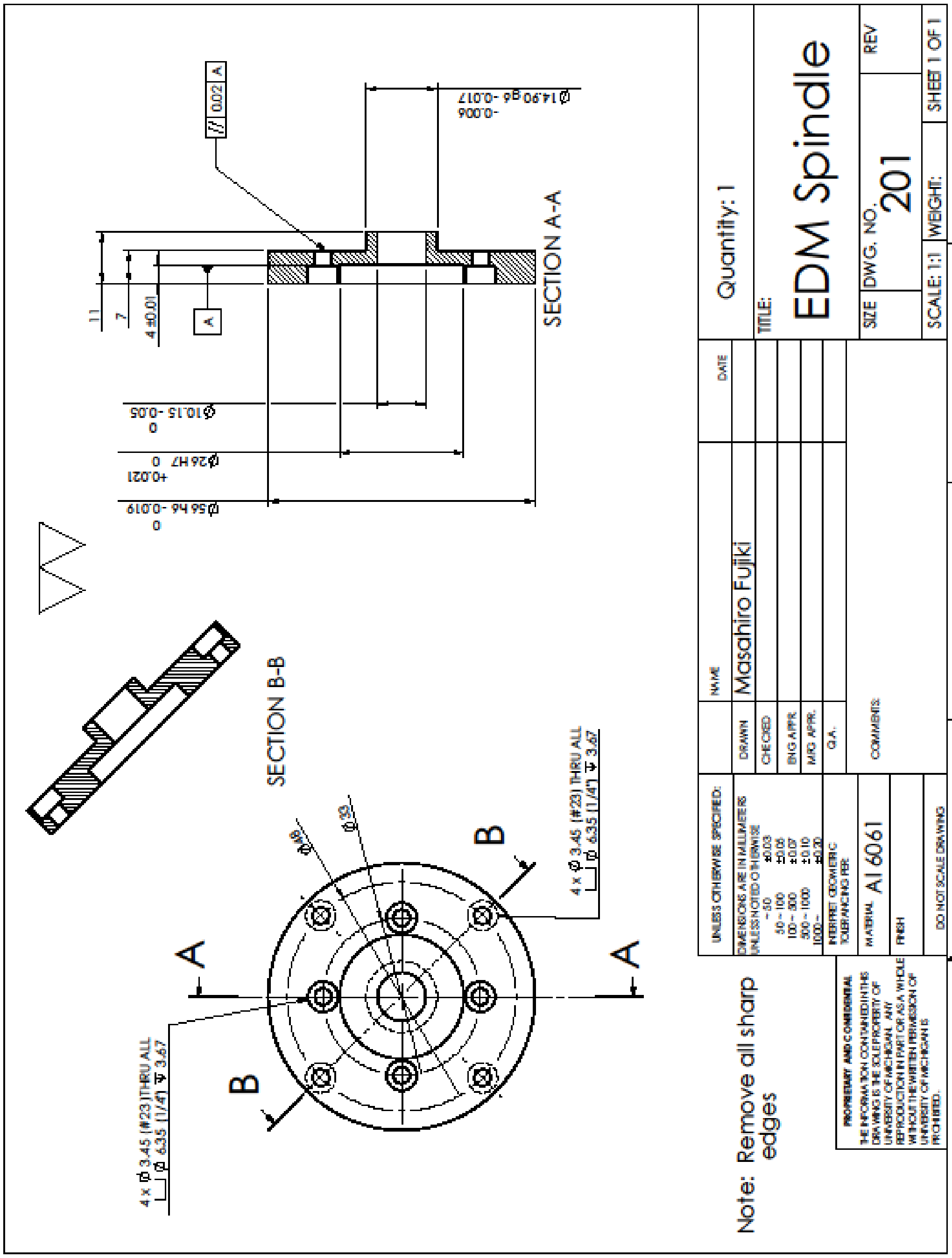

Figure A.7. 2D CAD drawing of part 201.

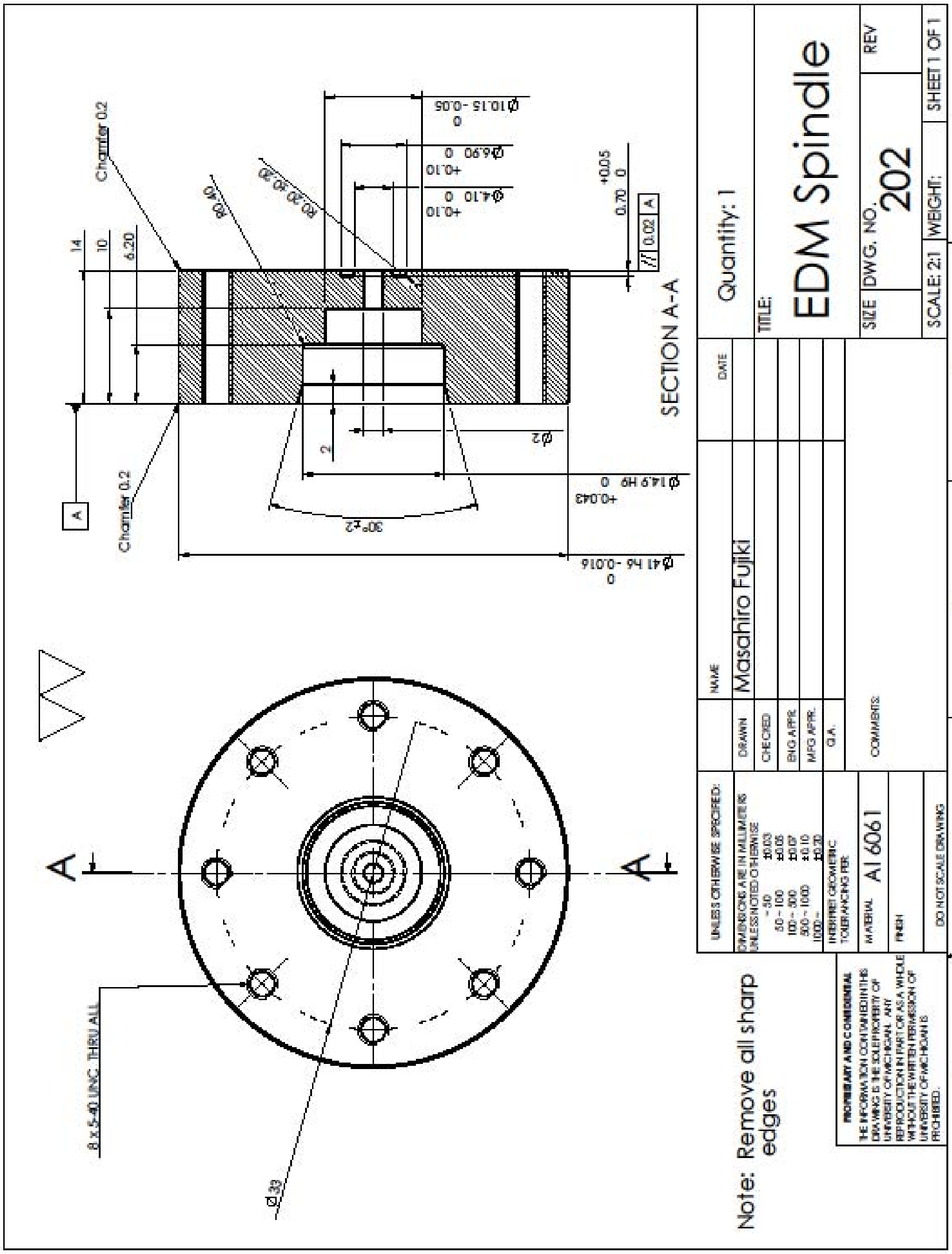

Figure A.8. 2D CAD drawing of part 202.

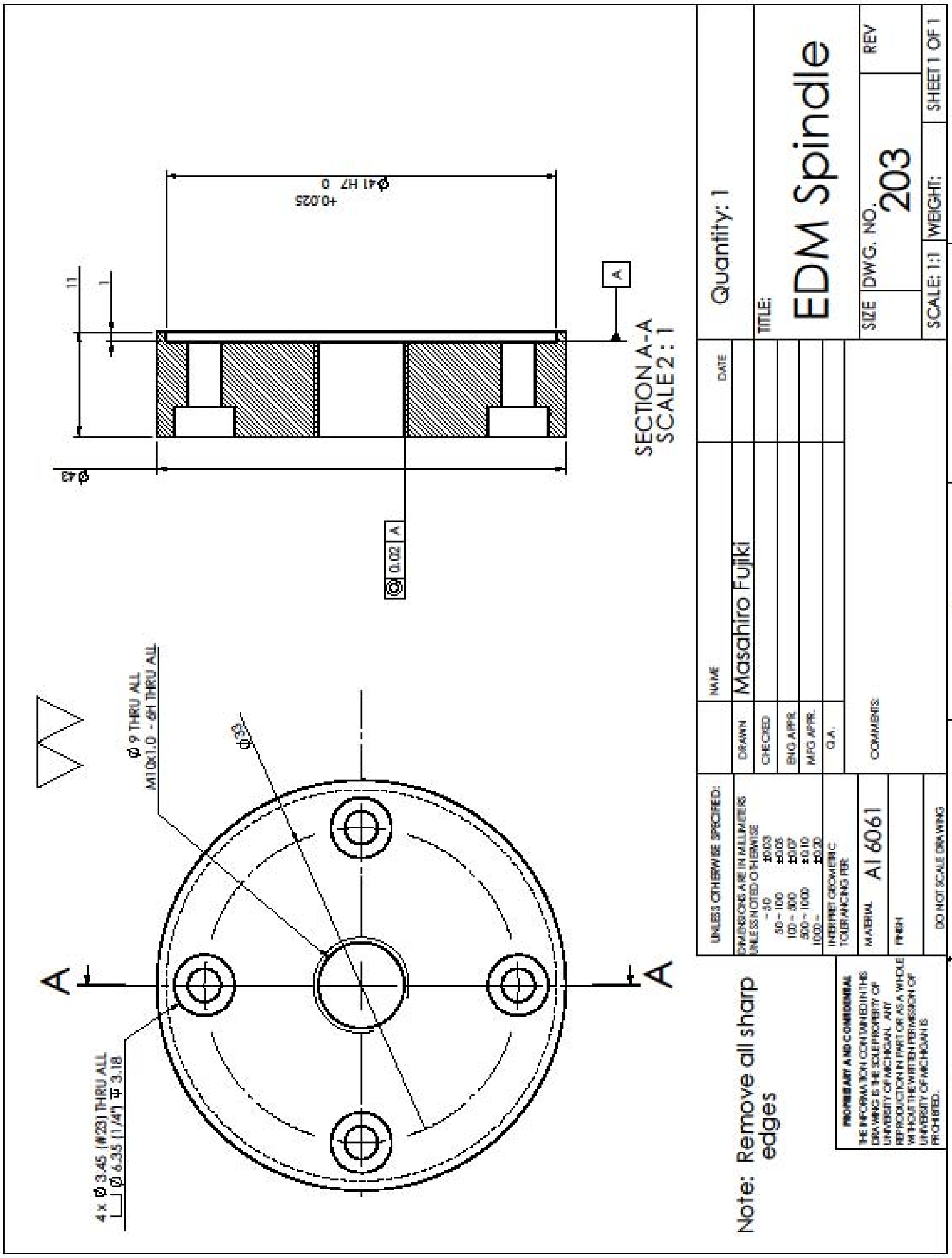

Figure A.9. 2D CAD drawing of part 203.

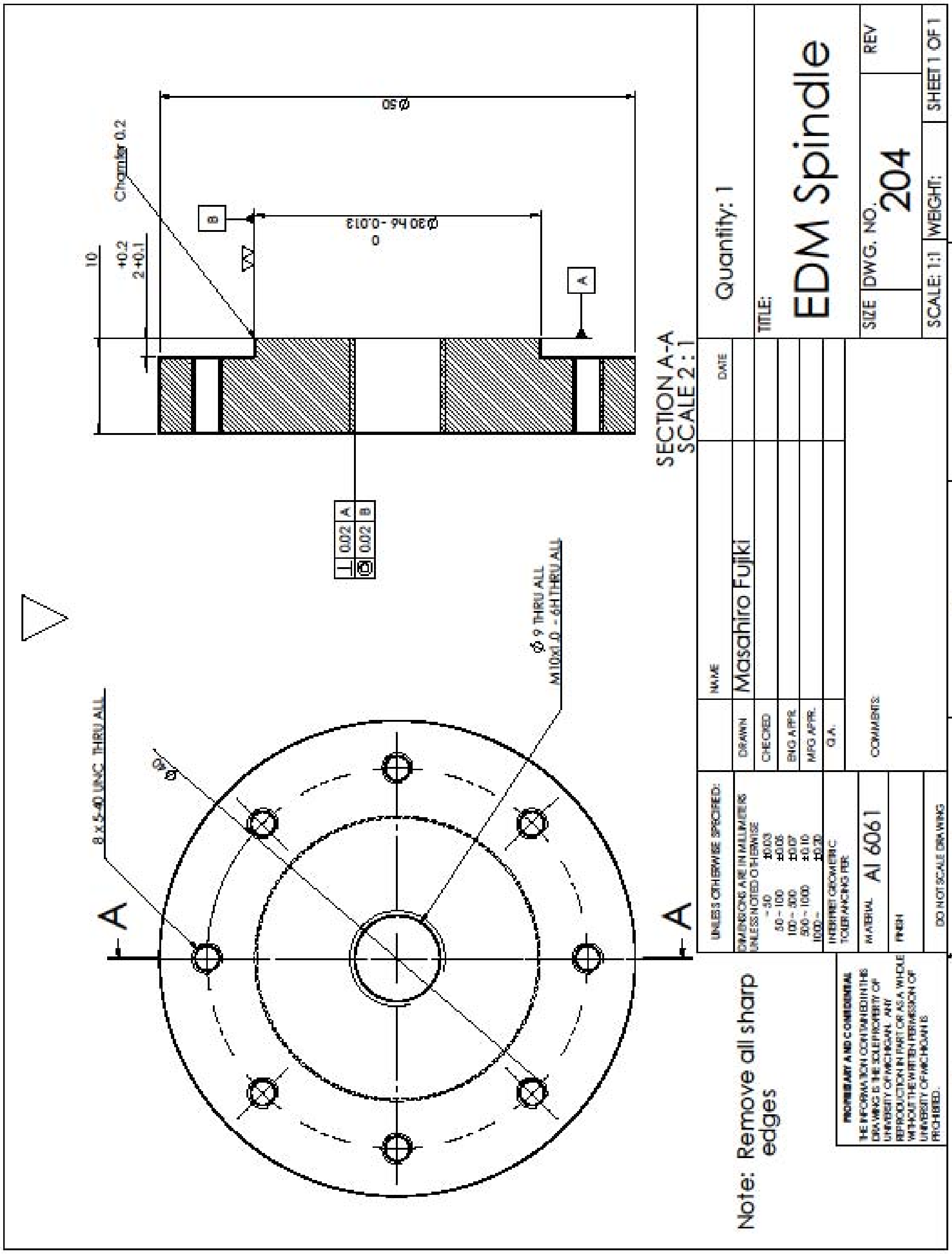

Figure A.10. 2D CAD drawing of part 204.

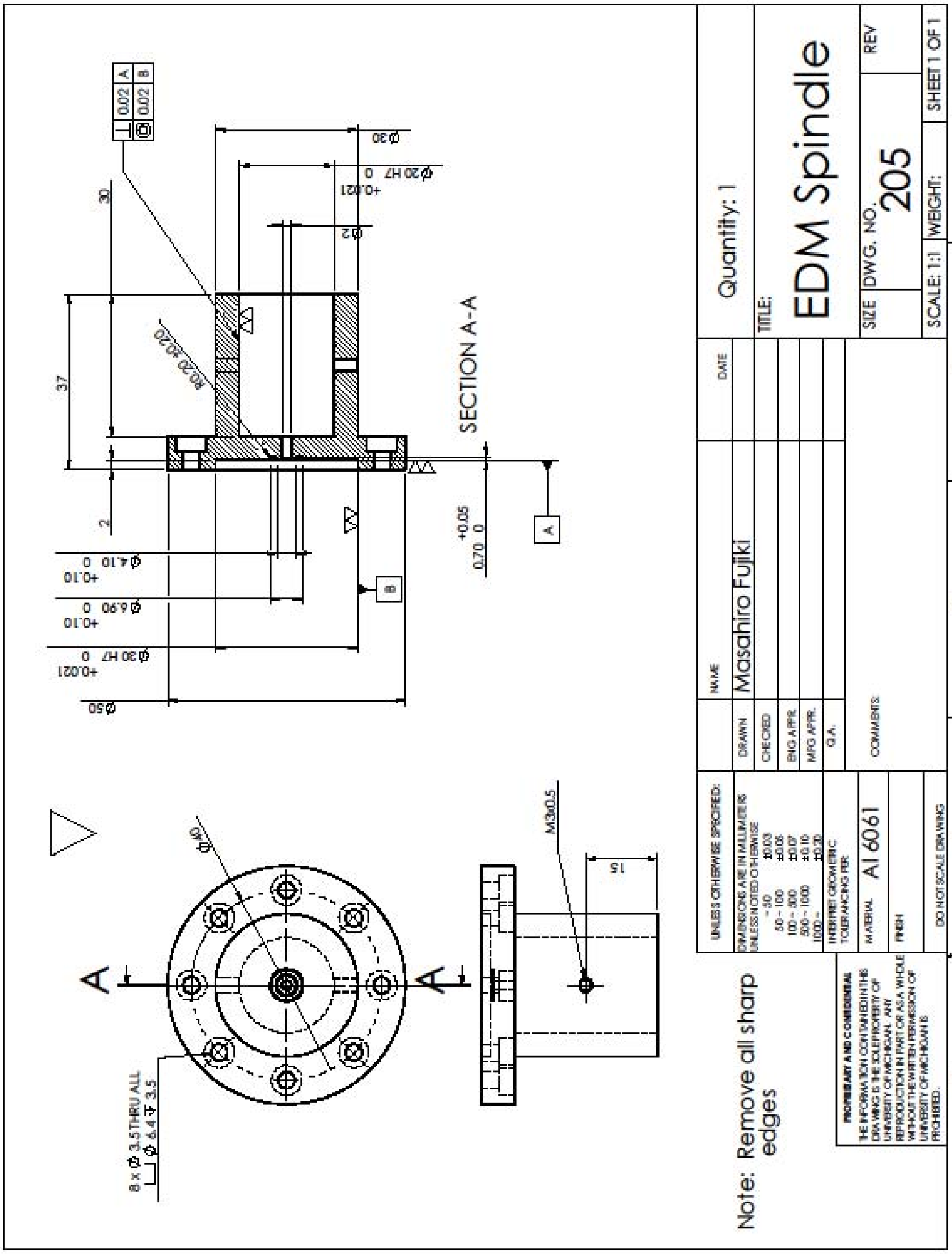

Figure A.11. 2D CAD drawing of part 205.

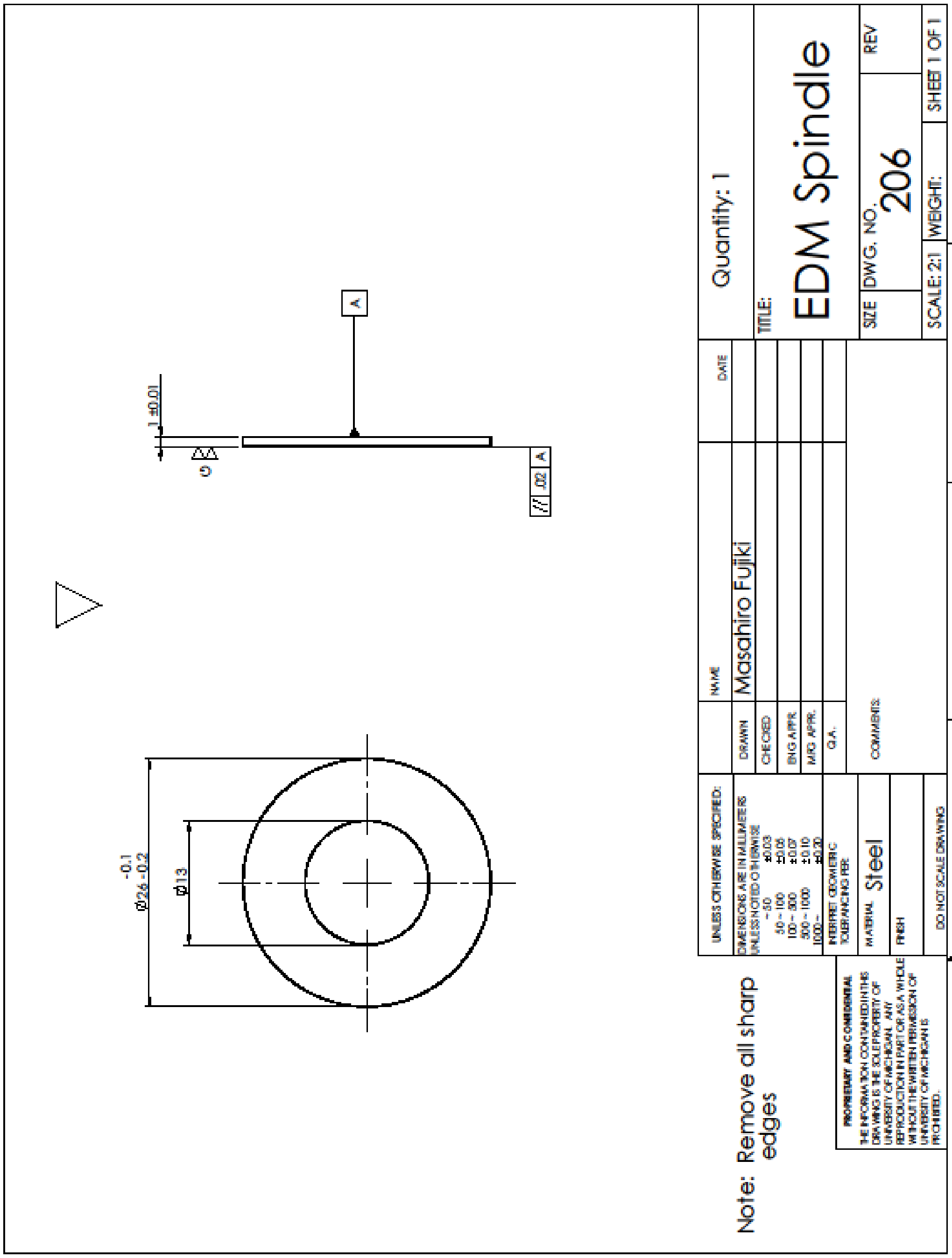

Figure A.12. 2D CAD drawing of part 206.

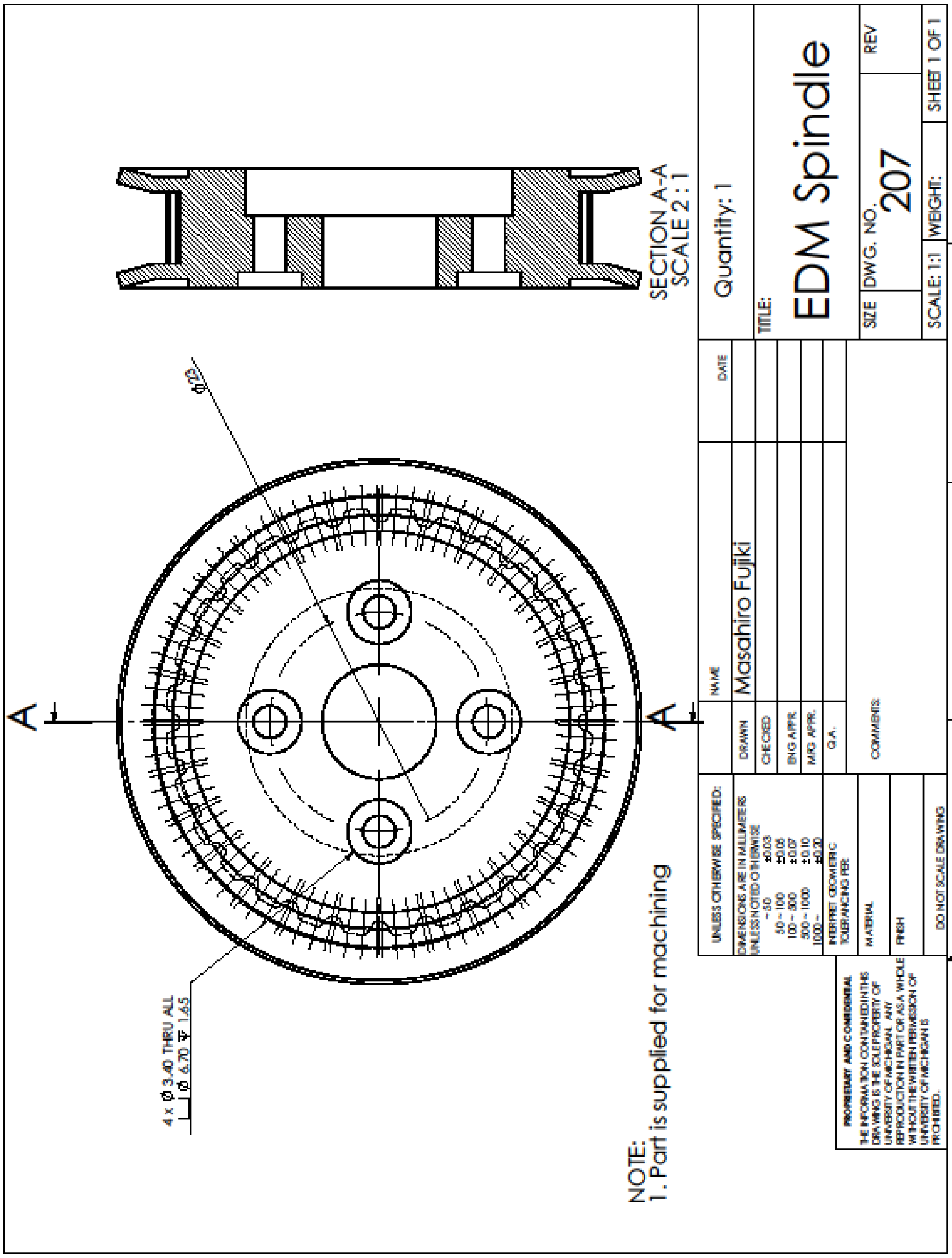

Figure A.13. 2D CAD drawing of part 207.

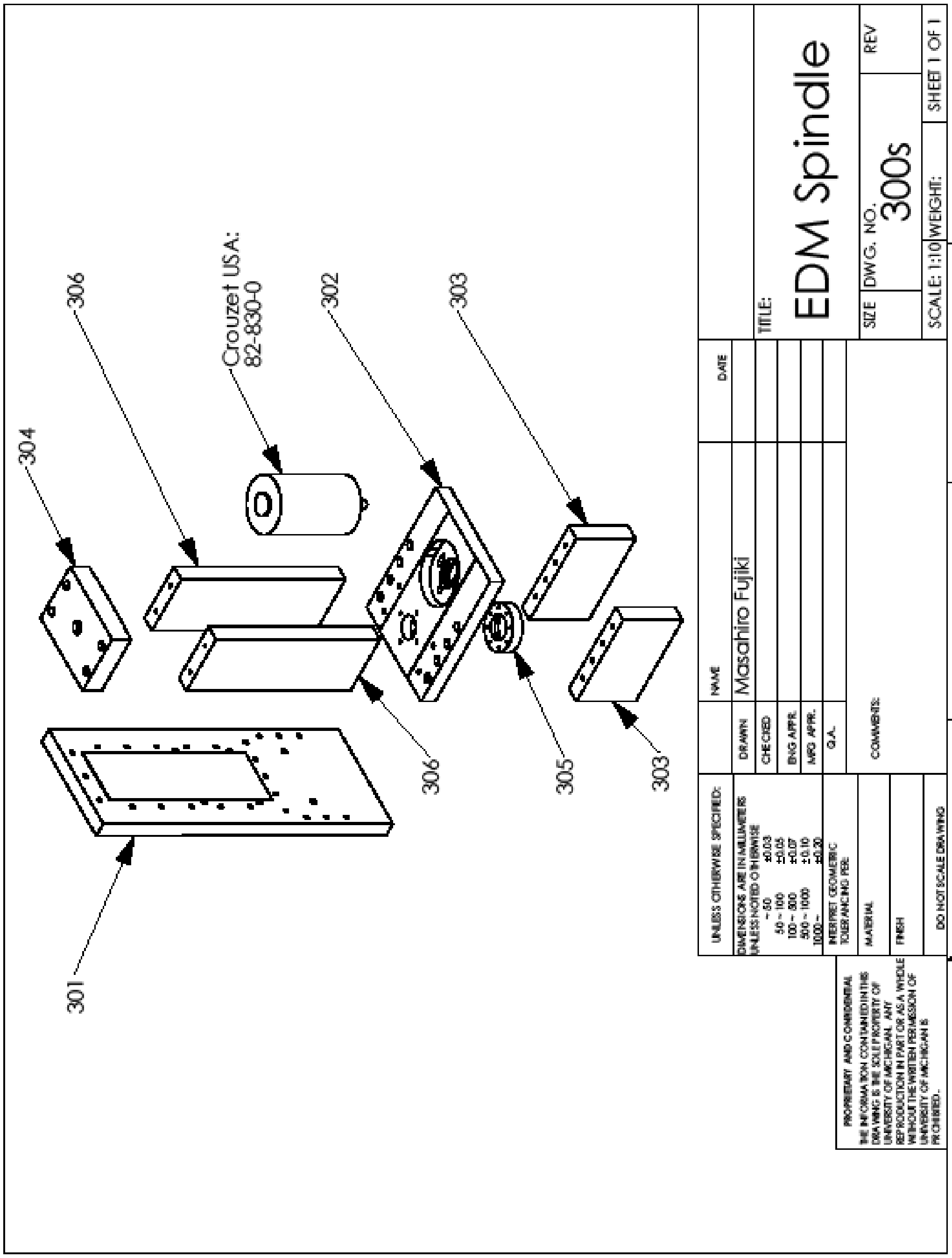

Figure A.14. Subassembly of 300's series.

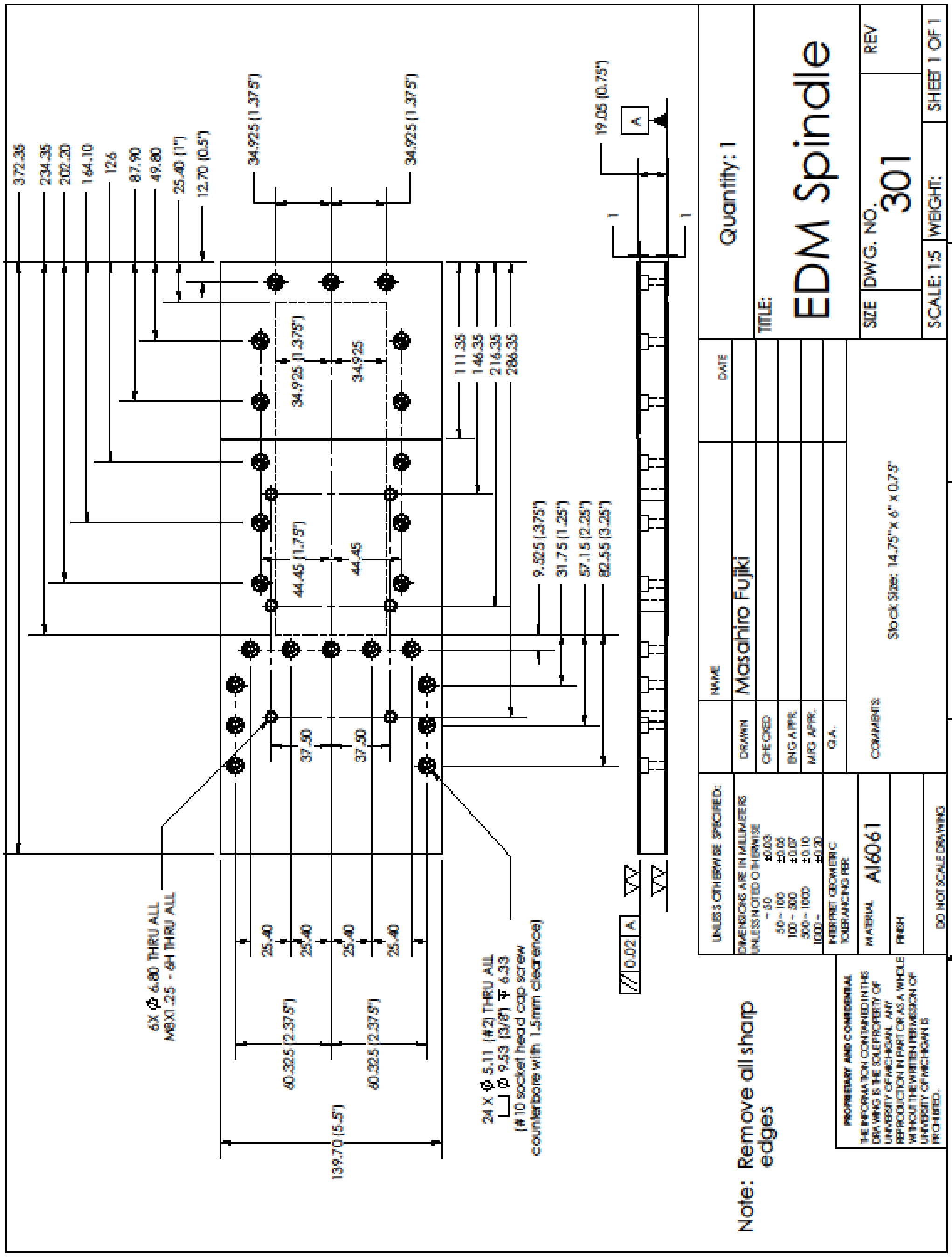

Figure A.15. 2D CAD drawing of part 301.

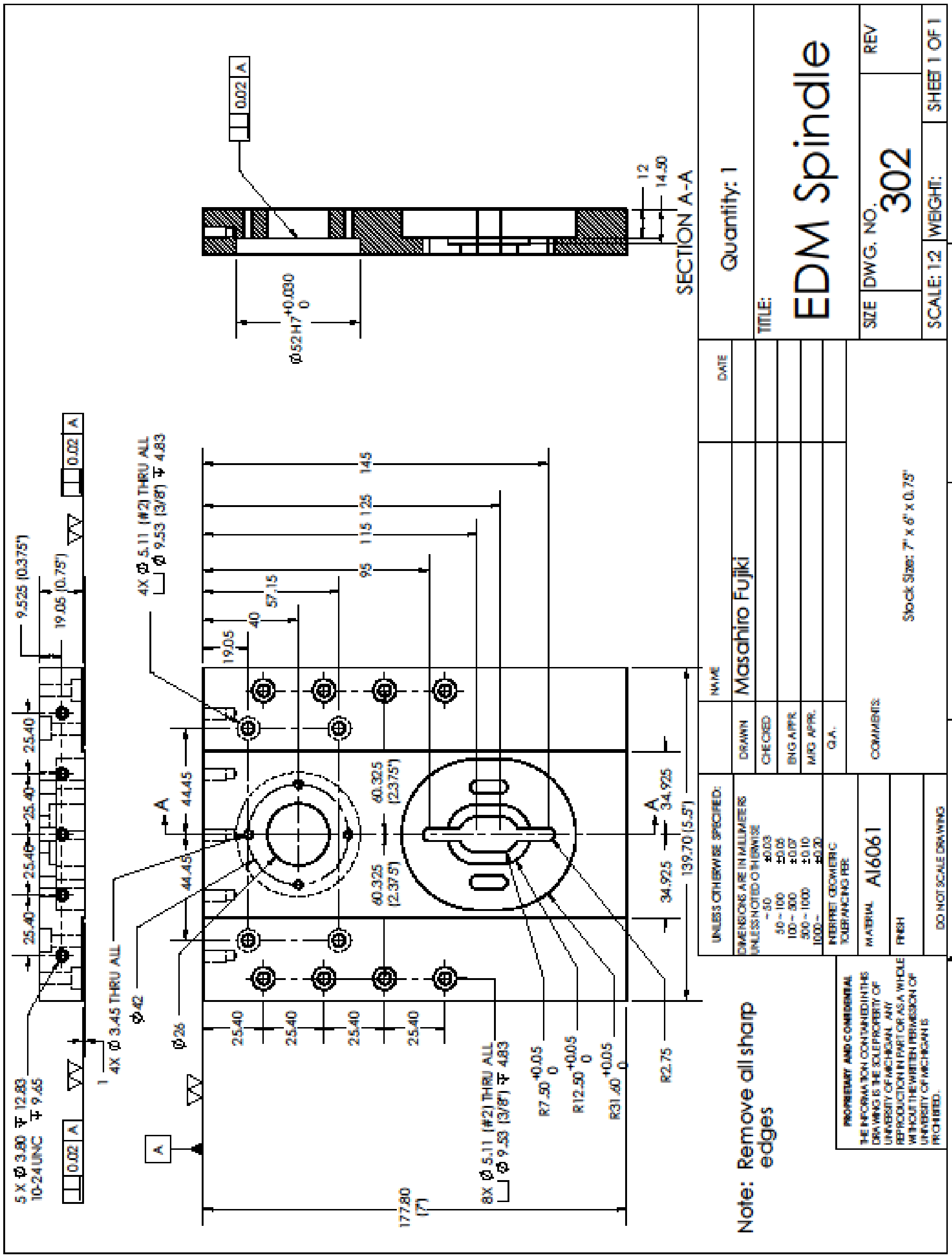

Figure A.16. 2D CAD drawing of part 302.

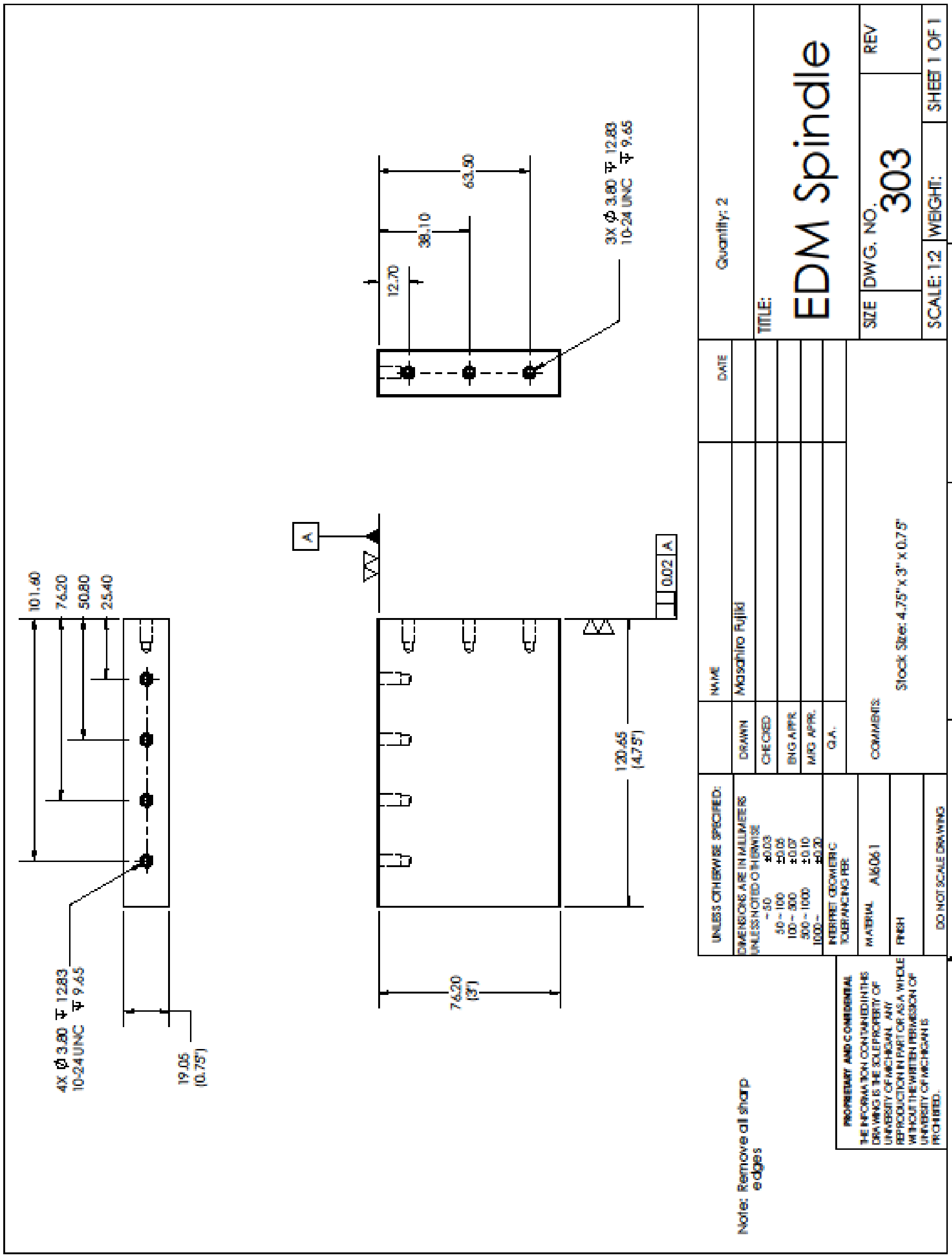

Figure A.17. 2D CAD drawing of part 303.

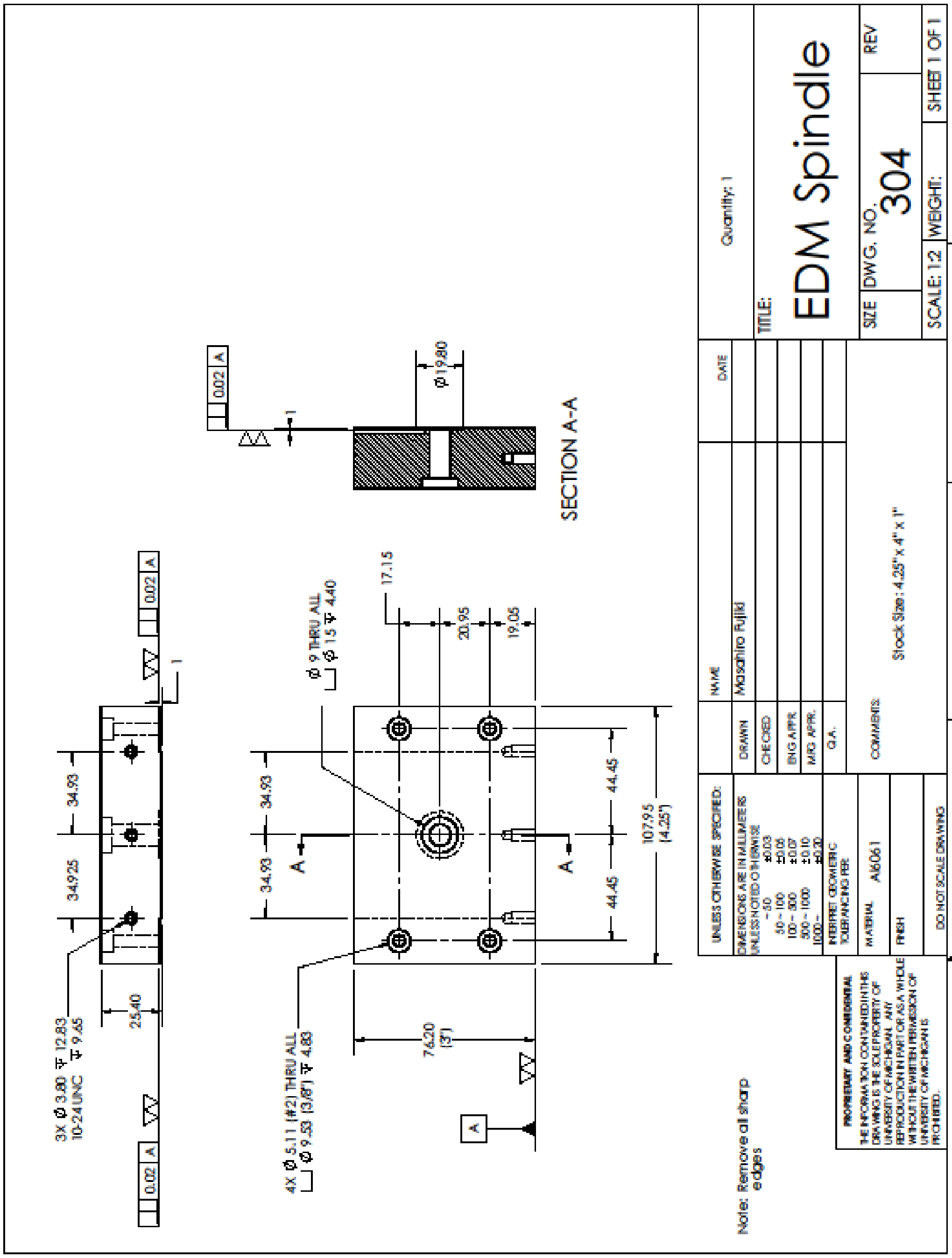

Figure A.18. 2D CAD drawing of part 304.

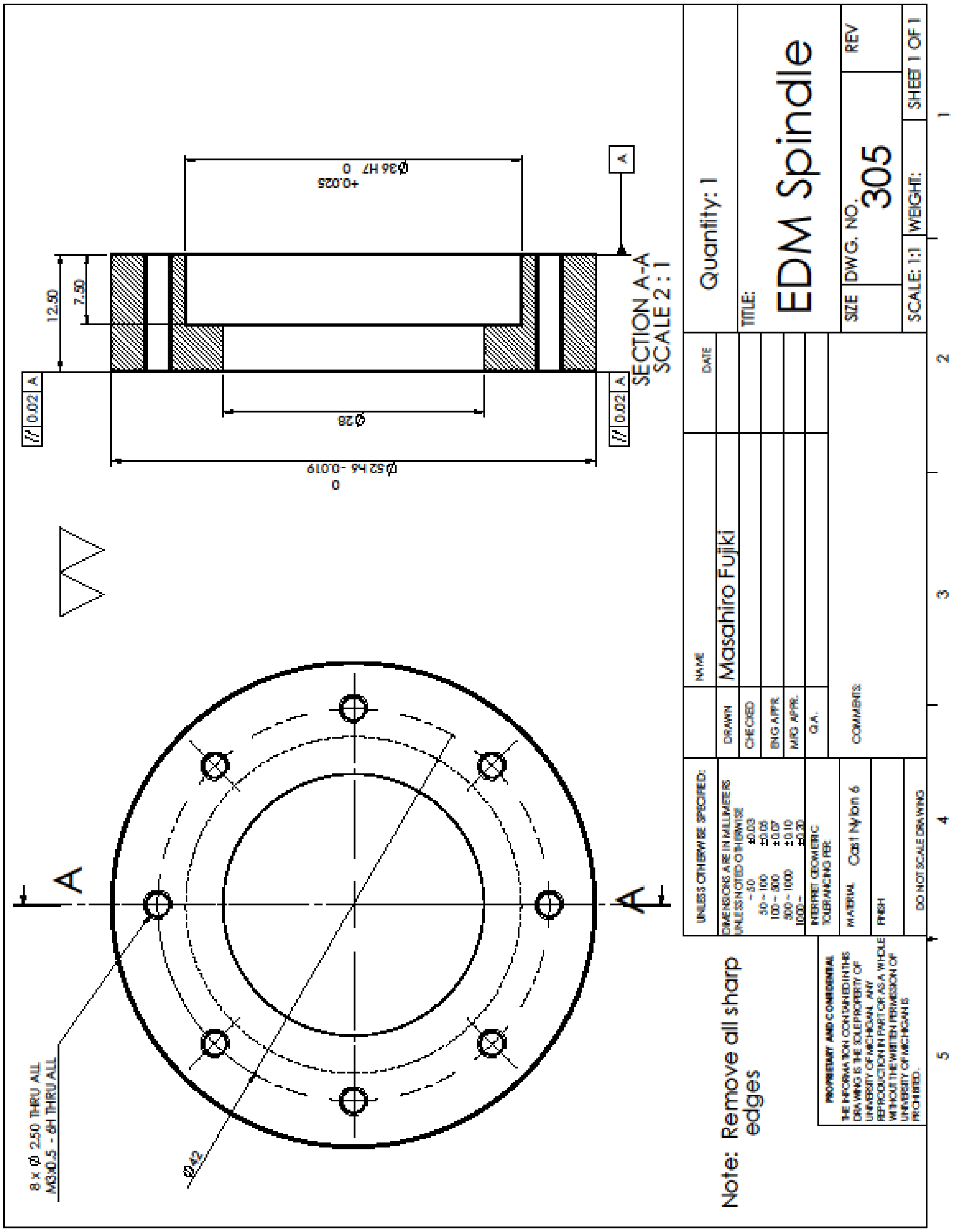

Figure A.19. 2D CAD drawing of part 305.

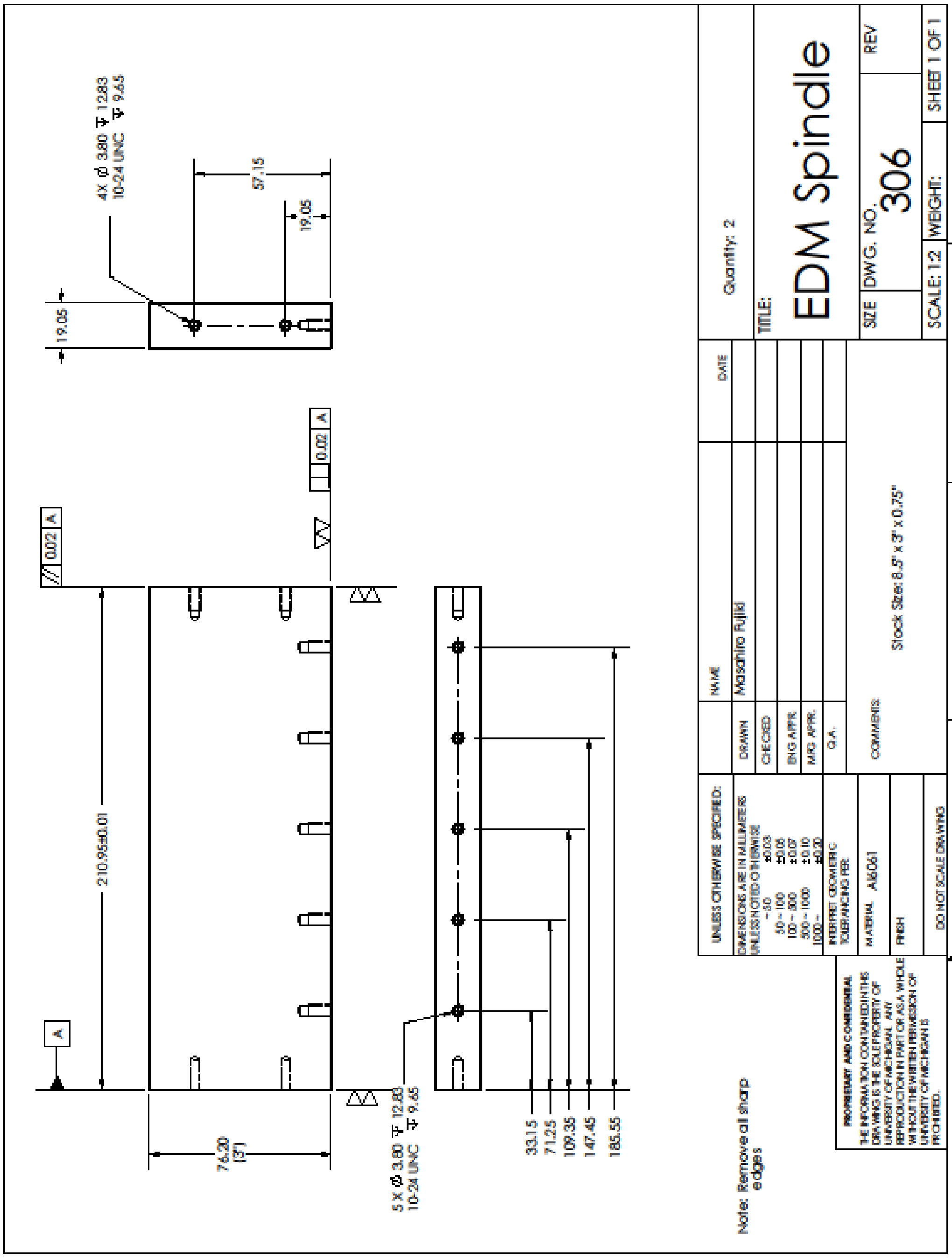

Figure A.20. 2D CAD drawing of part 306.

# References

Affouard, A., Duc, E., Lartigue, C., Langeron, J.M., Bourder, P. (2004), Avoiding 5-axis singularities using tool path deformation, International Journal of Machine Tools and Manufacture, 44 (4), 415-425

Bayramoglu, M., Duffill, A.W. (1994), Systematic investigation on the use of cylindrical tools for the production of 3D complex shapes on CNC EDM machines, International Journal of Machine Tools and Manufacture, 34 (3), 327-339

Beltrami, I., Joseph, C., Clavel, R., Bacher, J.P., Bottinelli, S. (2004), Micro- and nanoelectric-discharge machining, Journal of Materials Processing Technology, 149 (1-3), 263-265

Bleys, P., Kruth, J.P., Lauwers, B. (2004), Sensing and compensation of tool wear in milling EDM, Journal of Materials Processing Technology, 149 (1-3), 139-146

Chang, Y.F (2002), VSS controller design for gap control of EDM, Japan Society of Mechanical Engineering, International Journal, Ser. C 45 (3), 712–721

Chang, Y.F, Chiu, Z.H. (2004), Electrode wear-compensation of electric discharge scanning process using a robust gap-control, Mechatronics, 14 (10), 1121-1139

Crookall, J.P. (1979), A theory of planar electrode-face wear in EDM, Annals of the CIRP, 28 (1), 125-129

Dauw, D., Snoeys, R. (1986), On the derivation and application of a real-time tool wear sensor in EDM, Annals of the CIRP, 35 (1), 111-116

Ding, S., Jiang, R. (2004), Tool path generation for 4-axis contour EDM rough machining, International Journal of Machine Tools and Manufacture, 44 (14), 1493-1502

Enache, S., Opran, C., Stoica, G. (1990), The study of EDM with forced vibration of tool-electrode, Annals of the CIRP, 39 (1), 167-170

Erkorkmaz, K., Altintas Y. (2001), High speed CNC system design. Part I: jerk limited trajectory generation and quintic spline interpolation, International Journal of Machine Tools and Manufacture, 41 (9), 1323-1345

FLUENT 6.3 User’s Guide, Fluent Inc., (2003) Fujiki, M., Ni, J., Shih, A.J., (2009) Investigation of the Effect of Electrode Orientation and Fluid Flow in Near-Dry EDM Milling, International Journal of Machine Tools and Manufacture, 49(10), 749-758

Gao, C., Liu, Z. (2003), A study of ultrasonically aided micro-electrical-discharge machining by the application of workpiece vibration, Journal of Materials Processing Technology, 139 (1-3), 226-228

Ho, K. H., Newman, S. T. (2003), State of the art electrical discharge machining (EDM), International Journal of Machine Tools and Manufacture, 43 (13), 1287-1300

Imai, Y., Nakagawa, T., Miyake, H., Hidai, H., Tokura, H. (2004), Local actuator module for highly accurate micro-EDM, Journal of Materials Processing Technology, 149 (1-3), 328-333

Imai, Y., Satake, A., Taneda, A., Kobayashi, K. (1996), Improvement of EDM machining speed by using high frequency response actuator, International Journal of Electrical machining, 1, 21-26

Jun, C.S., Cha, K, Lee, Y.S. (2003), Optimizing tool orientations for 5-axis machining by configuration-space search method, Computer Aided Design, 35 (6), 549-566

Kao, C.C., , Shih, A. J., Miller, S. F. (2008a) Fuzzy Logic Control of Micro-Hole Electrical Discharge Machining, ASME Journal of Manufacturing Science and Engineering, 130, 064502-1-6

Kao, C.C., Shih, A. J., (2008b) "Design and Tuning of the Adaptive Fuzzy Logic Controller for Micro-Hole Electrical Discharge Machining," Journal of Manufacturing Processes, 10, 61-73.

Kaneko, T., Tsuchiya, M. (1988), Three-dimensional numerically controlled contouring by electric discharge machining with compensation for the deformation of cylindrical tool electrodes, Precision Engineering, 10 (3), 157-163

Kunieda, M., Lauwers, B., Rajurkar, K.P., Schumacher, B.M. (2005), Advancing EDM through Fundamental Insight into the Process, Annals of the CIRP, 54 (2), 599-622

Kunieda, M., Miyoshi, Y., Takaya, T., Nakajima, N., Yu, Z, Yoshida, M. (2003), High speed 3D milling by dry EDM, Annals of the CIRP, 52 (1), 147-150

Kunieda, M., Takaya, T., Nakano, S. (2004), Improvement of Dry EDM Characteristics Using Piezoelectric Actuator, Annals of the CIRP 53 (1), 183-186

Kunieda, M., Yoshida, M., Taniguchi, N. (1997), Electrical Discharge Machining in Gas, Annals of the CIRP, 46 (1), 143-146

Kruth, J.P., Klewais, P. (1994), Optimization and dynamic adaptation of the cutter inclination during five-axis milling of sculptured surfaces, Annal of the CIRP, 43 (1), 349-354

Kruth, J.P., Snoeys, R., Van Brussel, H. (1979), Adaptive control optimization of the EDM process using minicomputers, Computers in Industry, 1 (2), 65-75

Kremer, D., Lebrun, L., Moisan, A. (1989), Effects of ultrasonic vibrations on the performance in EDM, Annals of the CIRP, 38 (1), 199-202

Kremer, D., Lhiaubet, C., Moisan, A. (1991), A study of the effect of synchronizing ultrasonic vibrations with pulses in EDM, Annals of the CIRP, 40 (1), 211-214

Lai, X.D., Zhou, Y.F., Peng, F.Y., Yan, S.J. (2003), Geometrical error analysis and control for 5-axis machining of large sculptured surfaces, International Journal of Advanced Manufacturing Technology, 21 (2), 110-118

Lee, Y.S. (1997), Admissible tool orientation control of gouging avoidance for 5-axis complex surface machining, Computer Aided Design, 29 (7), 507-521

Lee, Y.S. (1998a), Mathematical modelling using different endmills and tool placement problems for 4- and 5-axis NC complex surface machining, International Journal of Production Research, 36 (3), 785-814

Lee, Y.S. (1998b), Non-isoparametric tool path planning by machining strip evaluation for 5 axis sculptured surface machining, Computer-Aided Design, 30 (7), 559-570

Lee, Y.S., Ji, H. (1997), Surface interrogation and machining strip evaluation for 5-axis CNC die and mold machining, International Journal of Production Research, 35 (1), 225-252

Lin, J.L., Lin, C.L. (2002), The use of the orthogonal array with grey relational analysis to optimize the electrical discharge machining process with multiple performance characteristics, International Journal of Machine Tools and Manufacture, 42 (2), 237-244

Lo, C.C. (1999a), Efficient cutter-path planning for five-axis surface machining with a flat-end cutter, Computer-Aided Design, 31 (9), 557-566

Lo, C.C. (1999b), Real-time generation and control of cutter path for 5-axis CNC machining, International Journal of Machine Tools and Manufacture, 39 (3), 471-488

Luis, C.J., Puertas, I., Villa, G. (2005), Material removal rate and electrode wear study on the EDM of silicon carbide, Journal of Materials Processing Technology, 164-165, 889-896

Murthy, V.S.R., Philip, P.K. (1987), Pulse train analysis in ultrasonic assisted EDM, International Journal of Machine Tools and Manufacture, 27 (4), 469-477

Nakao, S., Shibayama, T., Kunieda, M., Araie, I. (2005), Curved surfece processing by Dry EDM using 5-axis machine, Journal of Japan Society of Precision Engineering Spring Quarter, 1351-1352 (In Japanese)

Peace, G.S. (1993), Taguchi Methods, Addison-Wesley Publishing Company, 448

Pham, D.T., Dimo, S.S., Bigot, S., Ivanov, A., Popov, K. (2004), Micro-EDM—recent developments and research issues, Journal of Materials Processing Technology, 149 (1-3), 50-57

Saito, K., Kishinami, T., Konno, H., Sato, M., Takeyama, H. (1986), Development of numerical contouring control electric discharge machining (NCC-EDM), Annals of the CIRP, 35 (1), 117-120

Snoeys, R., Dauw, D., Kruth, J. (1980), Improved adaptive control system for EDM processes, Annals of the CIRP, 29 (1), 97-101

Takeuchi, Y., Watanabe, T. (1992), Generation of 5-axis control collision-free tool path and postprocessing for NC data, Annals of the CIRP, 41 (1), 539-542

Tao, J., Shih, A. J., Ni, J. (2008) Experimental Study of the Dry and Near-Dry Electrical Discharge Milling Processes, ASME Journal of Manufacturing Science and Engineering, 130, 011002-1-9.

Wang, T., Kunieda, M. (2004), Dry WEDM for Finish Cut, Key Engineering Materials, 259-260, 562-566

Yoshida, M., Kunieda, M. (1999), Study on mechanism for minute tool electrode wear in dry EDM, Journal of the Japan Society of Precision Engineering, 65 (5), 689-693

Yu, Z.Y., Masuzawa, T., Fujino, M. (1998), Micro-EDM for three-dimensionalcavities - development of uniform wear method, Annals of the CIRP, 47 (1), 169-172

Yu, Z.B., Takahashi, J., Kunieda, M. (2004), Dry electrical discharge machining of cemented carbide, Journal of Materials Processing Technology, 149, 353-357

Yu, Z.B., Takahashi, J., Nakajima, N., Sano, S., Kunieda, M. (2005), Feasibility of 3-D Surface Machining by Dry EDM, International Journal of Electrical Machining, 10, 15-20

Zhang, J.H., Lee, T.C., Lau, W.S., Ai, X. (1997), Spark erosion with ultrasonic frequency, Journal of Materials Processing Technology, 68 (1), 83-88

Zhang, J.H. Zhang, H. Su, D.S. Qin, Y. Huo, M.Y. Zhang, Q.H. Wang, L (2002a), Adaptive fuzzy control system of a servomechanism for electro-discharge machining combined with ultrasonic vibration, Journal of Materials Processing Technology, 129 (1-3), 45-49

Zhang, Q.H., Du, R., Zhang, J.H., Zhan, Q.B., (2006a), An investigation of ultrasonic-assisted electrical discharge machining in gas, International Journal of Machine Tools and Manufacture, 46 (12-13), 1582-1588

Zhang, Q.H., Zhang, J.H., Deng, J.X., Qin, Y., Niu, Z.W. (2002b), Ultrasonic vibration electrical discharge machining in gas, Journal of Materials Processing Technology, 129 (1-3), 135-138

Zhang, Q.H., Zhang, J.H., Zhang, Q.B., Su, S.P. (2006b), Experimental research on technology of ultrasonic vibration aided electrical discharge machining (UEDM) in gas, Key Engineering Materials, 315-316, 81-84